MULTI-ANALYTE BIOSENSOR FOR PHYSIOLOGICAL STATUS MONITORING DURING HEMORRHAGE

A Dissertation

by

ANKITA DATTAPRASAD BHAT

Submitted to the Office of Graduate and Professional Studies of
Texas A&M University
in partial fulfillment of the requirements for the degree of

DOCTOR OF PHILOSOPHY

Chair of Committee,	Anthony Guiseppi-Elie
Committee Members,	Michael McShane
	Abhishek Jain
	Edgar Sanchez-Sinencio
Head of Department,	Michael McShane

May 2020

Major Subject: Biomedical Engineering

ABSTRACT

This project contributes to the development of a biocompatible, multi-analyte biotransducer and associated instrumentation that serves as a minimally invasive implantable biosensor system to improve patient stratification, guide resuscitation and monitor the stabilization of hemorrhaging trauma patients. The pH-responsive element of the multi-analyte biotransducer, with sensing elements for glucose, lactate, pH, potassium and partial pressure of oxygen (pO_2), was addressed. A pH-responsive hydrogel for the measurement of acidosis under physiological conditions was synthesized from poly(2-hydroxyethyl methacrylate-co-poly(ethylene glycol) methacrylate)-based hydrogels that were molecularly engineered with AEMA and DMAEMA and surveyed for the distribution of water states within the hydrogel. It was found that bound water, not total hydration, correlated strongly with the biotechnical properties, determined the membrane resistance and thereby the pH sensitivity of hydrogels. Surface modification of electrodes was accomplished using polypyrrole and bioactive hydrogels to reduce the charge transfer resistance for ABIO-BIO interface engineering. Using multiplexed biomarker inputs and physician expert scoring, a Hemorrhage Intensive Severity and Survivability (HISS) score was obtained from a fusion of input data and could correlate to survivability using data-driven prediction models. For real-time monitoring, this biotransducer was interfaced externally with hardware components including front-end electronics and a display readout. This microsystem will be used as an intramuscular indicator for the pathophysiology of hemorrhage.

DEDICATION

I dedicate this dissertation to my parents: Dattaprasad and Arthi, and grandmother Sukanti Bhat for their unconditional support.

ACKNOWLEDGEMENTS

I would like to thank my advisor Dr. Anthony Guiseppi-Elie for his help and support throughout the duration of his project, for introducing me to fields like electrochemistry and biomaterials, and for the timely guidance that helped me to expand my skill sets with expertise. I thank my committee members Dr. Michael McShane, Dr. Abhishek Jain, and Dr. Edgar Sanchez Sinencio for their invaluable inputs, comments, suggestions, time and expert feedback toward this project. I would like to commend the guidance provided by Aby Thyparambil, Olukayode Adedamola Karunwi, and Christian Kotanen. I highly appreciate the help and support provided by my lab colleagues: Dr. John Aggas, Sara Abasi, Brandon Walther, Lauren Whitney, and Naren Venkatesh. I would like to thank my collaborators: Dr. Edgar Sanchez-Sinencio, Dr. Judy Amanor Boadu, and Guillermo Garayar-Levya, Dr. Cerasela-Zoica Dinu, Dr. Abdollah Homaifar, and Shabnam Nazmi, Dr. Philip Horner, and his group members: Matthew Hogan, Hemang Trivedi, Dr. Daria Podstawczyk from Poland, and physicians from the University of Michigan: Dr. Kevin Ward, Dr. David Machado. I also want to commend the work by the undergraduates that I had the privilege to work with: Rafael Viana, Blake Smith, Victoria Nguyen, Florian Goncalves, Lauren Whitney, Urel Djiogan, Lamya El Nihum, Alexa Graham, and Vishal Valaboju. I would like to thank professors: Alan Brewer, Dr. Michael McShane, and Dr. Kristen Maitland, with whom I taught undergraduate courses like Senior Capstone Design and Bioinstrumentation (Teaching-As-Research Fellow). I would also like to thank my uncle Dr. Pravin Bhat and all my friends from Texas A&M University for their advice, encouragement and support.

CONTRIBUTORS AND FUNDING SOURCES

Professor Anthony Guiseppi-Elie is founder and scientific director of ABTECH Scientific, Inc., manufacturer of microfabricated biochip substrates and devices used in this dissertation.

Contributors

This work was supervised by a dissertation committee consisting of Professor Anthony Guiseppi-Elie, Chair, Professor Michael McShane, and Dr. Abhishek Jain of the Department of Biomedical Engineering and Professor Edgar Sanchez-Sinencio of the Department of Electrical Engineering.

Funding Sources

Graduate study (September 2016 – August 2018 and June 2019- May 2020) was supported by a Graduate Research Assistantship provided by Professor Anthony Guiseppi-Elie and Graduate Teaching Assistantship (September 2018- May 2019) from the Department of Biomedical Engineering at Texas A&M University.

NOMENCLATURE

HEPES	4-(2-hydroxyethyl)-1-piperazineethanesulfonic acid
PBS	Phosphate-buffered Saline
DMEM	Dulbecco's Modified Eagle Medium
DI	Deionized water
HEMA	2-hydroxyethylmethacrylate
AEMA	N-(2-aminoethyl) methacrylate
DMAEMA	N,N-(2-dimethylamino)ethyl methacrylate
SPMA	Sulfopropyl methacrylate
HMMA	N-[Tris(hydroxymethyl)methyl] acrylamide
HPMA	2-Hydroxypropyl methacrylate
PEGMA	Poly(ethylene glycol) monomethacrylate
pNVP	Poly(N-vinylpyrrolidone)
TEGDA	Tetra(ethylene glycol)diacrylate
DMPA	2,2-dimethoxy-2-phenylacetophenone
ϒ-APS	(3-aminopropyl)trimethoxysilane
APNHS	Acrylate-poly(ethylene glycol)-3500 n-hydroxysuccinimide
GOx	Glucose oxidase
LOx	Lactate oxidase
SWCNT	Single-walled carbon nanotube
H_2O_2	Hydrogen peroxide
DL	Detection limit

R_M	Membrane resistance
R_{CT}	Charge transfer resistance
PCB	Printed circuit board

TABLE OF CONTENTS

Page

LIST OF FIGURES

Page

LIST OF TABLES

Page

CHAPTER I

INTRODUCTION

1.1 Management of trauma-the pressing issue

Trauma management has continued to become a pressing issue in recent times. The dearth of point-of-care systems for monitoring the status of the patient, specifically during the transportation of the patient from the site of injury to a clinic poses a prominent challenge in trauma management. The intensity of the problem is reflected in the staggering statistics from National Trauma Institute in 2018, where trauma is the topmost cause of death in individuals of 1-46 years of age[1]. Amongst the simplest associations due to trauma, hemorrhage is the most significant[2] as it accounts for 40% of mortalities due to trauma[3]. Simple associations resulting due to trauma are shown in **Figure 1**.

One of the methods for trauma administration during transportation includes employing an advanced trauma life support (ATLS) trained workforce[1] to transport the patients from the site of injury to the clinic[2]. The most critical patients need to be saved in the "golden-hour period" where the time to intervene is less[3]. Silver-day refers to the time of 24 hours in which medical care is required[3]. Trauma related hemorrhage contribute highly to death rates in the first 24 hours[4]. Lerner *et al.* demonstrates a counter view for the term "golden-hour" used in medical literature and states that not much evidence is available to support the term[5]. However, it is a fact that time to intervene is critical during the initial time period in trauma and the most severe patients need to be stabilized.

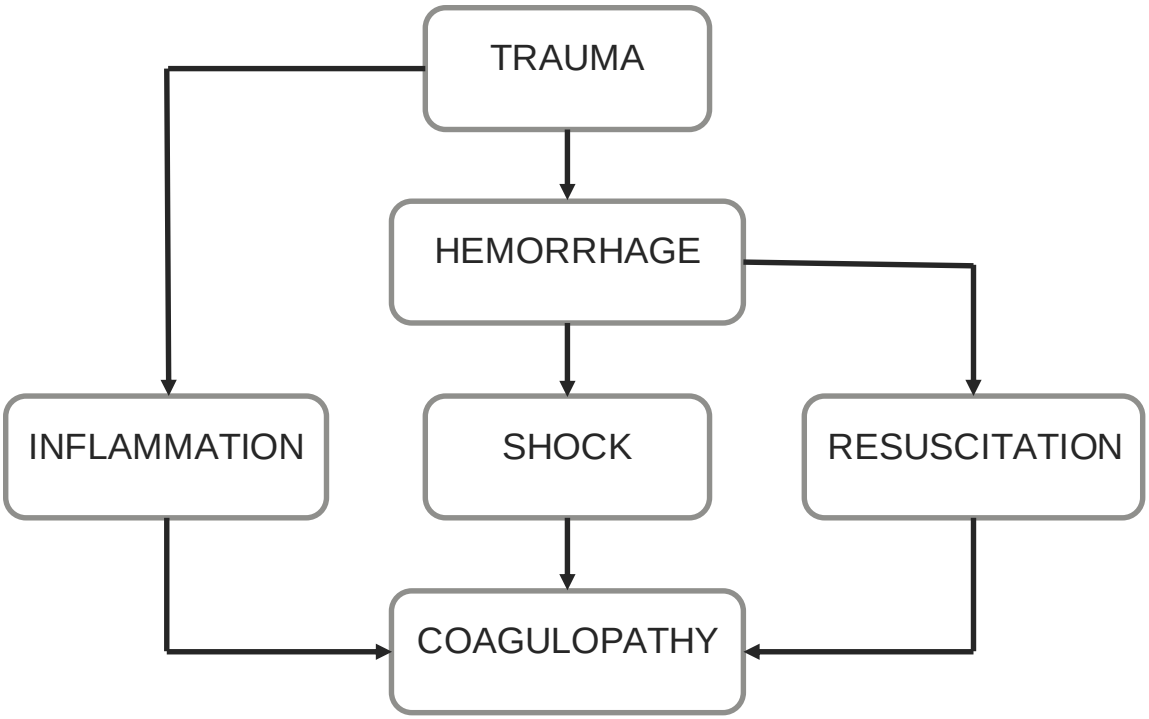

Figure 1. Simple associations due to trauma (Reprinted from source: National Trauma Institute) [6].

Shock is a state of lack of perfusion to the tissues [7]. ATLS identifies heart rate, systolic blood pressure and pulse oximetry or pulse pressure as the standard physiological cues for identifying the state of shock[8]. These current practices rely on testing the levels of analytes based in blood as a substrate. The vital signs predicted by using blood as a substrate may not be reliable and include many false negatives and false positives. These signs can give false complications that a critical patient is stabilized. Hence, it is indispensable to move to other substrates than blood.

A cascade of events occurs during hemorrhage due to trauma. In an attempt to stop the excessive blood loss due to injury, the blood pressure of the body drops[9]. This gives rise to the contraction of muscles, leading to sympathetic vasoconstriction[10]. This low peripheral

perfusion[11] which constitutes shock[12] and initiates tissue hypoxia[12]. This is accompanied by a fall in glucose levels[13] and a rise in the lactate levels[14] with a consequent fall in the pH of the body[15], which is countered with an increase in the levels of potassium[16]. To counter the effects of this cascade, resuscitation fluids are administered[17]. An adverse immune response is due to failure of the coagulation cascade[18] and a storm of local and systemic release of interleukins and cytokines is set up in the body, producing anti-inflammatory mediators[19]. The mediators move to vital organs causing their dysfunction leading to multiple organ failure[20]. This cascade of events for the pathophysiology of hemorrhage establishes the role of glucose (low), lactate (high), pH (low), potassium (high) and oxygen tension (low) together as biomarkers for trauma.

Minimally invasive biosensors provide a means to continuously monitor the patient data[21]. These biosensors are implantable and are stable and reside in the body for several weeks. They detect the levels of the analytes from the substrate they are dwelling in and hence can capture the status of these biomarkers in real-time. The data transmission can be made possible with the help of electronic hardware circuitry. Hence, these can be deployed in the management of trauma, especially during the transportation of the patient from the site of injury to the site of clinic. This will help in point-of-care stabilization of the patients. A layer of complexity can be added to form the physiologic profile of the patient by engaging machine learning algorithms to produce a single score, based on the levels of the five analytes, and further stratified according to the level of severity. This score can reveal the status of the patient to the physician in real-time, and care can be delivered to the most critical patients first. This score can help in the timely decision making of the physicians thus enabling reduction in morbidity and mortality due to hemorrhagic trauma.

Minimally invasive biosensors operate below epidermis or dermis at a specific depth and are subcutaneously implanted with the help of a small suture or surgery [22]. The in-dwelling or implantable type of minimally invasive biosensors can reside in the body for a few days and can be used for continual or continuous monitoring for point-of-care diagnostics (POC)[23]. The non-invasive wearable biosensors have less accuracy and do not involve breaking the skin barrier[24]. As against this, the fully invasive biosensors break the skin and are implanted at a considerable penetration depth. Thus, the minimally invasive biosensors are a mid-way between the non-invasive and the fully invasive biosensors. They can be inserted into the body with the help of a small suture/ incision or a surgery and provide a high accuracy[25]. **Figure 2** illustrates the concept of a minimally invasive biosensor.

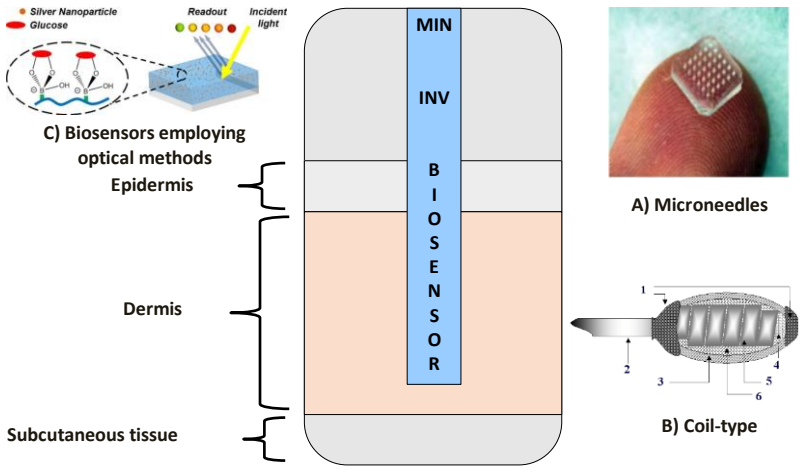

Figure 2. Concept of a minimally invasive biosensor and some of the commonly used minimally invasive biosensor types (Reprinted from [22]).

Microneedle type of minimally invasive biosensors[26] incorporate a solid or a hollow cannula with external diameter of about 30 microns[27] and with an insertion length[28] of about 20 to 1500 microns. It is important that the tip of the biosensor does not break. Hence, the mechanics of force should be studied while breaking the skin[29]. The geometry aspects such as microneedle length, tip radius, wall thickness, base density, diameter, and wall angle, and the

type of material along with the skin resistance to penetration dominate the successful insertion of the minimally invasive biosensor[30]. In comparison, Yu *et al.* have reported coil-type minimally invasive biosensors which allow for more loading of the enzyme, due to a larger electrochemical surface area and a higher current response[31] . Optical methods can also be used in minimally invasive biosensors. A polyacrylamide gel with silver nanoparticles has been utilized by Yetisen *et al.* where the glucose molecules bind to hydrogel causing the silver nanoparticles to separate, hence detecting the presence of glucose[32].

This paper is a critical review of the minimally invasive implantable biosensors used for the pathophysiology of hemorrhage. The different analytes like glucose, lactate, pH, potassium and partial pressure of oxygen are considered as their levels fluctuate during hemorrhage due to trauma. Hence, they can be considered as the biomarkers for trauma. An effort is made to diversify the substrate from interstitial fluid to blood.

Although the traditional substrate is blood, it has been found that the interstitial fluid[33] in the muscles can work as a substrate for biomarkers of trauma. The interstitial fluid is the bathing medium for the tissues[34]. This fluid can act as the substrate because the muscles are the action point of tissue hypoxia[35]. Due to tissue hypoxia, the blood flow drops as the peripheral vasoconstriction occurs. Hence, tapping this substrate specifically in the hemorrhaging trauma can be promising in place of blood. Also, muscles form a network throughout the body and are the largest utilizers of oxygen[36]. Hence, muscles is where the initiation point of tissue hypoxia lies, as a consequence of which the lactate levels are elevated during hemorrhagic trauma. Specifically, for measuring glucose the interstitial fluid can prove helpful with the microneedles technology[37].

Implantable biosensors face challenges of biofouling and fibrous encapsulation[38]. As such, they have to be treated for enhanced stability[39]. Biofouling refers to adsorption of proteins or other biomolecules on the sensor region and blocking it, causing it to foul and decrease in its performance[40]. To counter this biofouling, the biosensor has to be modified with a biocompatible coating like hydrogels[41].

In the following section, an overview of the present minimally invasive devices for monitoring each of the individual analytes of glucose, lactate, pH, potassium and oxygen tension is performed. The ranges of analytes for pathophysiological intravascular, and intramuscular glucose[42], lactate and pH[43], potassium[44], oxygen tension[45, 46] [46]are mentioned in **Table 1** as follows:

Table 1. describes the ranges of analytes which are biomarkers for hemorrhagic trauma including pathophysiological intravascular ranges and upper and lower bounds for intramuscular ranges.

	Pathophysiological range				
Analyte	Lower Bound	Low	Normal	High	Upper Bound
Glucose	0.1-0.5 mM	Hypoglycemia <3.88 mM <70 mg/dL	Euglycemia 3.88–5.50 mM 70-99 mg/dL	Hyperglycemia 5.50–10.00 mM 99-180 mg/dL	
Lactate		Hypolactatemia < 0.50 mM	Eulactatemia 0.50–1.00 mM	Hyperlactatemia 2.00–4.00 mM	5-8 mM
Potassium		Hypokalemia (<3.50 mM)	Eukalemia 3.50-5.50 mM	Hyperkalemia (>5.50 mM)	5.5-7.2 mM
pH	7-7.35	Acidosis (<7.35)	7.35-7.45	Alkalosis (>7.45)	
pO_2	1-9 mm Hg	Hypoxia <5.18 mM <100 mmHg	5.18-6.22 mM 100-120 mmHg	Hyperoxia (>6.22 mM) >120 mmHg	

The measurement techniques associated with the five analytes are glucose (amperometry), lactate (amperometry), potassium (K+) (potentiometry), pH (impedimetry), and oxygen tension (voltammetry). The concept for dose-response curves along with the measurement techniques for the analytes are discussed in Thévenot et al.[47]

1.2 Minimally invasive biosensors for pathophysiology of hemorrhage

Glucose and Lactate operate on the principles of enzymatic biosensors. Enzymatic biosensors which detect glucose and lactate are mostly electrochemical due to their fast response times, high sensitivity and cost efficiency [48]. Glucose and lactate sensing regions incorporate immobilized enzymes like Glucose Oxidase (GOx)and Lactate Oxidase (LOx) onto them. The reactions for the detection of glucose and lactate proceed as follows:

The enzymatic oxidation of analytes with enzymes produces H_2O_2 (Eq.1 and Eq.2)[49, 50].

$$L - lactate + O_2 \xrightarrow{LOD} pyruvate + H_2O_2 \quad (1)$$

$$glucose + O_2 \xrightarrow{GOD} gluconolactone + H_2O_2 \quad (2)$$

These reactions produce electrons as follow (Eq. 3)s:

$$H_2O_2 \rightarrow O_2 + 2H^+ + 2e^- \quad (3)$$

These electrons can be detected amperometrically, using EIS (Electrochemical Impedance Spectroscopy) techniques. Hydrogen peroxide generated can be electrochemically oxidized on a Platinum electrode at +600 mV with an Ag/AgCl reference electrode. Glucose and Lactate have been characterized in the previous generation dual analyte biochip[51]. Both sensors have a working, reference and counter electrode.

The equation for current[52] (Eq. 4) is

$$i(t) = \frac{nFAD_{app}^{1/2}C^*}{2\pi^{1/2}t^{1/2}} + \frac{nFAD_{app}\,C^*}{2r_o} \quad (4)$$

Where *n* is a number of electrons, *F* is Faraday Constant, *A* is area of the planar electrode, D_{app} is the Diffusion coefficient, *t* is the time in seconds, and *C** is a standard concentration.

1.2.1 Glucose

POC testing devices for glucose use finger pricking, using fluids such as tears, saliva, and excretory products like urine[53]. These methods are invasive, painful and need to be conducted frequently. Moreover, they do not convey time and the change in glucose magnitude over time[30]. On the contrary, minimally invasive devices are safe and use a less obstructive approach with minimal tissue invasion and inflammation that doesn't damage the tissue much. Minimally invasive and continuous monitoring sensor devices are called MiCoMs[54]. Microneedle array electrodes made from SU8 50 material are described in Sharma et al.[55] and are shown in **Figure 3.** This array of electrodes is inserted by breaking the topmost layer of the skin and are implanted in the forearm. Chronoamperometry[56] was used to measure the in vivo current. The use of microneedle sensor arrays has been described in Mohan et al.[54] The review by El-laboudi et al. described a minimally invasive continuous monitoring glucose sensor that uses Interstitial Fluid (ISF) as the substrate[30].

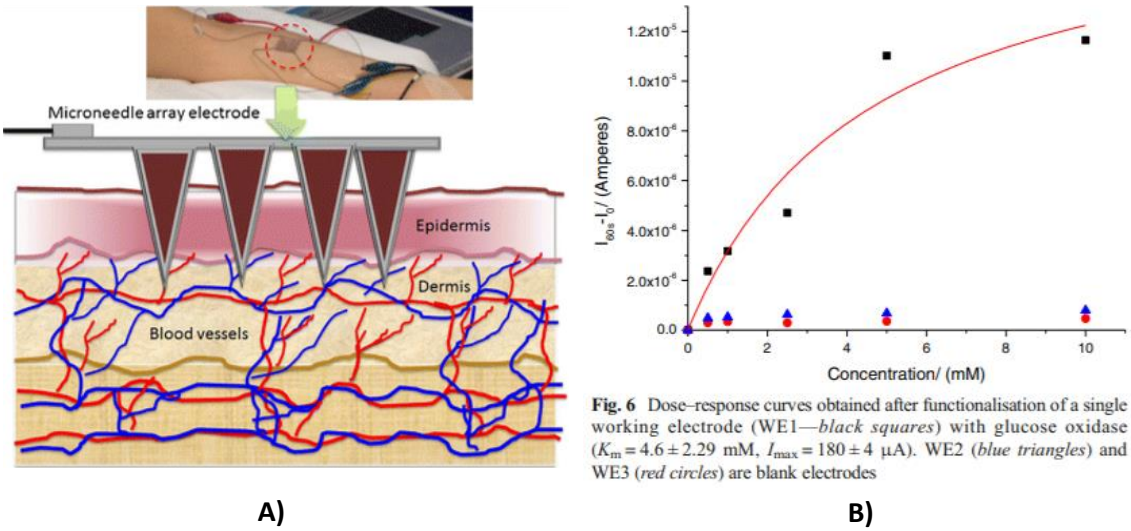

Fig. 6 Dose–response curves obtained after functionalisation of a single working electrode (WE1—*black squares*) with glucose oxidase ($K_m = 4.6 \pm 2.29$ mM, $I_{max} = 180 \pm 4$ μA). WE2 (*blue triangles*) and WE3 (*red circles*) are blank electrodes

A) **B)**

Figure 3. (A) Concept of a minimally invasive glucose biosensor, and (B) Dose-response curves (Reprinted from [55]).

1.2.2 Lactate

Humans have resting base lactate levels of 0.5-1.0 mM. During hemorrhage, the body goes into the anerobic respiration mode and consequently the lactate level increases due to abnormality in the Cori-cycle[57] . The lactate then is accumulated in the liver by diffusion into the bloodstream[58, 59] [59]. Hence, it is important to detect the rise in levels of lactate, which act as a predicator/precursor for the condition of shock or lack of perfusion to the tissues.

Higher lactate levels is an biomarker for tissue hypoxia and the criticality of the shock[60]. It is also a precursor for base deficits giving rise to lowering of pH[61] and resulting acidosis. Lactate along with base deficit[62] can help understand the extent of shock[63]. Restoration of the abnormal lactate levels are correlated with survival[63]. Early detection of the same can help in predicting survival and patient outcomes[64]. The accumulation of lactic acid due to inadequate clearance by liver and kidney causes lactic acidosis[65].

Lactate can be sensed using screen printed graphite electrodes, and microneedle sensors as shown in **Figure 4.**

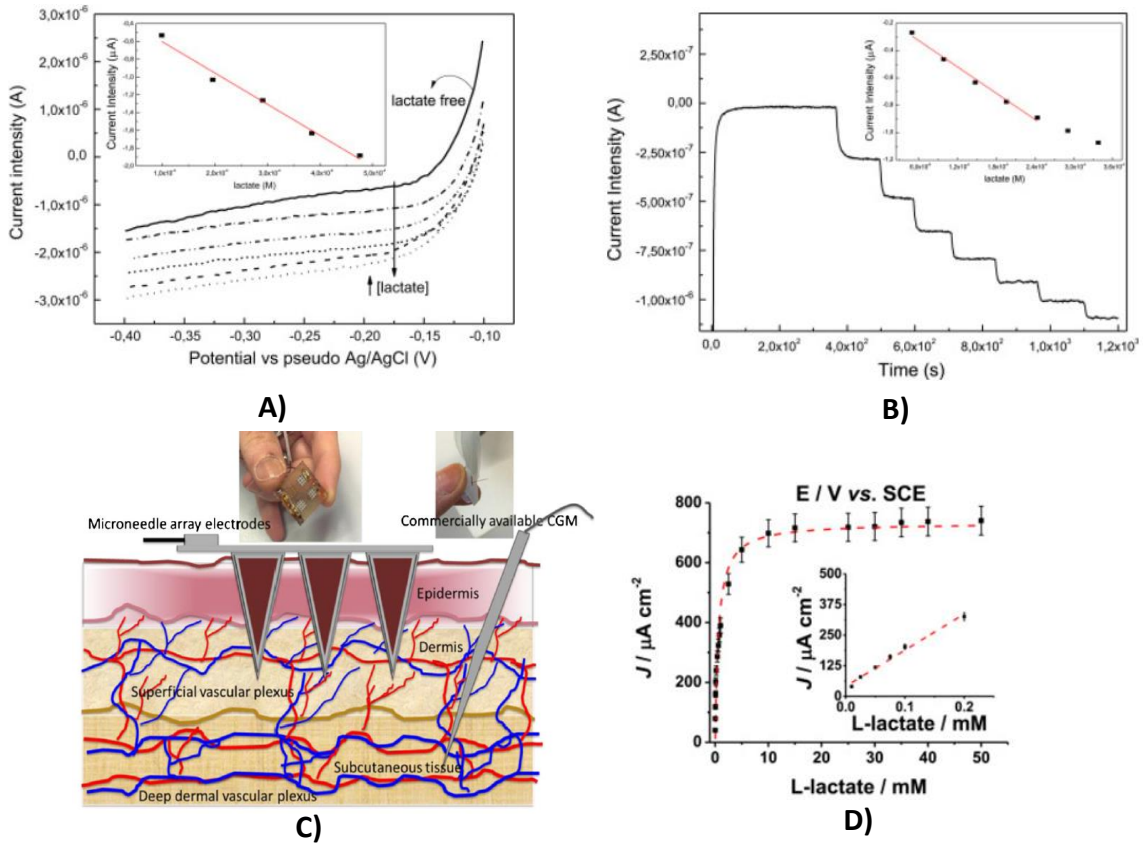

Figure 4. Responses from an electrochemical lactate biosensor A) Linear sweep voltammetry response[65], B) Chronoamperometric response (Reprinted from [65]), C) Concept of a minimally invasive lactate biosensor[66], and D) Calibration curve of gold microneedles (Reprinted from [66]).

1.2.3 pH

Hydrogels are three-dimensional network structures which swell with the uptake of water and de-swell with the loss of water[66]. Tissue acidosis occurs due to anaerobic glucose metabolism during tissue hypoxia. The distribution of water and the impedimetric response of hydrogel membranes of pH responsive devices is of interest for the development of in-dwelling biomedical sensors that must measure small changes in pH associated with tissue acidosis. Water

distribution and impedance changes due to small pH shifts are a function of monomer compositions in the hydrogels. Stimuli responsive hydrogels are a specific type of hydrogels which respond to a change in stimulus in their external media (eg. pH, temperature, chemical, light) by altering their mesh sizes[67]. pH sensor are the type of stimuli responsive hydrogels[68] which can be ionogenic or neutral type, depending on the presence of ionizable groups in their structure. Ionogenic hydrogels respond to a change in pH by protonating-deprotonating the ionizable groups in their structure[69]. Common cationic monomers include methacrylic acid, acrylic acid, N-(2-aminoethyl) methacrylamide, and anionic monomers include acrylamide, diethylaminoethyl methacrylate, dimethylaminoethyl methacrylate[70]. As against ionogenic, neutral hydrogels respond to a change in pH by means of donnan partitioning[71].

Monitoring of pH in the physiological pH range from 7.35-7.45 is crucial in stabilization of trauma patients[72] .A pH which is more acidic than 7.35 and accompanied by a rise in the lactate levels is termed to be acidosis[73], a condition which can be lethal. The water content in hydrogels plays an important role in governing its biotechnical properties[74]. Specifically, the bound water content governs the total hydration in poly-(HEMA) based stimuli responsive hydrogels[75]. Lactic acid acidosis is a biomarker for hemorrhaging trauma[76]. The relation between high lactate and hypoxia has been described using an oxyhemoglobin dissociation curve in Leach *et al.*[77].

pH sensor is an interdigitated IAME-co-IME sensor with hydrogel attached onto it[78]. Poly-(HEMA) based hydrogels have been utilized to give a sensitive pH response. Sheppard *et al.* explains the use of N,N-(2-dimethylamino)ethyl methacrylamide (DMAEMA) in the pH range 7-8[69]. Experimentally, the cationogenic N-(2-aminoethyl) methacrylamide (AEMA)has been determined to be the sensitive hydrogel in the pH range 7.35-7.45[79].

Hydrogel based minimally invasive sensors for pH sensing have been described in **Figure 5.** In Culver *et al[80],* the hydrogels undergo conformational changes when the target analyte binds to them and sense the change in pH. This can be extended to cross-linking from complementary DNA to give rise to a hydrogel assembly, used as a pH sensor. Yin *et al.* have described the pH sensitivity of polyacrylamide hydrogels due to changes in the pH induced functional group change in the pH[81]. Tamayol *et al.* have described the response of a fiber sensor to the pH variation[82]. Sheppard *et al.* have reported the pH sensitivity using DMAEMA hydrogels[71].

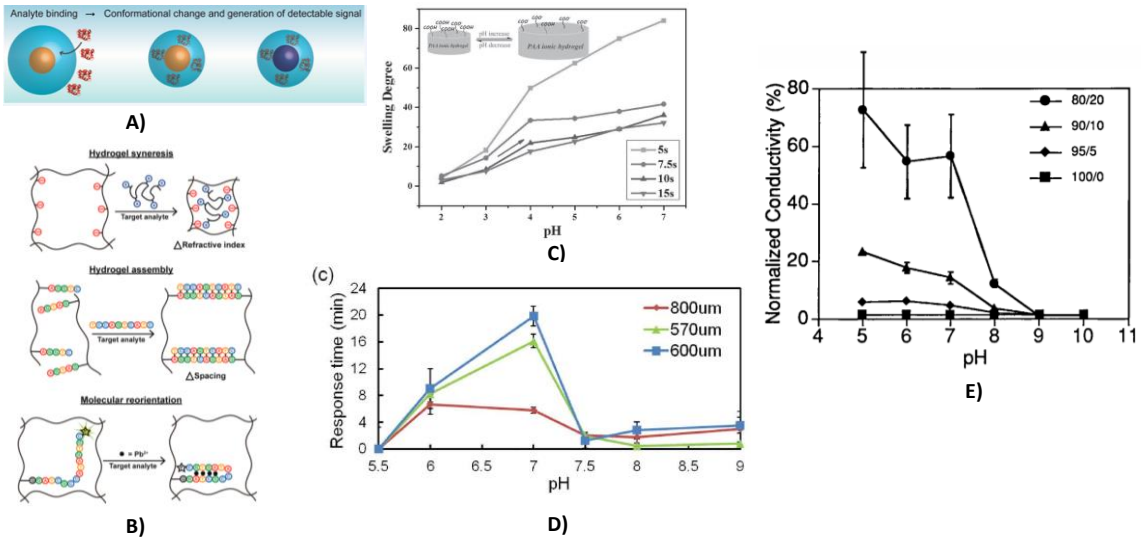

Figure 5. pH sensing using minimally invasive approaches (A) Analyte-responsive hydrogels for sensing, (B) Sensor mechanisms (C) Swelling degree of PAA ionic hydrogel with increasing pH, (D) Response of a fiber sensor to pH variation, and (E) pH sensitivity of D (Reprinted from [82]).

1.2.4 Potassium

Hyperkalemia refers to elevated levels of potassium as a result of hemorrhaging trauma[83]. The renal functions of the kidney do not suffice to match the excessive efflux of potassium in the extracellular region[84]. The regulation of potassium hemostasis is impaired as the secretion of potassium by vasopressin is inadequate is described in Uyehara *et al.*[85]. Zhou *et al.* describe a potassium monitoring approach using cDNA hybridization. **Figure 6.** describes the relation between vasopressin and renal clearance[85], and the logarithmic and linear responses from the potassium monitoring using DNA hybridization[86].

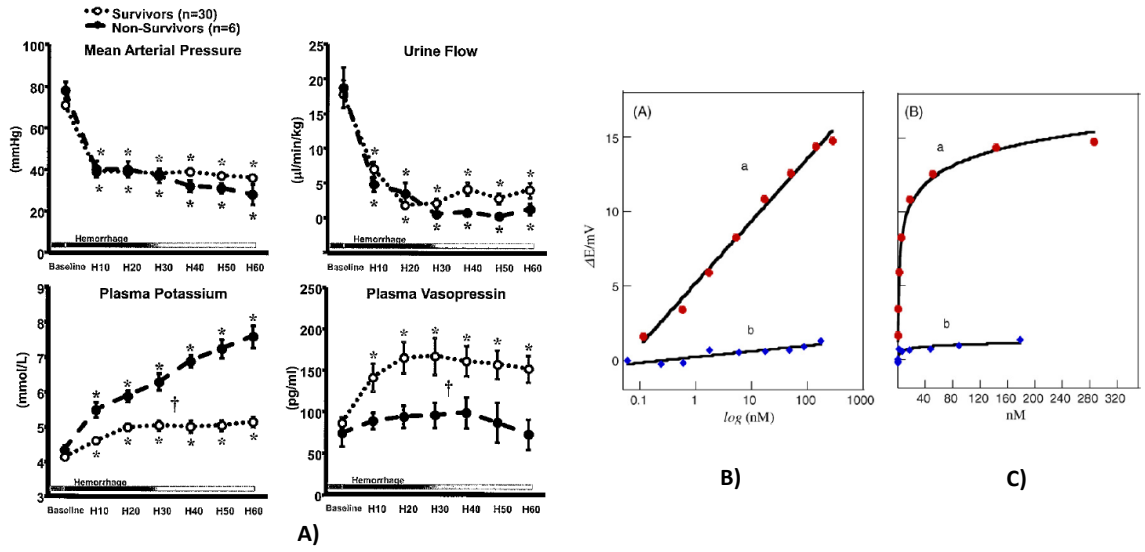

Figure 6. (A) Relation between vasopressin and renal potassium clearance, Potassium sensing using: DNA hybridization (B) Logarithmic response, and (C) Linear response (Reprinted from [85]).

The detection of potassium is governed by the Nernst equation (Eq. 5.)[87].

$$E = constant + \left(\frac{2.303RT}{zF}\right)\log\left[\frac{ion\ outside\ cell}{ion\ inside\ cell}\right] \quad (5)$$

Where E is the potential, R is the ideal gas constant (joules per kelvin per mole), T is the absolute temperature, z corresponds to the ion charge (for potassium ion z is +1), F is Faraday constant.

A relation has been described between hemorrhagic shock, tissue hypoxia and potassium in Filho *et al*. as shown in **Figure 7.** [88]. Strong correlations have been reported potassium and lactate (R=0.82), potassium and changes in partial pressure of carbon dioxide (R=0.82), potassium and changes in pH (R=0.83) [88].

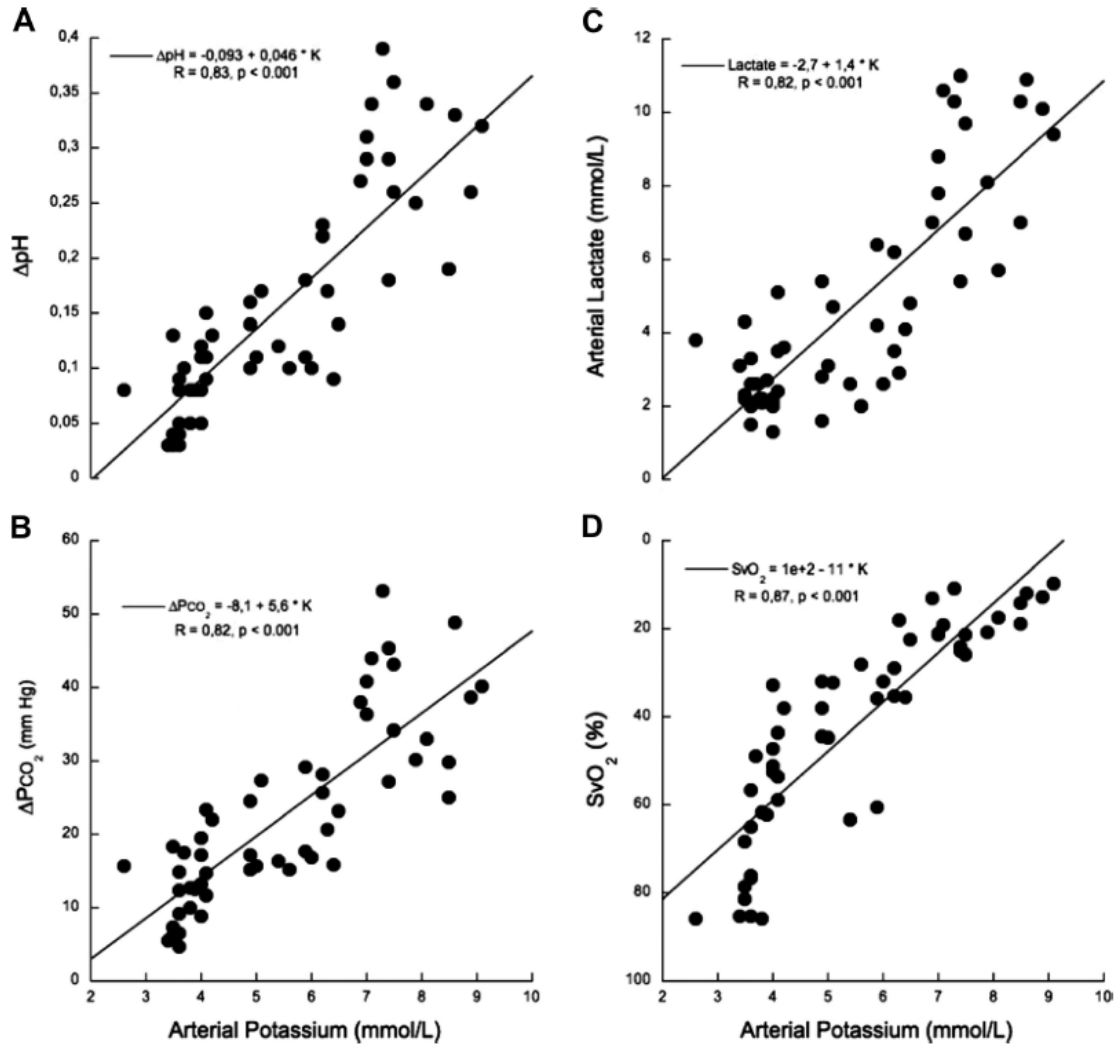

Figure 7. Relation depicting (A) Changes in pH, (B) Changes in partial pressure of carbon dioxide, (C) Arterial lactate, and (D) Arterial potassium (Reprinted from [89]).

1.2.5 Oxygen tension

Tissue oxygenation is an important parameter in the detection of hemorrhage[90]. Tissue saturation can be bifurcated into two parameters: Saturation pressure of oxygen (SpO_2) and partial pressure of oxygen (pO_2), which can in turn be related to hemoglobin saturation using the hemoglobin-oxygen dissociation curve [91] described in Collins *et al.*[91] as shown in **Figure 8**.

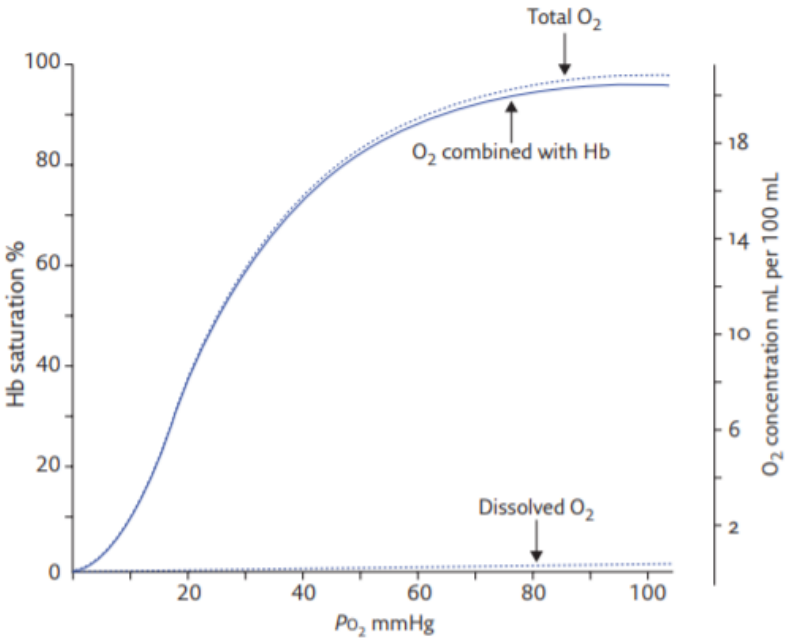

Figure 8. Relation between partial pressure of oxygen with hemoglobin saturation and oxygen concentration (Reprinted from [91]).

The current standard of care involves using pulse oximetry which measures the saturation pressure of oxygen. However, the saturation pressure measures the oxygen only at the local tissue levels [13] , and hence cannot be a reliable predictor for trauma-related hemorrhage involving acidosis. Tissue hypoxia correlates with hyperlactatemia which is a consequence of shock.[92]

Zelechowska *et al.* have monitored the dioxygen levels using cyclic voltammetry [93] using electrodes made from carbon nanotubes. Carbon paste electrodes have also been used for measuring tissue oxygenation by Bolger *et al.* [94]. Electrocatalysis have been performed using carbon-containing palladium nanoparticles modified using a platinum monolayer in Zhang *et al.* [95]. Hematite nanoparticles have been used on modified glassy carbon electrodes. Here, oxygen was electrocatalytically reduced using the four-electron pathway. The mechanism of oxygen reduction has been expressed using the Randles- Sevcik equation (Eq. 6)[96].

$$I = 2.99 \times 10^5 \, n(n' + \alpha)^{1/2} A D^{1/2} C v^{1/2} \quad (6)$$

Where I is the current produced, n is number of all electrons in the process, n' is the number of electrons in the prior step, α is the transfer coefficient, A is the active surface area of working electrode, D is the diffusion coefficient of oxygen, C is the concentration of oxygen and v is the scan rate [97]. **Figure 9.** shows the responses for oxygen sensing using different types of electrodes.

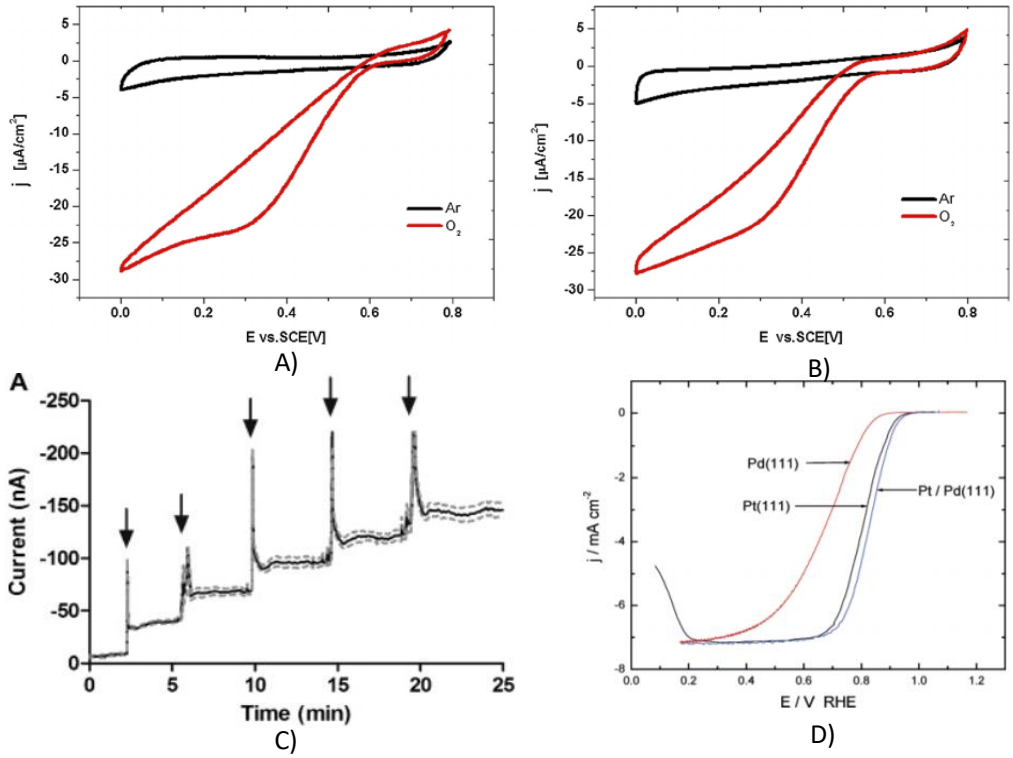

Figure 9. Cyclic voltammetric responses for direct reduction of oxygen with electrodes made from A) functionalized CNT and B) Bilirubin Oxidase, C) Current versus time response for Carbon Paste Electrodes, D) Polarization curves for oxygen reduction on Platinum/Palladium electrodes (Reprinted from [93]).

Ward *et al.* have reported the measurements of tissue oxygenation in the skeletal muscles. Here, near infra-red spectroscopy has been utilized to understand how comparing the absorption

spectra for various types of hemoglobin helps to track changes in the oxygen delivery and its consumption by organs [98].

1.3 Decision-making using a patient stratification profile

Trauma patients need to be closely monitored especially during their transport from the site of injury to the site of clinic. There is a dearth of efficient functional modalities in the creation of monitoring and patient stratification profiling. High number of casualties could be attributed to the technical gap in this area [99]. One such computer decision-support system has been developed by Salinas *et al.[99, 100].* This computer-based system includes wireless transmission capability. Here, transmission of important parameters like pulse oximetry, blood pressure, pulse rate and heart rate is explored. To enable the storage of the profile for the patient the data transmission needs to be coupled with a data-logger system. These five analytes can be used together in conjunction with classification algorithms to form a patient stratification profile.

An adjunct device can enable in decision making of the physicians regarding the criticality of the patient. This minimally invasive device can be implanted pre-emptively or by the first responder at the site of injury. This can enable immediate and continuous measurement of the trauma patient's physiological status in a real-time fashion. Point-of-care monitoring[101] in trauma is of paramount importance as it can tell the EMS personnel about the status of the injured person in real-time and help in speedy triage.

Liu *et al.* have reported the use of Wireless Vital Signs Monitor, Athena GTX to monitor vital signs and heart rate parameters [102]. For detecting the trends in the datasets, usage of machine learning algorithms based on artificial intelligence[103] has been suggested. This can be coupled with deep learning approaches to incorporate the growing data sets of patients. This

exorbitant amount of information data can be transmitted to hospital settings using wireless telemetry systems. **Figure 10.** shows the systems used for monitoring the patient status wirelessly.

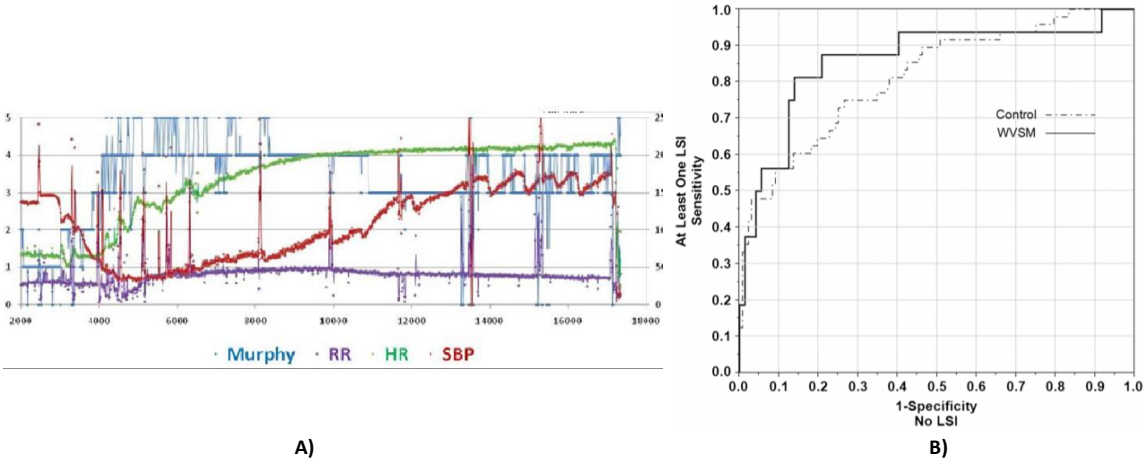

Figure 10. Monitoring of patient status using an algorithm to support decision-making using (A) Murphy factor algorithm to monitor vital signs, and (B) Wireless, portable vital signs monitor (WVSM) (Reprinted from [102]).

1.4 Wholesome system for the management of trauma

A wholesome system as a biosensor has been devised by Guiseppi *et al.* It is dual-analyte in nature, incorporating glucose and lactate [51]. This designed and fabricated system is tested in small animals [104]. Data is acquired using a dual-responsive bioSONDE kept indwelling into the muscle of the animal [52]. This biosensor has a hardware interface to gather, process and store the data from the two analytes in the form of a wireless bluetooth potentiostsat [51].

Taking inspiration from the dual-analyte biosensor, the system has been improvised to incorporate three more analytes in the same foot print area of 2 mm x 4 mm. The hardware components of a biosensor microsystem can include the biotransducers, front-end electronics

such as potentiostat, AD/DA, medical frequency wireless telemetry, base stations, remote computer, and display readout.

Important considerations for hardware design include data collection (current, potential, etc.), information transfer, security, signal processing, storage, device footprint, portability, and user friendliness. Hardware must be able to securely collect raw data from the biotransducers, in this case five separate biotransducers for five separate analytes, and transmit that to a computer processing station, temper and interpret the collected data, and display actionable data to the end user. Hardware has been improved to incorporate will be able to manage power usage for all system components, collect and condition all analog signals from the five biotransducers of the SONDE, digitize those analog signals, store raw or conditioned data and operational parameters, wirelessly support unidirectional or bidirectional communication with a base station, rapidly wake up from a low-power "sleep" for immediate data collection. The microsystem will be externalized on animals and the SONDE will be indwelling in the muscle of the animal which must be fully ambulatory.

Trauma-induced hemorrhage with its attendant peripheral vasoconstriction, insulin resistance, hyperlactatemia, acidosis, hyperkalemia, and hypoxia can rapidly lead to death or may be followed by a "cytokine storm" which can subsequently lead to Multiple Organ Dysfunction Syndrome (MODS), which can also be fatal [51]. A MODS severity score was developedby Marshall et al. in 1995, wherein a score (0-4) is applied by physiologic measurement of dysfunction in 6 organ systems [105]. The total number of input points were then added to achieve a score corresponding to the patients' ICU mortality %, hospital mortality %, and ICU stay. A score similar to MODS, called the Hemorrhage Intensive Systemic Score (HISS) is introduced to allow for patient stratification based on biomarker data fusion. HISS is a severity index intended

as an adjunct to inform trauma victim healthcare providers of the criticality of the patient's health and help them deliver timely and appropriate care and attention, as required[106]. This can help in timely triage and stabilization of the most critical patients and a consequent reduction in patient mortality [13]. This bio-SONDE, combined with a wireless processing hardware and a software algorithm to enable data fusion from the five identified biomarker analytes, can guide evidence-based decision making derived from the real-time pathophysiological profile of the patient.

For decision-making, different software algorithms like fine decision tree classifier, ensembled bagged decision tree classifier, linear support vector machine, fine gaussian support vector machine, artificial neural network, and possibility rule-based classification method on the data with 40% uncertainty (noise) in scores are explored. The predictions made by the data-driven model in conjunction with an adjunct device in the form of a multi-analyte biosensor intended for point-of-care continual monitoring of trauma patients, aid in decision-making, particularly in a scenario involving mass casualties.

Synthetic data sets are developed, in lieu of actual patient data, 200 Sensible Fictitious Patient data sets, each containing the results of the five biomarkers, were created using an algorithm scripted in Python 3.7.0. In the proposed strategy, each biomarker attribute was stratified into three levels corresponding to, for example, hypolactatemia (Low), eulactatemia (Normal), and hyperlactatemia (High). The details of the stratification are provided in **Table 1**.

Lactate was selected to serve as the principal indicator of pathophysiological stress in the hemorrhaging trauma patient[63]. A random number generator (RNG) was used to select a bounded value of lactate that corresponded to either hypolactatemia, eulactatemia or hyperlactatemia. Correspondingly bounded values for glucose, potassium, pH and oxygen tension (pO_2) were then selected based on the initial, seeded stat lactate value to generate a

physiologically consistent, randomized fictitious patient data set. These synthetic data sets are then validated by real-life physicians by providing scores or labels corresponding to each data set. These constitute the testing sets, against which the performance of different algorithms is measured.

1.5 Future scope

Minimally invasive biosensor devices with minimal stress to skin propose a new direction to the point-of-care monitoring devices for real-monitoring of hemorrhagic trauma. Five biomarkers of glucose, lactate, pH, potassium, and oxygen tension with their levels during hemorrhagic trauma are discussed. The measurement techniques for each of these biomarkers is also discussed. Glucose and lactate are detected by electrochemical enzymatic biosensor methods utilizing amperometry [107]. pH sensor is using stimuli-responsive hydrogels using impedimetric[108] approach. Potassium is monitored using a Nernstian approach. Oxygen tension is monitored using electrochemical reduction of oxygen using voltammetry approach[109]. An integrated hardware platform[110] is proposed to gather, process and store the data generated form these five analytes incorporated on a single biochip. Finally, the system for point-of-care monitoring is made wholesome using a data-driven approach for decision-making by employing classification algorithms. Extracted models are used to generate score predictions to create the patient stratification profile corresponding to patient severity which will help to guide resuscitation. [13] Data will be transmitted wirelessly[111] using low-power bluetooth modality[112] to a remote base-station.

1.6 Conclusions

Minimally invasive biosensors offer an advantage of high accuracy over non-invasive and less penetration depth over fully invasive biosensors. Point-of-care stabilization of hemorrhagic trauma patients is required to reduce morbidity and mortality. The current standard of care approach of monitoring the vital signs is not sufficient. Hence, there is a need to move to other substrates than blood. Interstitial fluid in muscles at the action point of tissue hypoxia poses a reliable substitute for blood. Biomarkers for pathophysiology of trauma include glucose(low), lactate(high), pH(low), potassium(high), and oxygen tension(low). Real-time monitoring for these biomarkers needs to be supported using a wholesome biosensor system, with wireless transmission capability and embedded algorithms, enabling patient stratification for efficient data-driven decision-making by the physicians. This can help in scenarios involving mass casualties, particularly during the transport of the patients from the site of injury to the site of clinic by the primary trauma care providers.

CHAPTER II

MOLECULAR ENGINEERING OF POLY(HEMA-*CO*-PEGMA)-BASED HYDROGELS: ROLE OF MINOR AEMA AND DMAEMA INCLUSION*

2.1 Introduction

Synthetic hydrogels are three-dimensional polymer networks synthesized from highly hydrophilic, water soluble monomers rendered water insoluble by electrostatic or covalent crosslinking and consequently imbibe and retain a significant weight fraction of water compared to the total polymer content [113]. Hydrogels are well-established biomaterials with a diverse array of biomedical applications. Traditionally, synthetic hydrogels have been applied as contact lenses [114], linings for artificial hearts [115], materials for artificial skin [115], three-dimensional scaffolds for tissue engineering and regeneration [116-118], bioreceptor hosting membranes for biosensors [119, 120], and sophisticated responsive drug delivery devices [121-123]. This diversity of applications reflects the fact that hydrogels may be molecularly engineered to achieve targeted physicochemical and stimuli-responsive properties [124]. However, major technical challenges are still found when tailoring hydrogels to the needs of the environments in which they are applied and while also eliciting the optimized desired response to stimuli originating from that environment. A suitable simple example is an implantable pH sensor wherein biocompatibility and pH-sensitivity are both desired characteristics [125, 126].

---

*Reprinted with permission from "Molecular engineering of poly (HEMA-co-PEGMA)-based hydrogels: Role of minor AEMA and DMAEMA inclusion" by **Bhat, A.,** Smith, B., Dinu, C. Z., & Guiseppi-Elie, A., 2019. *Materials Science and Engineering: C, 98,* 89-100.

In order to impart desired functionality, e.g. pH response, monomer constituents and/or chemical modifiers are added to the hydrogel network. Some modifiers alter the primary repeat unity structure of the hydrogel and in so doing have the potential to induce new architectural features from crystallinity to micelle formation. For example, poly(ethylene glycol) (PEG) may be added to hydrogels, ostensibly to mitigate protein adsorption and hence confer biocompatibility, although immunogenicity is now a concern with such materials [127, 128]. However, PEG inclusion may also influence total hydration, small molecule diffusivity and produce a change in elastic modulus [117, 129]. This illustrates the decisive impact monomer composition can have on global hydrogel properties. As such, it is important to characterize the changes in physicochemical properties and the corresponding biological response to hydrogels once desired chemical modifiers have been added and to subsequently optimize their composition to achieve targeted performance. The hydrogel characteristics analyzed in this study were, i) the total hydration as determined by gravimetry, ii) the distribution of water among free and bound states as determined by differential scanning calorimetry (DSC), iii) the elastic modulus as measured by force-displacement using an AFM method, iv) the membrane resistance calculated from Electrical Impedance Spectroscopy (EIS) data and equivalent circuit modeling, and v) the biological response of protein coverage determined by albumin adsorption isotherms on the hydrogel surfaces.

The degree of hydration (DoH), free water and bound water content are key hydrogel properties to take into consideration because of their profound impact on the functionality of hydrogels for biomedical application [130]. For example, the quantity and distribution of water within hydrogels have been shown to alter the sorption and diffusive transport of drugs [131] and have also been tailored for the fabrication of injectable hydrogels used in surgery and localized

therapy [130]. The balance among hydrophilic /hydrophobic character of functional groups on the polymer backbone and the segmental dynamics of the polymer network are responsible for the amount of water that can be imbibed (DoH) as well as the state distribution of water within the polymer network (free vs. bound water) [130]. The degree of hydration reflects the total amount of water imbibed by the hydrogel. Once imbibed, water within a hydrogel is described to exist as freezable free water, freezable bound water, and non-freezable bound water [132]. For simplicity, the freezable free water and freezable bound water may be grouped together as freezable water. The non-freezable water is that portion which is strongly hydrogen-bonded and hence bound to the repeat units of the polymer network. This portion of the water does not freeze at the regular freezing temperature of water and is not easily removed from the hydrogel. The freezable water is taken to be the water of solvation that occupies the interstices or nano-voids created by the balance of the solvation of the repeat units of the macromolecular chains that leads to an expansion of the network (the swelling force) and the counter balancing elastic force of the cross-linked structure (the retractive force) [133]. This water freezes at the regular freezing temperature of water and is readily removed from the hydrogel.

In addition to the DoH and water distribution within hydrogels, the Young's or elastic Modulus is paramount in determining favorable cell biomaterial interaction and has implication for the indwelling performance of implantable devices. In recent work, Guiseppi-Elie et al. demonstrated a clear relationship between the elastic modulus and the free:bound water ratio in poly(HEMA)-based hydrogels [130]. An increase in the free:bound water ratio parallels an increase in elastic modulus [130]. Additionally, attachment dependent RMS13 human muscle fibroblasts were shown to increase their *in vitro* attachment and proliferation at lower elastic modulus and lower free:bound water content that corresponded to lower cross-link density [134].

As such, changes of the elastic modulus and water content within hydrogels through the inclusion of hydrophobic [135, 136], protic and hydrogen bonding moieties [137], cationogenic [138] and zwitterionic moieties [139], has become a subject of interest in polymeric biomaterials research. Once modified to have the appropriate biomimetic properties, poly(HEMA)-based hydrogels have the potential to function as the biocompatible interface between a biotransducers (ABIO) and the local site of implantation (BIO) within the human body [124].

In this work is sought a pH-responsive hydrogel suitable for short-term intramuscular implantation capable of measuring tissue acidosis pursuant to hypoxia. The ideal hydrogel has optimized surface chemistry, molecular architecture, nanoscopic through mesoscopic structure, and mechanical properties that work in tandem to mitigate the pro-inflammatory response and minimize eventual fibrous encapsulation in order to maximize the bioanalytical performance of an implanted biotransducer. While a wide array of monomer constituents and chemical modifiers are known to influence pH-response, a major challenge is the lack of systematic understanding of the impact of individual hydrogel constituents on the water content and water distribution and how this may influence relevant physicochemical properties. The two monomer, amino ethyl methacrylate (AEMA) and dimethyl amino ethyl methacrylate (DMAEMA) were selected for the similarities of their pK_a values of 8.46 and 7.84 respectively, [140] [141] but contrasting hydrophobicity indices, -3.5 and 3.8 respectively . The reference monomer HEMA has a hydrophobicity index of -0.8 [75].

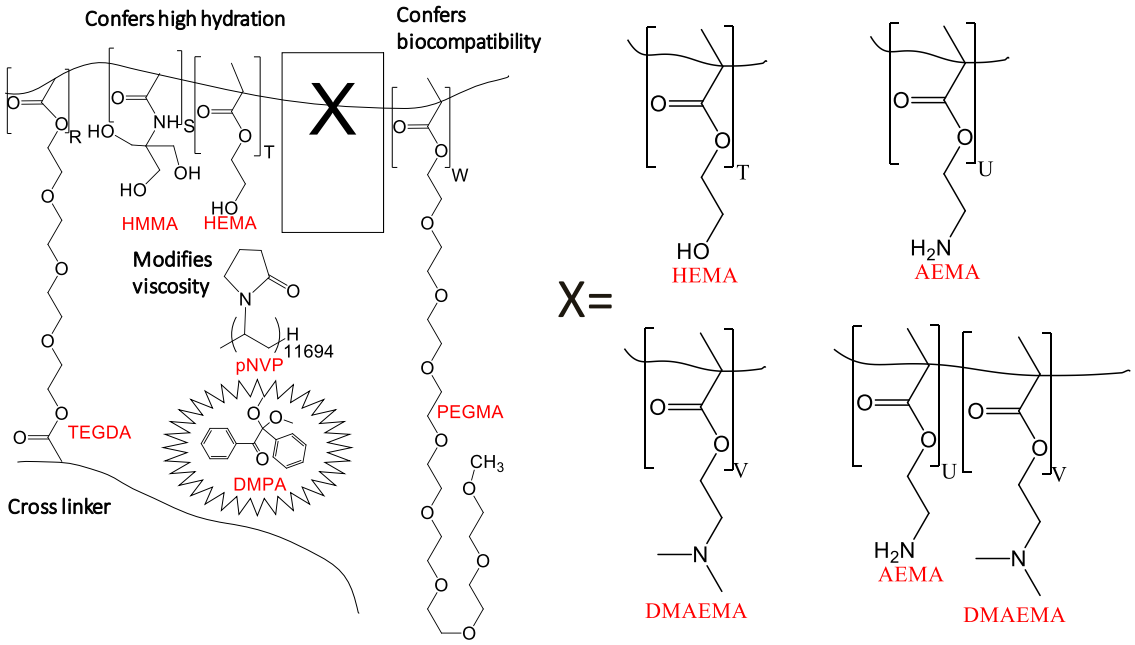

Figure 11. Schematic illustration of the various components of poly(HEMA-co-PEGMA)-based hydrogels explored in this study.

The monomer constituents characterized in this study include HEMA, AEMA and DMAEMA, the chemical structures and end-groups of which are shown in **Figure 11**. As seen from **Figure 11**, the hydroxyl end-group in HEMA (-OH), a common monomer used in hydrogel formulation [142], was responsible for the hydrophilic property. Similarly, the primary amine group of AEMA ($-NH_2 \leftrightarrow -NH_3^+$) and the tertiary amine end-group of DMAEMA ($–N-(CH_3)_2 \leftrightarrow (–NH^+-(CH_3)_2$) were responsible for the reactive and relatively hydrophilic, and relatively hydrophobic behavior of the constituents. The combined presence of the hydrophobic and ionizable tertiary amine in DMAEMA and the reactive primary amine in AEMA were expected to have an impact on hydration characteristics of the hydrogels.

This study reveals that inclusion of functional monomers in minor amounts (~4 mol%) does not significantly impact the water content but significantly impacts the water distribution. Compared to reference HEMA hydrogel, hydrophilic and ionizable AEMA maintains similar

hydration, water distribution, elastic modulus, and protein adsorption, however, it showed higher membrane resistance at pH 7.4 under differing temperature conditions. The hydrophobic and ionizable DMAEMA had lower total hydration, achieved at the sacrifice of the bound water content. The impact of these subtle changes was observed in an increase of the elastic modulus, an increase of the membrane resistance, and an increase of protein adsorption. Hydrogels with both AEMA (2 mol%) and DMAEMA (2 mol%) exhibited behavior that shifted preferentially toward DMAEMA with regard to water content and towards AEMA with regard to the measured physiochemical properties.

2.2 Chemicals and reagents

The monomers 2-hydroxyethyl methacrylate (HEMA), poly(ethylene glycol)(360)methacrylate (PEG(360)MA), N-[tris(hydroxymethyl)methyl]acrylamide (HMMA, 93%), N-(2-aminoethyl) methacrylamide (AEMA, 90%), N,N-(2-dimethylamino)ethyl methacrylamide (DMAEMA, 98%), the cross-linker tetra(ethylene glycol) diacrylate (TEGDA, technical grade), the biocompatible viscosity modifier polyvinylpyrrolidone (pNVP, MW ~1,300,000) and the photo-initiator 2,2-dimethoxy-2-phenylacetophenone (DMPA, 99+%) were purchased from Sigma Aldrich Co. (St. Louis, MO, USA). Methacrylate and diacrylate reagents were passed through an (removal column (306312, Sigma-Aldrich Co., St. Louis, MO) in order to remove the polymerization inhibitors hydroquinone and monomethyl ether hydroquinone. The buffer formed from 4-(2-hydroxyethyl)-1-piperazineethanesulfonic acid sodium salt (HEPES) was prepared to physiologically relevant conditions of 25 mM and pH = 7.4. A Milli-Q® plus (Millipore Inc., Bedford, MA) ultrapure water system was used to prepare deionized water. All other common chemicals and solvents were purchased from Sigma Aldrich Co. (St. Louis, MO, USA) and were used as received, unless otherwise stated.

2.2.1 Hydrogel cocktail formulation and polymer synthesis

All monomers were handled in a UV-free laboratory with UV filtering sleeves (TG-T8TG-UV, Lightbulbsurplus.com) placed over the fluorescent light bulbs. Four unique hydrogel pre-polymer formulations were prepared that varied in composition and were synthesized from HEMA, DMAEMA and AEMA by varying 4-mol% (nominally) of the responsive constituent. **Table 2** lists the hydrogel constituents and their exact molar composition. Thus, all hydrogels comprised 80 mol% HEMA. The formulation referenced as 4-mol% HEMA contained an additional 4-mol% HEMA to a total of 84-mol% HEMA and served as a reference formulation.

Other hydrogels were formulated by replacing the 4-mol% HEMA with 4-mol% AEMA, 4-mol% DMAEMA, or a mixture of comprising 2-mol% AEMA and 2-mol% DMAEMA. To improve component solubility, a mixed solvent comprising 1:1 (v/v) ratio of ethylene glycol and DI water was added to the mixture such that it comprised 20 volume% of the formulation. Finally, the mixture was ultrasonicated for 5 min and sparged with nitrogen gas to remove dissolved oxygen prior to casting and crosslinking.

Table 2. Monomer composition (mol%) for all four poly(HEMA)-based hydrogel formulations containing 4 mol% HEMA, 4 mol% AEMA, 4 mol% DMAEMA, and 2 mol% AEMA + 2 mol% DMAEMA.

Polymer constituents	Mol% of monomer components			
	4-mol% HEMA	4-mol% AEMA	4-mol% DMAEMA	2-mol% AEMA 2-mol% DMAEMA
HEMA (Base monomer: hydrophilic)	79.8	79.8	79.8	79.8
TEGDA (Cross-linker)	3.3	3.3	3.3	3.3
PEGMA(360) (Confers biocompatibility)	5.8	5.8	5.8	5.8
HMMA (Support monomer: hydrophilic)	4.4	4.4	4.4	4.4
pNVP (Pre-polymer: Increases viscosity) (on the basis of repeat unit structure)	1.9	1.9	1.9	1.9
HEMA (Monomer: hydrophilic)	4.4	0	0	0
AEMA (Monomer: hydrophilic)	0	4.4	0	2.2
DMAEMA (Monomer: hydrophobic)	0	0	4.4	2.2
DMPA (Photoinitiator)	0.4	0.4	0.4	0.4

To prepare hydrogel samples for characterization and testing, the hydrogel formulations were cast inside press-to-seal silicone isolator chambers (JTR12R-2.0, Grace Biolabs, Bend, OR) comprising 12 each of 4.5 mm diameter x 1.6 mm depth that were placed between two hydrophobicly prepared glass slides. Prior to casting, both sides of the glass slides were thoroughly degreased with acetone, UV cleaned for 10 min (UV-ozone Cleaner, Boekel Industries Inc., Feasterville, PA) and sonicated in isopropyl alcohol to further remove contaminants. The slides were then plasma cleaned (Plasma cleaner/sterilizer PDC-32 G, Harrick

Plasma, Ithaca, NY) to activate –OH groups and immediately incubated in a freshly prepared solution of 0.1% octadecyltrichlorosilane (OTS) in toluene for 45 minutes. The glass slides were then sonicated in isopropyl alcohol for 5 minutes and the silanol condensation with –OH groups of the glass allowed to proceed in an oven by sequentially heating to 40, 110, and 40°C for 20 minutes at each temperature. The isolator was pressed to one glass slide and each chamber filled with the hydrogel cocktail. The second glass slide was then gently lowered onto the chambers. Hydrogels were UV cross-linked for five minutes (CX-2000, UVP, Upland, CA). Upon completion of cross-linking, the polymerized hydrogels were removed from the glass slides and gradually hydrated and unreacted monomer extracted by soaking for one hour each in ethanol (99%) and 25 mM HEPES buffer (pH 7.4) mixtures in proportions of 100/0, 75/25, 50/50, 25/75 and 0/100 (mL/mL %). Ethylene glycol diffuses out completely by the extraction/hydration procedure used as it does not cross-link or become entrapped within the hydrogel. Such a progression in extraction helps to ensure that ethylene glycol is completely removed before the test of hydrogel properties.

2.3 Characterization of Hydrogels

2.3.1 Hydration via gravimetry

The degree of hydration (DoH) of the hydrogels was determined using gravimetric analysis. Hydrogel discs were weighed following equilibrium hydration (W_h) and then weighed again once they were completely dehydrated (W_d). Dehydration was accomplished by storing hydrogels in an -80°C freezer for twelve hours and then lyophilizing them for two days under 0.01 mbarr at -50°C. DoH was then calculated using Eq. (7).

$$DoH = \frac{W_h - W_d}{W_h} \times 100 \qquad (7)$$

2.3.2 Water distribution via Differential Scanning Calorimetry (DSC)

Thermal analysis was performed using a differential scanning calorimeter (Q2000, TA Instruments, New Castle, DE). Following established methods [143], wherein, approximately 5-10 mg of hydrated hydrogel was sealed into a hermetic pan (Tzero hermetic lid, 901684.901; Tzero pan, 901683.901), equilibrated at -40°C and heated to 30°C at 10°C/min under purging nitrogen (50mL/min). The enthalpic contribution, ΔH_m, of hydrogels at 0°C was then found by integrating the endothermic peak in TA Universal analysis software and then normalizing the data with respect to W_h. Assuming the enthalpy of the freezable and bound water to be the same as that of bulk water (ΔH_0 = 334 J/g), the freezable free water content was calculated using Eq. (8), and the non-freezable bound water content was calculated using Eq. (9).

$$\frac{W_f}{W_h}(wt\%) = \frac{\Delta H_m}{\Delta H_0} \times 100 \quad (8)$$

$$\frac{W_{\text{nfb}}}{W_h}(wt\%) = DoH - \frac{W_f}{W_h} \quad (9)$$

To determine the glass transition temperature (T_g) of the hydrogels, samples were first dehydrated then placed and sealed into hermetic pans (Tzero hermetic lid, 901684.901; Tzero pan, 901683.901), equilibrated at -20°C and heated to 200°C at 10°C/min for two cycles. The first cycle was performed in order to erase the thermal history of the hydrogels, and the second cycle was performed in order to determine the inherent thermal properties of the hydrogels. The T_g was determined by extrapolation of thermal trace data using TA Universal Analysis software.

2.3.3 Electrical Impedance spectroscopy

The electrical conductivity of hydrogels, while not extensively studied, has implications for cytocompatibility, cellular attachment and differentiation [144] and appears to manifest through differences in hydration. EIS, along with equivalent circuit modeling, provides a

convenient means to determine hydrogel membrane resistance. For a hydrogel system represented by a simplified Randles equivalent circuit of a series membrane resistor (R_M) and a parallel arrangement of an interfacial charge transfer resistor (R_{CT}) and a double layer capacitor elements, impedance (Z) is represented as a function of its capacitance (C) and frequency (f) (Eq. 10, Eq.11 and Eq. 12) [78]:

$$Z' = R_M + \frac{R_{ct}}{1+(\omega C_{dl} R_{ct})^2} \quad (10)$$

$$Z'' = -\frac{\omega C_{dl} R_{ct}^2}{1+(\omega C_{dl} R_{ct})^2} \quad (11)$$

$$\left(Z' - R_M - {R_{ct}}/{2}\right)^2 + (Z'')^2 = \left({R_{ct}}/{2}\right)^2 \quad (12)$$

The hydrogel membrane resistance is reflective of the volume density and state of ionization of ionogenic groups within, the type of bathing ions and their concentration that partition into the hydrogel, and temperature. The real (Z') and imaginary (Z") components of the complex impedance presented via the Nyquist plot establishes an idealized semicircle. The depressed semicircles in Nyquist plots indicate pseudocapacitance arising due to a frequency power (n) value between 0 and 1 (*n*=0 being a pure resistor and *n*=1 being a pure capacitor)[145]. For an admittance Y_0 the pseudocapacitance is given as (Eq. 13):

$$C_{pseudo} = \frac{(Y_0 R_{ct})^{1/n}}{R_M} \quad (13)$$

Hydrogel cocktails were pipetted into the wells (ϕ=4.5 mm and T=1.6 mm) of singulated, non-adhesive, press-to-seal silicone isolators (JTR12R, Grace Biolabs, Bend, OR) that were supported on OTS-silanized glass microscope slides. Following UV cross-linking, slides were removed, hydrogels were kept within the isolators then hydrated and extracted by sequentially soaking for one hour each in ethanol (99%) and 25 mM HEPES buffer (pH 7.4) mixtures in

proportions of 100/0, 75/25, 50/50, 25/75 and 0/100 (mL/mL %). Finally, hydrogels were equilibrated overnight in HEPES buffer of nominal pH 7.4. Following equilibration, two stainless steel mesh electrodes (5.0 mm x 50 mm) (SS Type 304, ϕ= 0.0075 in, 60 per inch, TWP, Inc., Berkeley, CA) that were degreased in boiling methylene chloride, rinsed profusely in isopropyl alcohol, rinsed profusely in DI water and blown dry with nitrogen gas, were assembled, one on either side of the silicone isolator chamber that contained the cross-linked hydrogel. The assembly was then clamped with a plastic clip (**Figure 12**) and returned to the pH 7.4 HEPES buffer solution where it was allowed to equilibrate overnight. Immediately before the EIS measurements, the samples were removed from the buffer and quickly blown with nitrogen gas to remove excess liquid.

All EIS measurements were carried out over the range 0.01 Hz – 1 MHz using 10 mV p-t-p sine wave (5 points per decade) with zero offset voltage. Measurements were done at room temperature (21 °C) in air or under physiologic conditions in an incubator at 37 °C and 5% CO_2 using a VersaStat 4 (Princeton Applied Research, AMETEK, Inc., Oak Ridge, TN). Impedance spectra of Bode plots (impedance magnitude, $|Z|$, and phase, θ, *vs.* frequency) and Nyquist plots (Z_{real} versus Z_{img}) were derived directly from the software provided with the instrument (VersaStudio version 1.51, AMETEK, Inc., Oak Ridge, TN). Further data analysis using ZSimpWin software version 3.60 (AMETEK, Inc., Oak Ridge, TN) with a modified Randles equivalent circuit model R(QR) resolved the membrane resistance, R_M, charge transfer resistance, R_{CT}, and the double layer capacitance, Q_{DL}, or constant phase element (CPE).

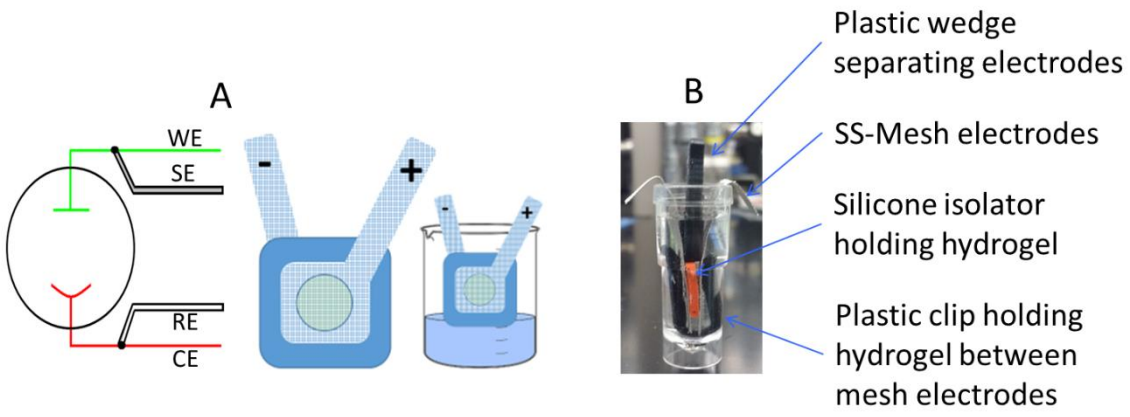

Figure 12. (A) Schematic illustration of the device under test showing the 2-electrode setup for electrical impedance spectroscopy and (B) setup of the electrode assembly with ss-mesh electrodes clamped on either side of equilibrated hydrogel discs within silicone isolator molds.

2.3.4 Surface Morphology of hydrogels using Scanning Electron Microscopy(SEM)

Hydrated hydrogels were freeze-fractured using liquid nitrogen. The freeze-fractured hydrogels were dried for 48 hours in a closed cell concentrator (TurboVap 500, Zymark, St. Cridersville, OH) and stored in a desiccator cabinet (Fisherbrand, Hampton, NH) until use. Desiccated hydrogels were mounted onto sample holders using double-sided, conductive carbon tape such that their freeze-fractured surfaces were exposed and were sputter-coated with a 5 nm thick platinum/palladium layer using a Cressington 208HR High Resolution Sputter Coater equipped with a MTM-20 thickness controller (Cressington Scientific Instruments, UK). A small piece of carbon tape was placed on one side of the hydrogels. This was done to dissipate the charging of the sample while imaging. SEM imaging was conducted using a JEOL JSM-7500F FE-SEM at 3.0 kV at magnification of x2.5k.

2.3.5 Elastic modulus of hydrogels

The elastic modulus of fully hydrated hydrogels (25 mM HEPES buffer, pH 7.4) was measured using an Instron 3345 (Norwood, MA) equipped with 1 kN pre-load cell. The accompanying Instron Bluehill software was used to note the dimensions of the hydrogel sample. Using compression-extension mode in the software, the elastic modulus of fully hydrated hydrogels was tested with a 0.1 N pre-load force over 5% strain at the rate of 1 mm/min. The elastic modulus was extracted from the linear part of the stress-strain curve and noted in kPa.

2.3.6 Protein adsorption on hydrogels

Protein adsorption is a key factor in the biological response to implantable devices and is the governing event in cell signaling for the foreign body response [146], the inflammatory cascade [147] and the blood coagulation cascade [148]. Protein adsorption is therefore important for engineered tissue scaffolds and implantable biosensors [149, 150]. Shortly after intravascular implantation, plasma proteins such as albumin, fibrinogen, immunoglobulin G, fibronectin, and von Willebrand factor adsorb onto the biomaterial's surface and undergo conformational changes that signal to initiate inflammation, coagulation, and the foreign body response [151]. Of these proteins, albumin is often used to determine the blood compatibility of prepared hydrogels [152] as its extremely high serum content and ability to complex with other proteins gives it an influential role in the competitive adsorption of proteins from biological environments [153]. The commonality of protein interactions in biological processes coupled with the complexity of the mechanisms behind protein adsorption has led to an increased drive to research protein adsorption on engineered surfaces [149] and the effect seen on protein adsorption with different surface characteristics, such as hydrophobic versus hydrophilic surfaces [151].

Hydrogel cocktails representing the four variants under study were cast (40 µL), UV-crosslinked and simultaneously covalently attached via NHS-PEG-acryloyl conjugates [154] to the bottom of the wells of 96-well polystyrene multi-well plates that were chemically modified by treatment for one minute with acidified permanganate (H_2SO_4/K_2Mn0_4) [154]. Hydrogels were then hydrated in PBS 7.4. FITC-tagged albumin was prepared at twelve unique concentrations; 0.1, 0.3, 0.5, 1, 3, 5, 10, 30, 50, 100, 300, 500 µg/mL in PBS 7.4 buffer and the hydrogels covered in 50 µL of each solution in the dark for overnight incubation at RT. Following adsorption, the loosely adsorbed proteins were removed under running DI water for five minutes, wells immediately rinsed with PBS buffer and each well scanned using a Cytation-5 (BioTek Instruments). Adsorption isotherms [155] were constructed from triplicate measures of fluorescence intensities at each concentration using the Langmuir Adsorption Isotherm equation (Eq. 14)

$$Q = Qmax\frac{K\,[A]}{1+K[A]} \qquad (14)$$

Where Q_{max} is the maximum protein adsorption capacity, Q is protein adsorption capacity and K is the equilibrium constant given by (Eq. 15)

$$K = \frac{[AB]}{[A][B]} \qquad (15)$$

[A] is the molar concentration of adsorbate (proteins) and [B] is the molar concentration of adsorbent sites on the hydrogels. The Langmuir isotherm has long been used to describe the adsorption of proteins onto biopolymer surfaces and, as in this case, was often found to have the best fit relative to other isotherm models [156].

2.3.7 Statistical Analysis

For hydrogel water content, the results were presented as the mean ± 95% confidence intervals (C.I.), with n = 3. The statistical significance of differences between mean values for different samples was evaluated using the Student's t-test with values of $p < 0.05$ being considered as statistically significant. The results for the Young's Modulus of the hydrogels was presented as an average value and standard deviation for each hydrogel formulation with n = 500. For impedance at room temperature and physiological temperature, the values were represented as an average value and standard deviation for each hydrogel formulation with n = 3. For protein adsorption, the statistical significance was assessed from the predicted intervals.

2.3.8 Partition coefficients and hydrophobicity indices for HEMA, AEMA and DMAEMA monomers

2.3.8.1 Calculations for partition coefficients

Partition coefficient (unit less), $P = [X]_{organic} / [X]_{aqueous}$, is the ratio of molar concentrations (mol/L) in contacting phases [143], generally an organic phase vs the aqueous phase (page 1112, Sangster).[157] When $\log P > 0$, $P > 1$; $[X]_{org} > [X]_{aq}$ and when $\log P < 0$, $P < 1$; $[X]_{org} < [X]_{aq}$.

As monomers HEMA, AEMA and DMAEMA differ only with respect to their functional groups OH, NH_2, and $N(CH_3)_3$ respectively, it is assumed that only these functional groups contribute to the partition coefficients.

For CH_3OH, CH_3NH_2, $N(CH_3)_3$; log P values were calculated to be -0.74 (table 9, page 1150, Sangster), -0.57 (table 15, page 1192, Sangster), 0.16 (table 15, page 1193, Sangster) respectively.[157] For CH_3OH and CH_3NH_2 the log P values are negative indicating hydrophilicity. For $N(CH_3)_3$, log P is 0.16 (positive), indicating hydrophobicity. These values

serve to provide a relative ranking of the monomer along a continuum from highly hydrophilic to hydrophobic.

2.3.8.2 Evaluating the hydrophobicity indices of the monomers using Kyte-Doolittle scale (for amino acids) [158]

Kyte-Doolittle scale[158] lists the hydrophobicity indices of amino acids. We allocated these hydrophobicity indices to our monomers based on their functional group similarity with the R-groups of amino acids.

2.4 Results and Discussion

The monomers used in the hydrogel cocktail were of similar molecular weights, diffusivities and chemical reactivity and the hydrogel was formed by random co-polymerization. Hence, the composition of the resulting polymer product was expected to reflect the composition of the starting reactants. Also, the cross-linker, TEGDA, was consistently used at 3 mol% in each of the compositions of HEMA, AEMA and DMAEMA. The degree of cross-linking has been well established to have a significant effect on the biotechnical performance hydrogels. In previous work by Guiseppi-Elie et al [159] it was established that the cross-link density was inversely proportional to swelling and that the measured and calculated degree of cross-linking was reflective of the mol % cross-linker in the starting reaction cocktail.

2.4.1 Water Content and Distribution

The degree of hydration as determined by gravimetric analysis and the free and bound water content as determined by DSC of the four hydrogel formulations are detailed in **Table 3**.

Table 3. Hydration, water distribution (25 °C, DI water) and glass transition temperature, Tg, for all four poly(HEMA)-based hydrogel formulations containing 4 mol% HEMA, 4 mol% AEMA, 4 mol% DMAEMA, and 2 mol% AEMA + 2 mol% DMAEMA.

Property	4-mol% HEMA	4-mol% AEMA	4-mol% DMAEMA	2-mol% AEMA 2-mol% DMAEMA
Degree of hydration at 25°C DoH (wt%)	39.3±0.4	39.0±0.2	35.5±0.3	38.7±0.2
% Δ	0.0%	-0.8%	-9.7%	-1.5%
Freezable water $\frac{W_f}{M_{HG}}$ (wt%)	3.8±0.69	3.8±0.4	5.5±0.8	5.4±0.4
% Δ	0.0%	0.0%	44.7%	42.1%
Non-Freezable bound water $\frac{W_{nfb}}{M_{HG}}$ (wt%)	35.5±0.69	35.2±0.4	30.0±0.8	33.3±0.4
% Δ	0.0%	-0.8%	-15.5%	-6.2%
T_g (°C)	93.2 ± 2.9	86.3 ± 1.3	114.2 ± 0.7	96.3 ± 0.4

It is immediately apparent that the total hydration among the four formulations is not dramatically different. However, close inspection reveals that the distribution of water among free and bound states was significantly different ($p < 0.05$). Of the 39.3% total hydration of the poly(HEMA) hydrogel, 91% was non-freezable, bound water and 9% was freezable, free water. The replacement of 4 mol% HEMA with 4 mol% AEMA made no difference to the total hydration (~ 1% change) or the distribution of water, suggesting that at this level, there is equivalence of the –OH and the $–NH_2$ moieties. However, the replacement of 4 mol% HEMA with 4mol% DMAEMA resulted in a reduction in total hydration by 15 % and a change in the distribution of water such that of the 35.5% total hydration of the poly(HEMA-4 mol% DMAEMA) hydrogel, 85% was non-freezable, bound water and 15% was freezable, free water. When 4 mol% HEMA was replaced with 2 mol% AEMA and 2 mol% DMAEMA there resulted no difference in total hydration (~ 2% change), a behavior that was dominated by the presence of

the 2 mol% AEMA. However, the distribution of water changed such that of the 38.7 % total hydration of the poly(HEMA-2 mol% AEMA-2 mol% DMAEMA) hydrogel, 86% was non-freezable, bound water and 14% was freezable free water, a behavior that was dominated by the presence of the 2 mol% DMAEMA.

The bound water is an integral part of the hydrogel polymer network through hydrogen bonding. The implication of this is that bound water is not freezable at the regular freezing point of water. The free water, on the other hand, is water not directly hydrogen-bonded to the polymer network, which may be readily removed and/or frozen at 0°C. These changes are more clearly illustrated in **Figure 13** that plots the change in water content of all three other hydrogels relative to the reference hydrogel with 4 mol% HEMA. These changes and their statistical significance are now clearly discernable as percentage increases and decreases relative to the reference hydrogel with 4 mol% HEMA.

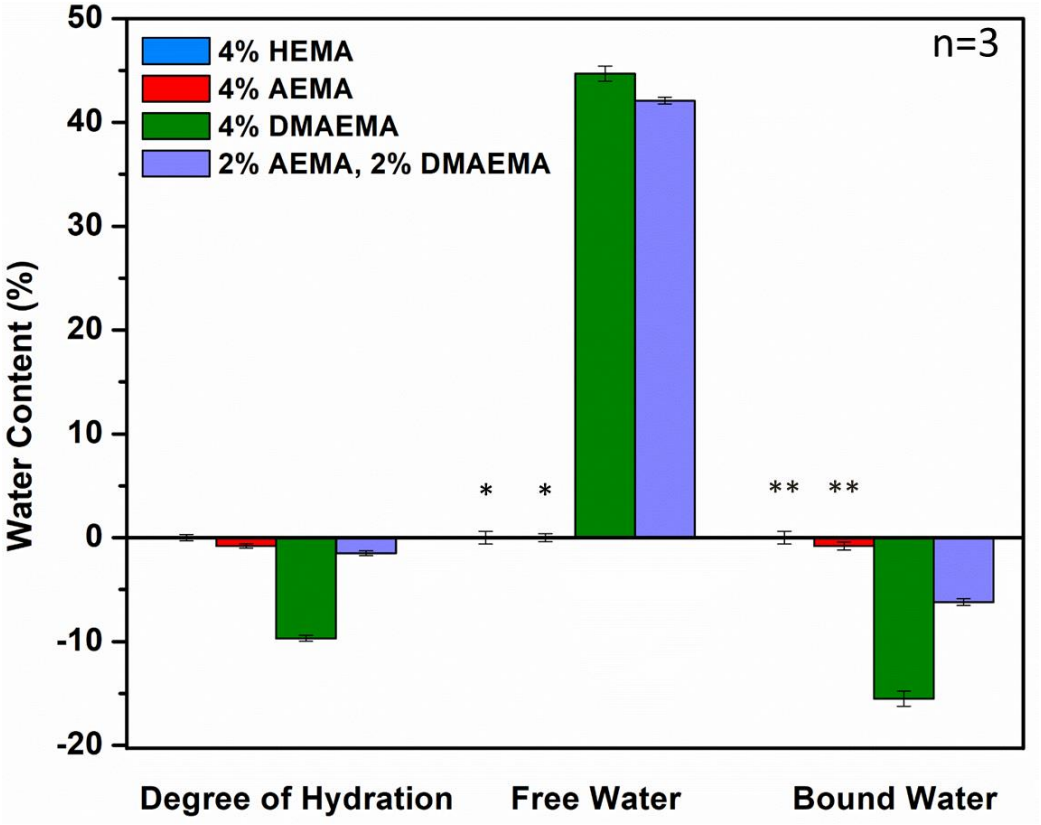

Figure 13. Relative changes in the degree of hydration, free water content, and bound water content of poly(HEMA)-based hydrogel containing 4 mol% HEMA (blue), 4 mol% AEMA (red), 4 mol% DMAEMA (green) and 2 mol% AEMA + 2 mol% DMAEMA (purple).

The glass transition temperature (T_g) of hydrogels was determined using DSC [75]. Values were obtained from the second DSC heating cycle, erasing any influence from the thermal history of the hydrogels. T_g provides insight into the dynamics of the amorphous phase of a solid material. The T_g is the temperature at which there is an increase in segmental mobility of the polymer backbone. Materials are in a rubbery, soft state above their T_g and in a glassy, hard state bellow their T_g. This transition is dependent on the flexibility of the polymer chains, which for hydrogels is highly influenced by water content (plasticizer effect). In previous studies, the T_g has been found to be inversely related to the amount of bound water, with an increase in bound water leading to a decrease in the T_g [130]. Thus, analysis of T_g is relevant and

for similarly cross-linked polymers allows comparative insight into hydrogel water distribution. The T_g for the control hydrogel was found to be 93.2 ±2.9°C while the replacement of 4 mol% HEMA with 4 mol% AEMA reduced the T_g to 86.3 ± 1.3°C, which was not significantly different, and replacement with 4 mol% DMAEMA increased the T_g to 114.2 ± 0.7°C, which was significantly different. The T_g values reported in the literature for poly(HEMA) hydrogels vary generally from roughly 67°C - 100°C [143, 160] depending on factors such as drying procedure, method of measurement, original water content, and of course, the amount of crosslinker used. The results from the current study does fall within this range. The wide variations in T_g values from the literature were due to the variations in cross-linking density, the overall water content, and drying method used prior to DSC. In general, higher water content generally lowered the T_g values. However, as this study shows, it may not just be hydration but rather specifically, bound water content, which is most influential. The higher T_g obtained for the hydrogel containing 4 mol% DMAEMA was accompanied by lower total hydration but also by lower non-freezable, bound water.

The relative similarity in the water content, the distribution of water, and T_g when 4 mol% HEMA was replaced with 4 mol% AEMA was not surprising as both HEMA and AEMA are relatively hydrophilic monomers with relatively similarly sized functional groups. The replacement of 4 mol% HEMA with 4-mol% DMAEMA had a significant impact on water content and the distribution of water. DMAEMA decreased the bound water content by ~14% while increasing the free water content by ~45% relative to the control hydrogels. The modest decrease in total hydration, the major shift in the water distribution and the increase in T_g were all expected and are consistent with previous studies [130]. DMAEMA, unlike the HEMA and AEMA, is a relatively hydrophobic and bulkier moiety. The inclusion of DMAEMA was thus

expected to cause a decrease in the hydrogels ability to strongly bind water, leading to higher free water content and lower bound water content. The lower bound water also raised the energy required to incite mobility in the polymer chains within the hydrogel. That this effect could be realized with a mere 4 mol% DMAEMA was surprising.

The effect of 2 mol% AEMA and 2 mol% DMAEMA mixture on the water content and distribution was likewise interesting. In general, the overall water content and the T_g for these hydrogels were statistically similar to that of poly(HEMA). However, the amount of bound water was reduced by a factor of ~6%, and the free water increased by a factor of 42% relative to the equivalent water content in poly(HEMA) hydrogel. The overall results were quite different from the individual addition of AEMA or DMAEMA. In fact, the T_g for the mixture was significantly different from that of the AEMA or the DMAEMA hydrogels. Based on the combined results, it was evident that the water content and distribution within a hydrogel with equivalent mixtures of hydrophilic and hydrophobic monomers do not follow the simple rule of mixtures but instead reflect a distinct behavior all its own. The degree of hydration calculated at pH 7.4 was shown to be the same regardless of molecular composition examined. This implies that the minor changes in composition did not significantly affect the gravimetrically determined degree of hydration. However, the water distribution in the hydrogels was changed dramatically, which in turn influences the key biotechnical properties.

2.4.2 Surface morphology

The surface morphology of freeze-fractured hydrogels as imaged by SEM is shown in **Figure 14**. The images illustrate the influence of water content and distribution on the micromechanics of fracture within the freeze-fractured surface of the hydrogels at x2.5k magnification. The images of all hydrogels appeared nearly featureless. The root mean square

surface roughness (Rq) for the four poly(HEMA)-based hydrogel formulations containing 4 mol% HEMA, 4 mol% AEMA, 4 mol% DMAEMA, and 2 mol% AEMA + 2 mol% DMAEMA was analyzed using the SurfChargeJ Plugin in ImageJ software[161] and were found to be 71.1, 68.2, 73.0 and 66.0 nm ,respectively.

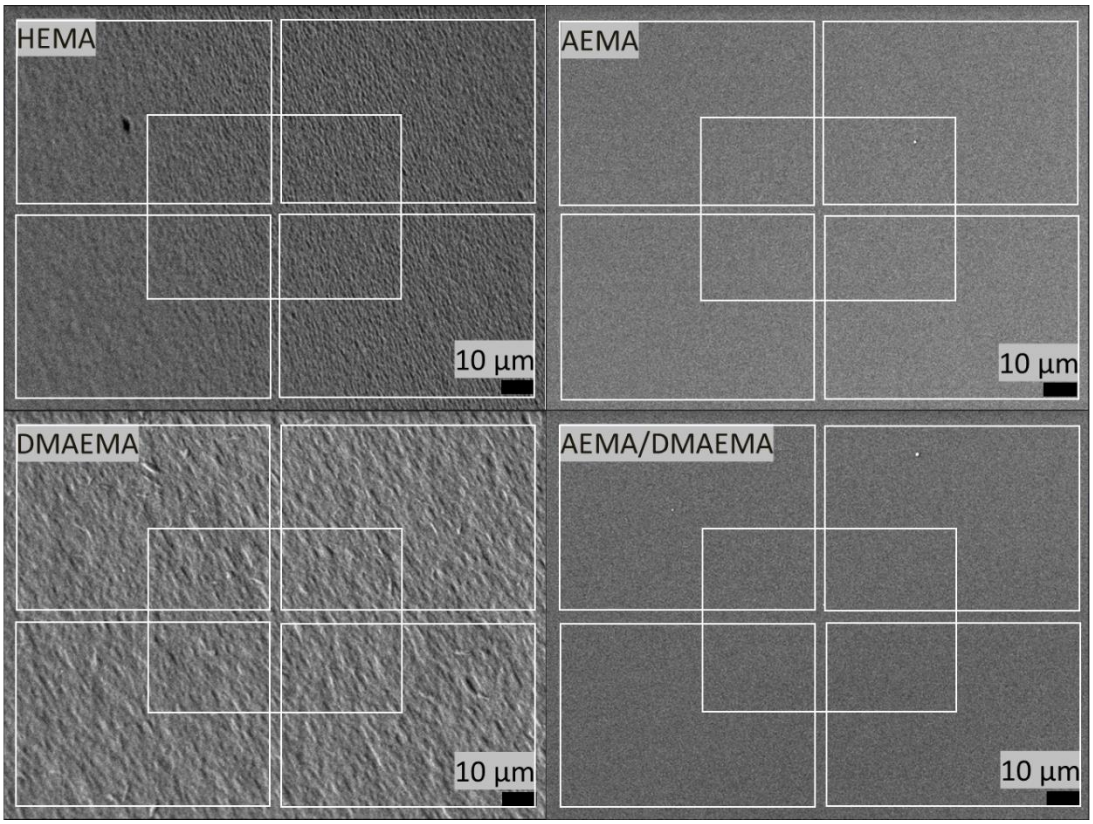

Figure 14. SEM images of poly(HEMA)-based hydrogel containing 4 mol% HEMA, 4 mol% AEMA, 4 mol% DMAEMA and 2 mol% AEMA + 2 mol% DMAEMA, each taken at acceleration voltage 3.0 kV and x2.5k magnification.

The measured root mean square surface roughness of the freeze-fractured polymers (**Table 4**) reflects the fracture pattern of a heterogeneous ice-in-polymer composite glass. At liquid nitrogen temperature, the freezable water coalesces into domains of ice crystals. The size of those crystals, the hydrogen bonded interaction between ice crystals and the surrounding polymer and the bonded water that influences inter and intra-chain hydrogen bonding among

polymer chain segments that may serve to plasticize the polymer combine to play a role in determining the surface roughness [162]. Fracture surfaces become more rough when the fracture velocity is high[163]. Relative to poly(HEMA), the hydrogel containing the hydrophobic moiety, DMAEMA, was shown to possess an increased amount of free water, a decreased amount of bound water and shows the highest surface roughness. The hydrogel containing the hydrophilic moiety, AEMA, was shown to possess a similar amounts of free and bound water show similar surface roughness as poly(HEMA). Although, the water content and distribution in AEMA/DMAEMA was dominated by DMAEMA, this hydrogel showed the least surface roughness out of the four subsystems.

2.4.3 Elastic Modulus

Instron was used to determine the force displacement characteristics of the hydrated hydrogel formulations, which were then used, along with the Hertz Model, to calculate the Young's Modulus for each hydrogel. The elastic moduli of the hydrogels with 4 mol% HEMA, 4 mol% AEMA, 4 mol% DMAEMA and 2 mol% AEMA/2 mol% DMAEMA were measured to be 3142 ± 1489 kPa, 1452 ± 41 kPa, 19036 ± 5233 kPa and 2067 ± 12 kPa respectively. **Figure 15** depicts the plot for the average elastic modulus of the hydrogels and the numerical values are displayed in **Table 4**. The Young's or elastic modulus indicates the stiffness or elasticity of the polymer as defined by the relationship between the stress (applied force) and strain (resultant deformation). A similar trend was observed between the average Young's Modulus and the glass transition temperature of the four hydrogel formulations. For instance, the lowest average Young's Modulus value observed is 1452 kPa for the AEMA hydrogel and the highest average Young's Modulus value observed is 19036 kPa for DMAEMA hydrogel, which is the same trend seen in the glass transition temperature. This was expected as the segmental polymer dynamics

are influenced by the water content of the hydrogels due to the plasticizing nature of water [130, 164]. Hydrogel formulations of HEMA, AEMA and AEMA/DMAEMA have statistically similar Young's Modulus values but DMAEMA has a high average value as well as a statistically different Young's modulus value than the other three types of hydrogels. This shows that in the poly(HEMA) hydrogel, the Young's Modulus of the hydrogel does not differ with the addition of AEMA or with a 50/50 composition of AEMA/DMAEMA but it is higher and significant with only DMAEMA.

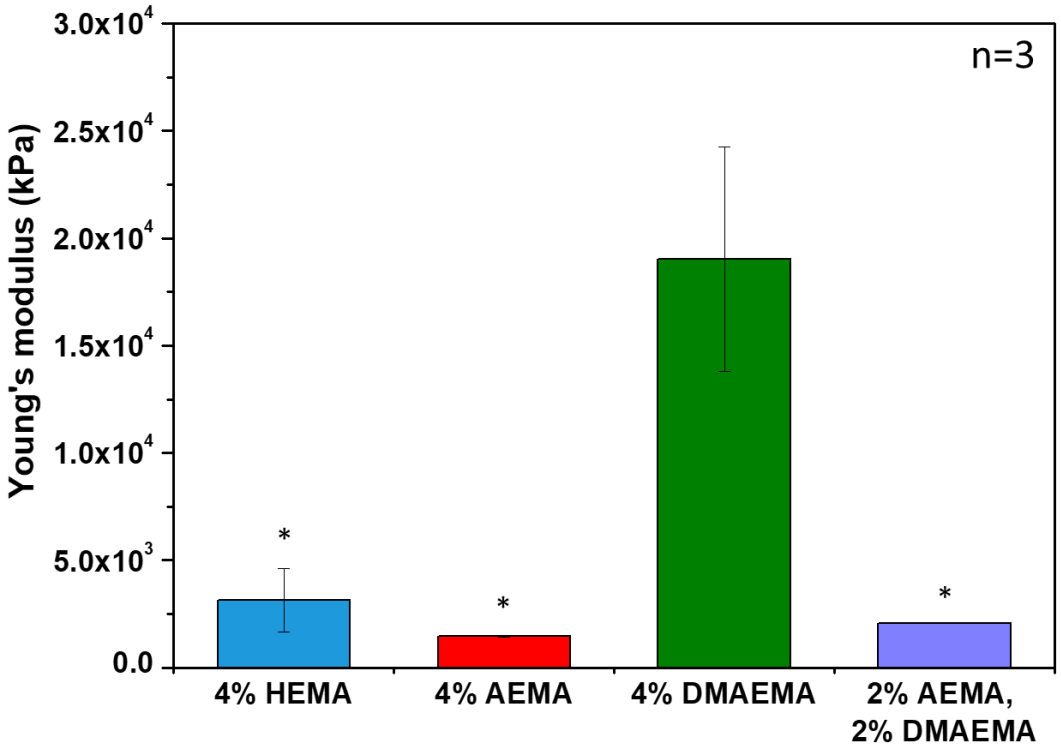

Figure 15. Elastic modulus (kPa) of poly(HEMA)-based hydrogel containing 4 mol% HEMA (blue), 4 mol% AEMA (red), 4 mol% DMAEMA (green), and 2 mol% AEMA + 2 mol% DMAEMA (purple).

Table 4. The root mean square surface roughness (Rq) values of freeze-fractured hydrogel surfaces determined using SurfChargeJ Plugin in ImageJ software (n=5) and the elastic modulus (kP) measured at RT for four poly(HEMA)-based hydrogel formulations containing 4 mol% HEMA, 4 mol% AEMA, 4 mol% DMAEMA, and 2 mol% AEMA + 2 mol% DMAEMA).

	4% HEMA	4% AEMA	4% DMAEMA	2% AEMA and 2% DMAEMA
Rq (nm)	71	68	73	66
E (kPa) Average ± SD (kPa)	3,142 ±1489	1,452 ±41	19,036 ±5233	2,067 ±12

Given the equality of the total hydration among the engineered compositions, the differences in moduli may be attributed to the differences in the distribution of water within these hydrogels brought on by the small changes in molecular composition. A relative increase in free water and decrease in bound water content (4 mol% DMAEMA) suggests greater opportunities for intra and inter-chain hydrogen bonding (virtual crosslinks) that results in increased stiffness. Conversely, higher levels of bound water (4 mol% HEMA) are expected to effectively plasticize the polymer, thereby reducing the modulus. Despite the protonation of the 1° amines and the partitioning of corresponding electro neutralizing counter anions, the 4 mol% HEMA and 4 mol% AEMA have similar moduli in the polyelectrolyte[165]. Also, when the polymer possesses 2 mol% AEMA and 2 mol% DMAEMA, the distribution of water and elastic modulus are dominated by the presence of the DMAEMA. Additionally, the presence of ionogenic moieties (1° and 2° amines) potentially gives rise to electrostatic repulsion between polymer chains and ingress of solvated counter anions, thus improving the uptake of water [166].

2.4.4 Membrane Impedance

Electrochemical Impedance Spectroscopy (EIS) was used to assess the influence of hydration and water distribution on the membrane resistance (R_M) of the four uniquely formulated hydrogel compositions containing 4 mol% HEMA, 4 mol% AEMA, 4 mol% DMAEMA, and 2 mol% AEMA + 2 mol% DMAEMA. The measurements were carried out both at room temperature (RT, 21°C, 0.043% CO_2) and physiological conditions (PC, 37°C, 5% CO_2). Impedance spectra were obtained over the frequency range 0.01 Hz-1 MHz following equilibration in HEPES buffer at pH 7.4. Spectra were essentially similar and equivalent circuit modeling of the complex impedance data established an $[R_M(Q^nR_{CT})]$ resistor-capacitor network with robust goodness of fit ($Y^2<0.2$) that varied according to the chemical composition of the hydrogels. In this way the membrane resistance value, R_M, was extracted for each hydrogel under the tested conditions. The extracted parameters were then used to simulate the impendence spectra over a slightly wider range of frequencies (1 mHz - 100 MHz). **Figure 16** shows the Nyquist plots obtained from these simulations and **Figure 17** shows the R_M (Ω) values as a function of hydrogel composition in HEPES buffer. **Table 5** shows the equivalent circuit parameters extracted from $[R_M(Q^nR_{CT})]$ equivalent circuit modeling.

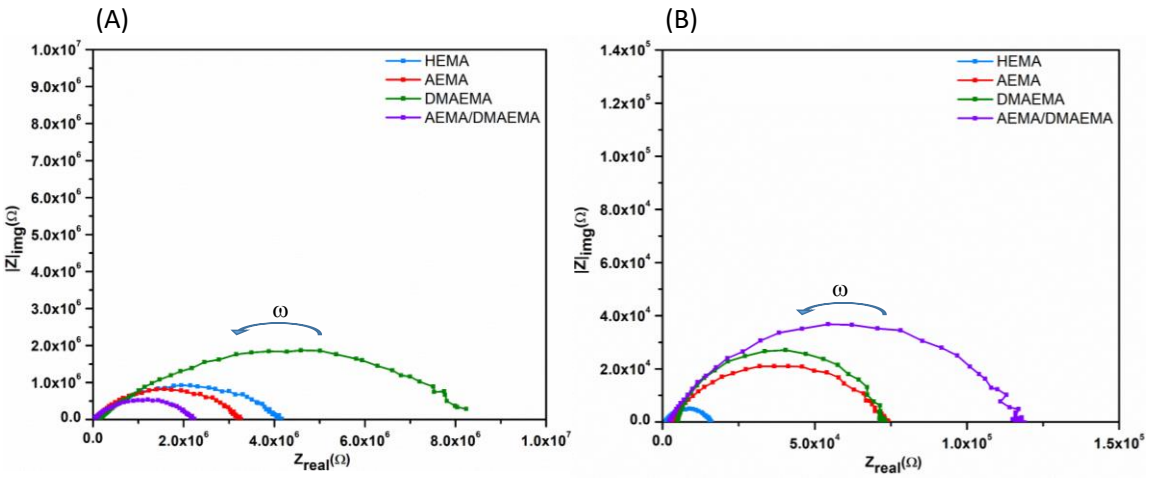

Figure 16. Nyquist plots of Zreal (Ω) vs. Zimag (Ω) for poly(HEMA)-based hydrogel containing 4 mol% HEMA (blue), 4 mol% AEMA (red), 4 mol% DMAEMA (green), and 2 mol% AEMA + 2 mol% DMAEMA (purple) in HEPES buffer at A) Room temperature (RT, 21 ºC, 0.043% CO_2) and B) Physiological conditions (PC, temperature 37 ºC, 5% CO_2). (n=3).

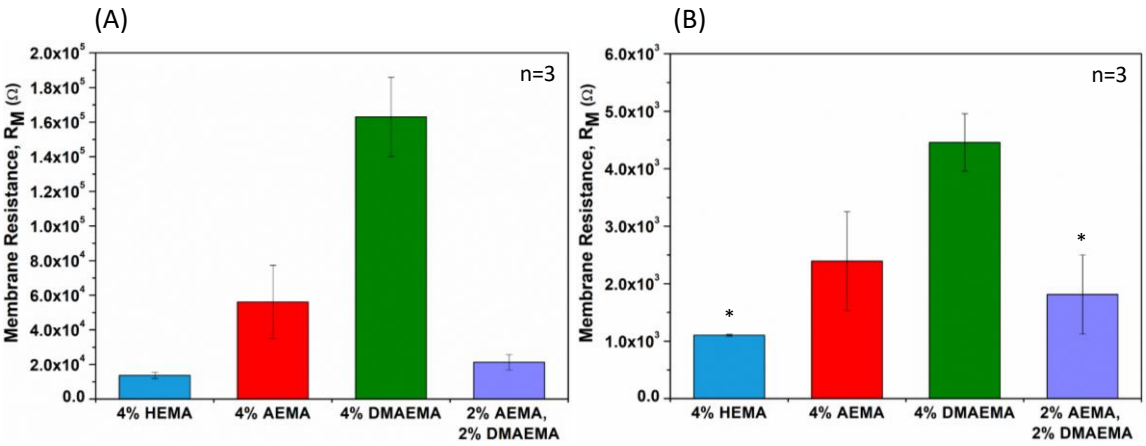

Figure 17. Graph of membrane resistance, R_M (Ω), extracted from R(QR) equivalent circuit analysis using ZSimpWin v3.60 software versus nominal pH 7.4 in pH-adjusted HEPES buffer at A) Room temperature (RT, 21 ºC, 0.043% CO_2) and B) Physiological conditions, (PC, 37 ºC, 5% CO_2).

Table 5. Equivalent circuit parameters extracted from R(QR) equivalent circuit analysis using ZSimpWin v3.60 software and using data obtained at pH 7.4 in pH-adjusted HEPES buffer at A) Room temperature (RT, 21 ºC, 0.043% CO_2), B) Physiological conditions (PC, temperature 37 ºC, 5% CO_2), and C) Calculated Resistances.

Hydrogel	Room Temperature					Physiological Conditions					Calculated resistances
	R_M(Ω)	Q ($S\text{-}s^n$)	n	R_{CT} (Ω)	χ^2	R_M (Ω)	Q ($S\text{-}s^n$)	n	R_{CT} (Ω)	χ^2	R_M(Ω)
HEMA	1.20E+04	1.60E-06	0.535	4.13E+06	0.107	1110	6.34E-04	0.750	1.48E+04	0.122	1.30E+04
AEMA	3.41E+04	2.98E-06	0.603	3.21E+06	0.152	2812	1.70E-05	0.692	7.05E+04	0.152	5.62E+04
DMAEMA	1.37E+05	3.94E-06	0.533	8.31E+06	0.258	4877	1.26E-05	0.858	6.75E+04	0.321	1.69E+05
AEMA/ DMAEMA	2.17E+04	7.42E-06	0.579	2.21E+06	0.120	2184	2.62E-06	0.724	1.15E+05	0.298	4.22E+04

As expected, the real and imaginary components of the complex impedance were lowered by an order of magnitude upon measurement under physiological conditions. Physiologic conditions contributes two key variables, an increased temperature that increases ionization and accordingly increases conductivity by 0.262/°C [167] and the presence of additional ions,

bicarbonate ions and protons in particular, formed by the dissolution of CO_2 (carbonic acid) $CO_2 + H_2O \leftrightarrow H_2CO_3 \leftrightarrow [H^+] + [HCO_3^-]$ [28]. Hydrogels fashioned exclusively from HEMA displayed the lowest membrane resistance under both conditions. Hydrogels fashioned with 4 mol% AEMA were similar, though somewhat more resistive than hydrogels fashioned from HEMA. Hydrogels fashioned with 4 mol% DMAEMA displayed the highest membrane resistance under both conditions and were 10-fold more resistive that p(HEMA). The simultaneous inclusion of AEMA and DMAEMA, each at 2 mol%, could be expected to behave, to a first approximation and in accord with the rule of mixtures, as the algebraic sum of contributions from the influences of the two separate monomer, that is, a simple rule of mixtures. However, this formulation behaved more like the hydrogels fashioned from 4 mol% AEMA suggesting the dominant importance of non-freezable bound water in influencing the resistance of the membranes.

The reference hydrogel (84.2 mol% HEMA) and those possessing minor amounts of AEMA and/or DMAEMA and their surrounding environment (HEPES buffer pH adjusted to 7.4 with NaOH) can be considered as a single system. For AEMA and DMAEMA containing hydrogels, this system comprises the ionophores ($–NH_3^+$) and ($–NH^+-(CH_3)_2$) which contribute fixed positive charges within the hydrogel and mobile co-ions H^+ and Na^+ that originate outside the hydrogel. The HEPES (4-(2-hydroxyethyl)-1-piperazineethanesulfonic acid) buffer, itself a zwitterionic organic molecule, contributes $-SO_3^-$, which along with OH^- in the bathing solution, contributes counter anions each with the capability to adsorb and diffuse into the hydrogel and be equilibrated with the inherent cationic charges within the hydrogel. The extent of ionization of the ionogenic moieties depends upon their pKa and is governed by the Henderson–Hasselbalch equation. The ion partitioning and the concentration of free ions is governed by Gibbs-Donnan

partitioning effect, which depicts the relation between the concentrations of the different ions in hydrogel (*h*) and in the surrounding solution (*s*) (Eq. 16).

$$a^h_{mco} = C^h_{mco}\gamma^h_{mco}; a^s_{mco} = C^s_{mco}\gamma^s_{mco}; a^h_{cou} = C^h_{cou}\gamma^h_{cou}; a^s_{cou} = C^s_{cou}\gamma^s_{cou} \quad (16)$$

Where, *a*, *C*, and γ are the activity, the molar concentration, and the activity coefficient, respectively, the subscripts *mco* and *cou* refer to mobile co-ions and counter anions, respectively, and the superscripts *h* and *s* refer to the hydrogel and the adjacent solution, respectively. When ionic solutions approach the dilute solution limit, $C^h_{mco} \ll C^h_{fix}$ holds true and the equation modifies to (Eq. 17)

$$C^h_{mco} = \frac{C^s_s}{C_{fix}}\left(\frac{\gamma^s_{\pm}}{\gamma^h_{\pm}}\right)^2 \quad (17)$$

The hydrogel resistance is the reciprocal of conductance[168]. The resistance, R, of a highly hydrated hydrogel may be expressed as its dimensionalized value, resistivity, ρ, a material property or as a reciprocal of its conductance, S, and its dimensionalized value, conductivity, σ (Eq. 18)

$$R = \frac{1}{S} = \rho\frac{l}{A} = \text{and } S = \sigma\frac{A}{l} \quad (18)$$

For conductive polyelectrolytes like hydrogels, the total conductance, S_{total}, and the total conductivity, σ_{total}, are the sum of the contributing conductances and conductivities of the constituent ions within the material. Thus, (Eq. 19)

$$S_{total} = S_+ + S_- \text{ and } \sigma_{total} = \sigma_+ + \sigma_- \quad (19)$$

Where subscripts + and – refer to cations and anions respectively. The equivalent conductivity can be expressed as (Eq. 20)

$$\Lambda_{eq} = \lambda_+ + \lambda_- \quad (20)$$

Where, λ_+ and λ_-, are the equivalent conductivities of the contributing cations and anions, respectively.

The flux generated due to application of an electric field gradient to the hydrogel can be written as (Eq. 21)

$$J_c = \sum_i \nu_i z_i \mu_i [C] \text{ e } N_A \quad (21)$$

Here, J_c is the flux of charges through the hydrogel medium, *i* refers to the i^{th} charge carrier, z_+ and z_- refer to the charges on or valence of the dissociated ions, ν_+ and ν_-refer to the stoichiometric coefficients of the cation and anion, respectively, μ_i is its ion mobility, e is the charge on an electron (1.602×10^{-19} C) and NA is Avogadro's number (6.023×10^{23}). The product, e* NA = 96,485 C or Faraday's constant[169].

The minor mol% inclusion of the ionogenic AEMA (1° amine) and DMAEMA (3° amine) moieties, affects the Gibbs-Donnan partitioning and hence the equilibrated internal concentration of free ions. Thus, the membrane impedance of the hydrogel at pH 7.4, captured using EIS technique, was governed by the ionic concentrations and mobility of ions. Membrane resistances were calculated based on the forgoing and were shown to be in remarkably good agreement with measured values. The hydration of hydrogel was determined and reported under biotechnically relevant conditions and not in DI water. Since the protein adsorption and impedimetric pH-responses were all measured under 25mM HEPES condition and we sort to investigate the relationship between water content and distribution on these biotechnical properties, all hydrations were measured in 25 mM HEPES.

The manuscript focusses on the influence of composition of poly(HEMA)-based hydrogels on the key biotechnical properties and mentions the pH response of the hydrogels as it directly reports on observations of impedance measurements as a function of pH (indirect

measurements). The pH critical characterization and responses for pH (direct measurements) and temperature (LCST and UCST) are the topic of an extensive and detailed study that will shortly be reported from our lab.

2.4.5 Protein Adsorption

Adsorption data from FITC-labeled albumin were fitted to a Langmuir adsorption isotherm model using the solver fit within MS Excel. Parameters like maximum surface coverage, Q_{max}, and the equilibrium constant, K_{eq}, were extracted. **Figure 18** shows the Langmuir surface coverage, Q_{max}, of FITC-labeled albumin adsorption onto the poly(HEMA)-based hydrogels containing 4 mol% HEMA, 4 mol% AEMA, 4 mol% DMAEMA and 2 mol% AEMA + 2 mol% DMAEMA. The hydrogel formulation with 4 mol% DMAEMA showed the highest protein coverage while the hydrogel formulations with 4 mol% HEMA and 4 mol% AEMA showed similar but lower protein coverage. Sticky proteins such as albumin, readily unfold exposing their hidden, hydrophobic core to hydrophobic domains on surfaces as they spread [170, 171]. The simultaneous inclusion of AEMA and DMAEMA, each at 2 mol%, could be expected to behave, to a first approximation and in accord with the rule of mixtures, as a balance between the influences of the two monomer. However, this formulation behaved unlike any other producing the lowest protein adsorption.

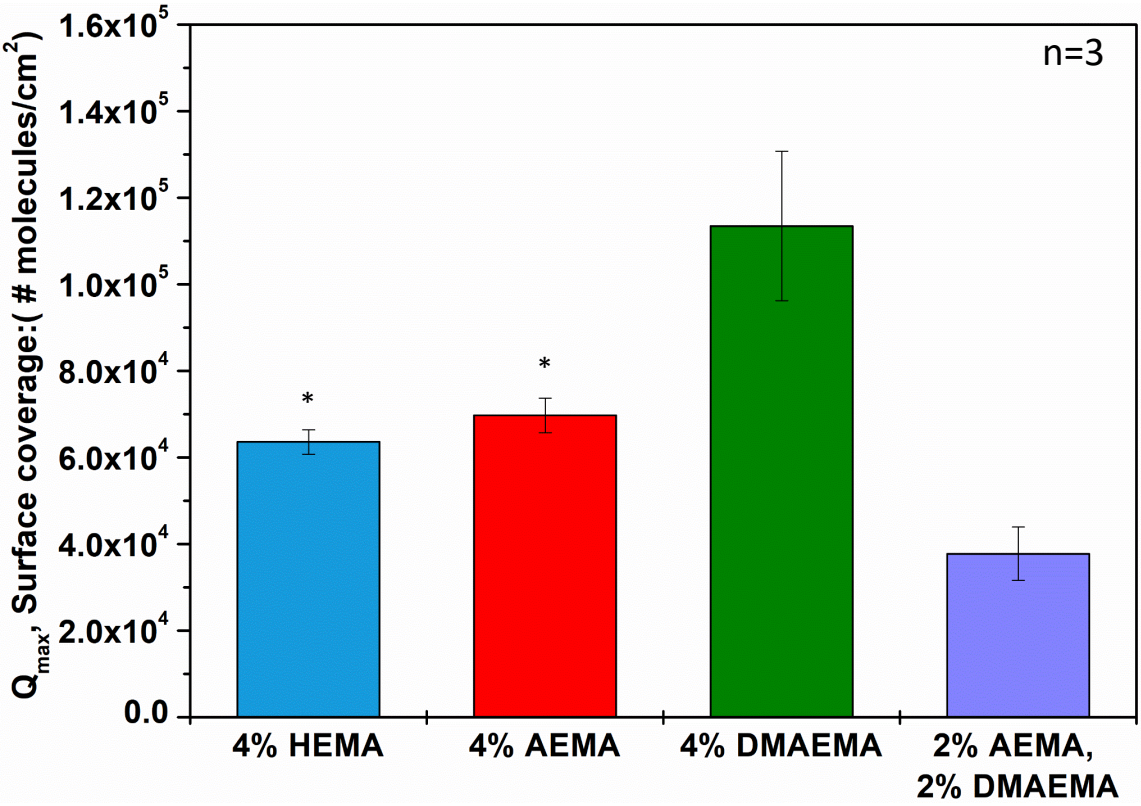

Figure 18. Langmuir surface coverage, Qmax, of FITC-labeled albumin adsorption onto poly(HEMA)-based hydrogels containing 4 mol% HEMA (blue), 4 mol% AEMA (red), 4 mol% DMAEMA (green) and 2 mol% AEMA + 2 mol% DMAEMA (purple).

Proteins adsorb quite differently onto hydrophobic and hydrophilic surfaces [172]. On hydrophilic surfaces, a hydration corona prevents globular proteins from readily unfolding to become adsorbed. The reduction in bound water that accompanies the inclusion of 4 mol% DMAEMA reduces this hydration corona is reflected in higher protein adsorption. As a corollary, the inclusion of 4 mol% AEMA, which possesses a similar hydrophobicity index as HEMA, results in similar bound water and similar protein adsorption. The distribution of free and bound water, influenced by hydrophobicity/hydrophilicity, in turn influences the amount of protein adsorption on the surface. As proteins do not adsorb onto bound water rich surfaces, the AEMA/DMAEMA subsystem shows the least protein adsorption.

2.4.6 Correlations between water content, distribution and the physicochemical properties

Correlations among the water content, water distribution and the physicochemical and biological properties of these hydrogels were explored using multivariate methods in JMP software. **Table 6** summarizes the results of the correlation analysis.

Table 6. Correlations between water content, water distribution and the physicochemical biotechnical properties of poly(HEMA)-based hydrogels.

	Modulus (kPa)	Impedance (Ω) at RT	Impedance (Ω) at 37 ˚C, 5% CO_2	Q_{max} (#molecules/cm^2)
Bound water	-0.92	-0.87	-0.85	-0.67
Free water	0.61	0.52	0.59	0.22
Total Hydration	-0.98	-0.96	-0.90	-0.85

As expected, there was a strong inverse correlation between elastic modulus, membrane resistance at room and physiological temperature, the maximum protein surface coverage and total hydration. That is, for similarly cross-linked poly(HEMA)-based hydrogels experience small changes in monomer feedstock composition, as total water content goes up the hydrogel becomes softer, the membrane becomes more conductive, and sticky proteins are disposed to lowered adsorption coverage. However, free water showed a direct correlation with all the physicochemical and biological properties. It was the bound water, however, that showed the inverse correlation, similar to total hydration. Thus, it was seen that the high inverse correlation associated with the total hydration was governed by the bound water contribution. It is the bound water, which as a controlling factor, is indicative of the change in modulus, membrane resistance and protein surface coverage, which in turn were influenced by minor changes in the hydrogel composition.

*2.4.7 Hydrophobicity indices for HEMA, AEMA and DMAEMA monomers**

Hydrophobicity indices for poly(HEMA)-based hydrogels: HEMA, AEMA and DMAEMA calculated from two different methods: 1) Partition coefficients and 2) Kyte-Doolittle scale are depicted.

2.4.7.1 Partition coefficients for HEMA, AEMA and DMAEMA

Table 7 mentions the hydrophobicity indices for HEMA, AEMA and DMAEMA monomers based on the partition coefficients of monomers[157] derived from their functional group contributions.

Table 7. Partition coefficients of monomers based on their functional group contribution.

Monomers	*Functional group*	*Partition coefficients (log P)*
HEMA (CH_3OH)	*-OH*	*-0.74*
AEMA (CH_3NH_2)	*-NH_2*	*-0.57*
DMAEMA ($N(CH_3)_3$	*-$N(CH_3)_2$*	*0.16*

2.4.7.2 Hydrophobicity indices of the monomers using Kyte-Doolittle scale (amino acids)

Table 8 mentions the hydrophobicity indices for HEMA, AEMA and DMAEMA monomers based on the Kyte-Doolittle scale[158] derived from their functional group contribution.

*Reprinted with permission from "Dataset on hydrophobicity indices and differential scanning calorimetry thermograms for poly (HEMA)-based hydrogels" by **Bhat, A.,** Smith, B., Dinu, C. Z., & Guiseppi-Elie, A., 2019. *Data in Brief, 103891*. Copyright [2019] by Elsevier

Table 8. Determining hydrophobicity indices of monomer as per amino acids.

Monomers	*Functional group*	*Partition coefficient (log P)*	*Amino acid*	*Hydrophobicity index*
HEMA	*-OH*	*-0.74*	*Ser*	*-0.8*
AEMA	*-NH_2*	*-0.57*	*Asn and Lys*	*-3.5 and -3.9*
DMAEMA	*-$N(CH_3)_2$*	*0.16*	*Leu and Arg*	*3.8 and -4.5*

2.4.8 Differential Scanning Calorimetry (DSC) thermograms for 4 mol% HEMA, 4 mol% AEMA, 4 mol% DMAEMA and 2 mol% AEMA/ 2 mol% DMAEMA

Figures 19-22 depict the DSC thermograms for poly(HEMA)-based hydrogel polymers synthesized to contain 4 mol% HEMA, 4 mol% AEMA, 4 mol% DMAEMA, and 2 mol% AEMA plus 2 mol% DMAEMA. **Table 9** shows the glass transition temperature, Tg, for all four poly(HEMA)-based hydrogel formulations.

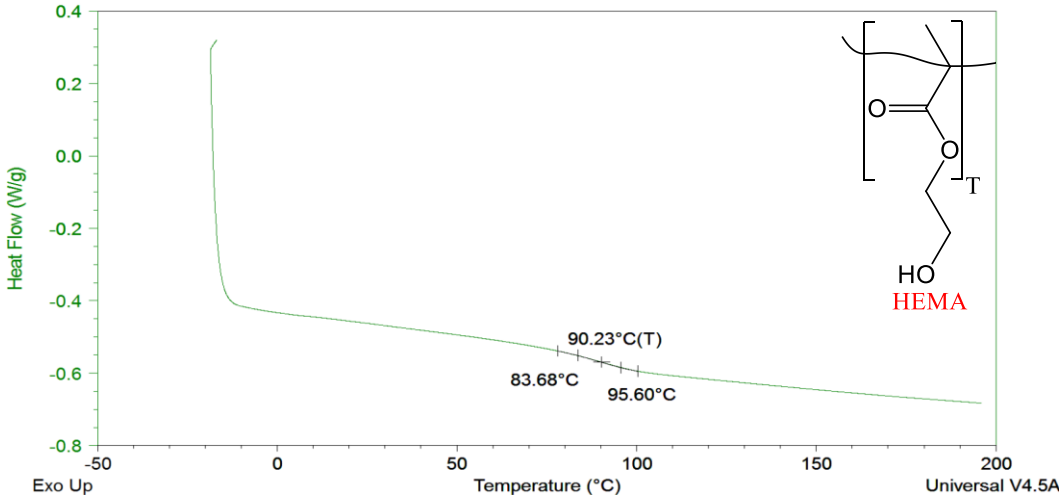

Figure 19. DSC thermogram for poly(HEMA)-based hydrogel containing 4 mol% HEMA

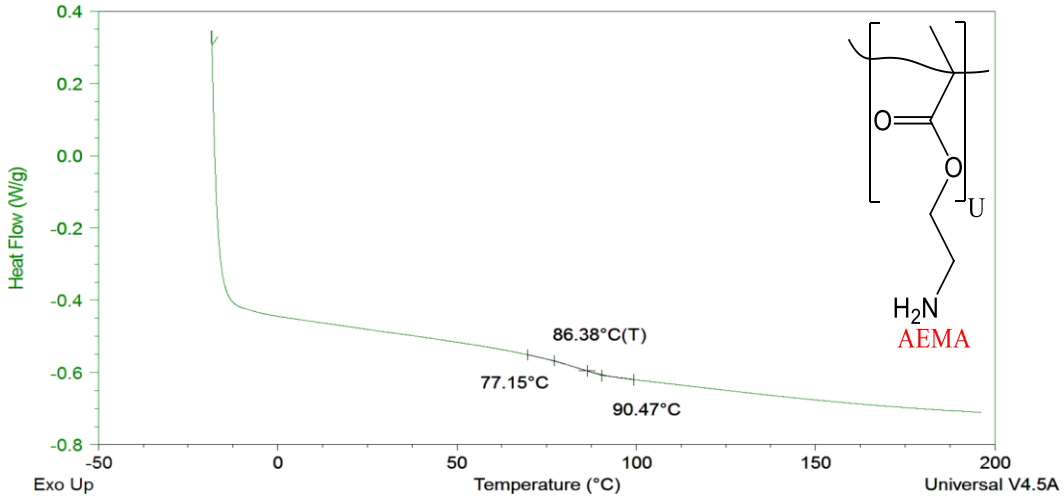

Figure 20. DSC thermogram for poly(HEMA)-based hydrogel containing 4 mol% AEMA

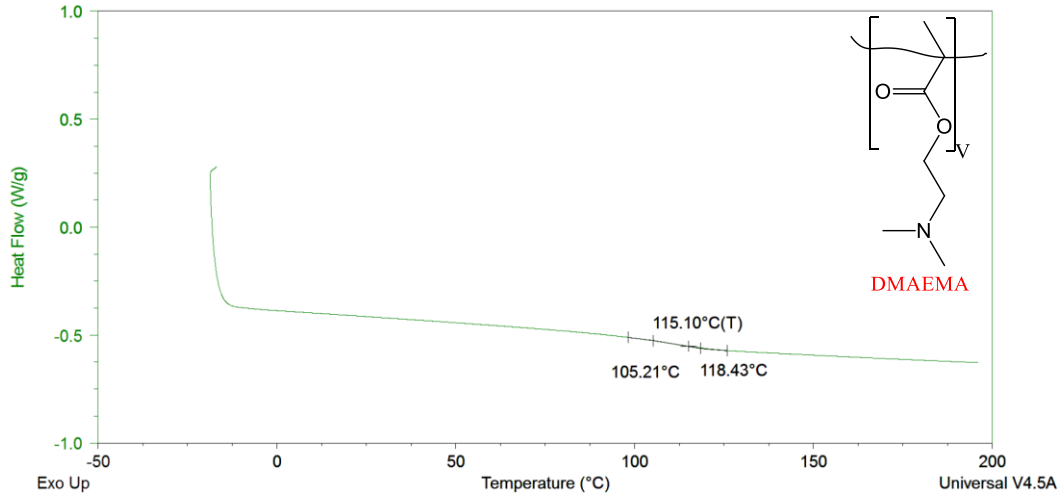

Figure 21. DSC thermogram for poly(HEMA)-based hydrogel containing 4 mol% DMAEMA

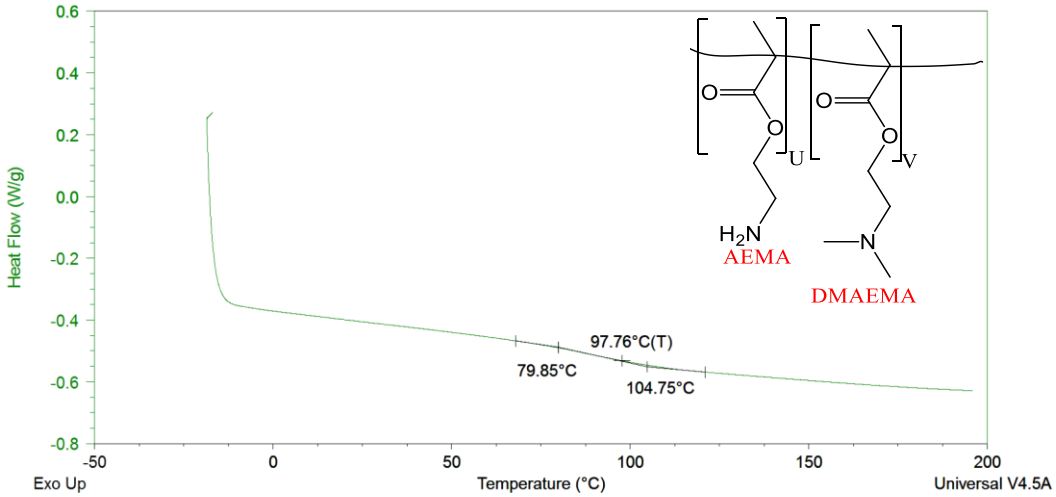

Figure 22. DSC thermogram for poly(HEMA)-based hydrogel containing 2 mol% AEMA+ 2 mol% DMAEMA

Table 9. Glass transition temperature, Tg, for all four poly(HEMA)-based hydrogel formulations containing 4 mol% HEMA, 4 mol% AEMA, 4 mol% DMAEMA, and 2 mol% AEMA + 2 mol% DMAEMA [2].

Property	4 mol% HEMA	4 mol% AEMA	4 mol% DMAEMA	2 mol% AEMA 2 mol% DMAEMA
T_g(°C)	93.2 ± 2.9	86.3 ± 1.3	114.2 ± 0.7	96.3 ± 0.4

2.5 Conclusions

Minor changes, nominally 4 mol% (4.4 mol%), in monomer composition of a poly(HEMA)-based hydrogel, while having very little influence on total hydration was shown to have profound impact on the distribution of water within the hydrogel, the elastic modulus, the membrane electrical resistance, and critical biological properties such as protein adsorption. The

changes in the physicochemical and biological properties were shown to strongly correlate with total hydration and that this correlation was best associated with the bound water content. The more hydrophilic monomer, AEMA, maintained hydration and water distribution similar to the reference HEMA hydrogel. However, the more hydrophobic monomer, DMAEMA, caused a minor decrease in the total hydration and a major shift in water distribution compared to the HEMA hydrogel. The inclusion of both AEMA and DMAEMA resulted in deviation from expected behavior. The equimolar mixtures of AEMA and DMAEMA showed total water content that was essentially unchanged but had water distribution that was more similar to the DMAEMA-only than to the AEMA-only hydrogel. Hence, the chemical structure of the hydrogels relates to its physico-chemical properties. For example, relative to the control HEMA hydrogel, hydrophilic monomer AEMA showed higher membrane resistance and similar surface coverage for protein adsorption. On the other hand, the hydrophobic monomer DMAEMA showed an enhanced membrane resistance and a higher surface coverage for protein adsorption. The AEMA/DMAEMA deviated from its normal expected midway behavior between the hydrophilic/hydrophobic subsystems and showed a lower membrane resistance and surface coverage for protein adsorption. This system can be used to make biosensors like a pH sensor to yield membrane resistances across a range of pH values indicating pH sensitivity.

CHAPTER III

TOWARDS IMPEDIMETRIC MEASUREMENT OF ACIDOSIS WITH A PH-RESPONSIVE HYDROGEL SENSOR*

3.1 Introduction

Next generation smart materials must sense targeted changes in their environment, respond predictably with materials-property based changes decisively linked to the environmental stimuli and be conditioned by that change to respond differently to new stimuli, that is, the material must "learn"[173]. There is continued growing interest in the use of hydrogels as responsive smart materials [174, 175]. This interest is fueled by the relative ease with which hydrogels may be molecularly engineered through variation in molecular composition, network density variation, and internal architecture control. Possessing broad applicability and biocompatibility [176] in various biomedical applications such as drug delivery [177] and biosensing [178], hydrogels are cross-linked polymeric networks of highly hydratable monomer that results in soft materials that imbibe large amounts of water. The hydration ensues due to solvation of the individual monomeric repeat units that seek to dissolve but are constrained by the covalent bonds that impose a retractive force on the polymeric network. At equilibrium, the water entrained by hydrogels can be rationalized as being distributed amongst freezable free water (W_{ff}), freezable bound water (w_{fb}), and non-freezable bound water (W_{nfb}) [74] [179]. Moreover, this distribution has been shown to be readily influenced by small changes in composition [75] and to govern key biotechnical properties [180] that are most strongly

*Reprinted with permission from "Towards Impedimetric Measurement of Acidosis with a pH-Responsive Hydrogel Sensor" by **Bhat, A.,** Amanor-Boadu J.M., & Guiseppi-Elie, A., 2020. *ACS Sensors, 5:500-9.* Copyright [2020] by American Chemical Society

correlated with the ratio of total freezable to non-freezable water [181]. The hydrogels which respond to a change in stimulus are called stimuli-responsive hydrogels[67]. These hydrogels swell and de-swell in response to external stimuli such as temperature, light, chemical reactions and pH [182]. Such swelling and de-swelling is the result of changes in the water content of the hydrogel linked to a hierarchy of chemical influences to changes in its three-dimensional network structure [179] and mesh size [183].

Hydrogels that are pH-responsive belong to a sub-class of stimuli-responsive hydrogels that may be neutral or ionogenic/protic as shown in **Figure 23**. Neutral hydrogels possess no ionizable groups in their molecular or repeat unit structure and when incubated in an external media of a particular pH, H_3O^+, OH^- and supporting ions partition into the hydrogel according to the Gibbs–Donnan effect [71]. Ionogenic hydrogels possess ionizable pendant groups in their structure which can be cationic or anionic and may be protic. These respond to a change in pH by protonating or deprotonating their ionizable groups [69]. This is accompanied by swelling and deswelling kinetics of the hydrogel [184]. The presence of the solvated ions within the hydrogel makes it an ionically conductive polyelectrolyte network. The conductivity of the hydrogel due to the ionic electromigration can be measured by probing the hydrogel with a small sinusoidal voltage using Electrochemical Impedance Spectroscopy(EIS) techniques [71].

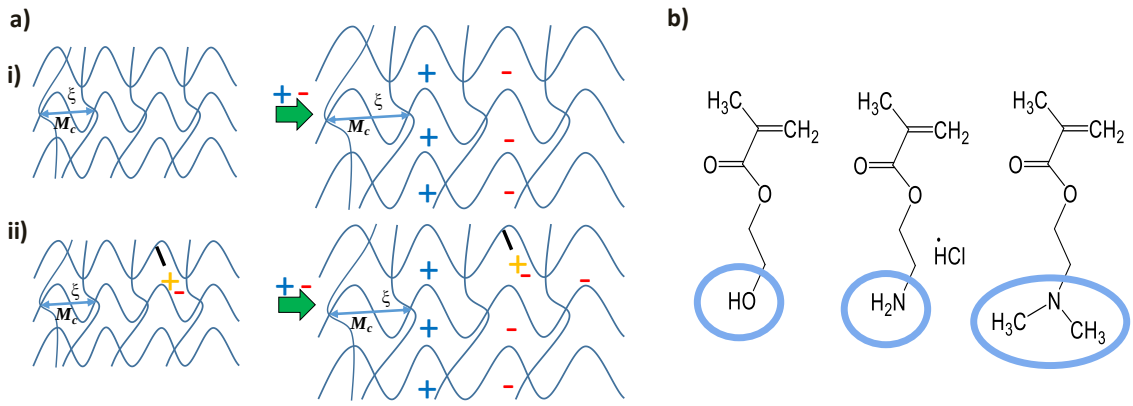

Figure 23. General types of pH-responsive hydrogels a) i) Neutral ii) Ionogenic and b) the chemical structures of hydrogel monomer constituents showing the non-ionogenic –OH of HEMA and the ionogenic moieties of AEMA and DMAEMA.

Different types of synthetic pH-responsive hydrogels have been reported in the literature [185-187]. Examples include hydrogels incorporating ionogenic monomer such as *N*,*N*-dimethylaminoethyl methacrylate (DMAEMA), acrylic acid (AA), methacrylic acid (MAA). pH-responsive hydrogels have also been fashioned from poly(acrylamide) (PAA), poly(methacrylic acid) (PMAA) with poly(ethylene glycol) (PEG), poly(HEMA), and polymers with phosphoric acid derivatives [186, 188-191]. Sheppard *et al.* have reported pH-responsive DMAEMA sensors showing highest pH-sensitivity between pH 7-8 corresponding to the pKa of DMAEMA [192]. Deirram *et al.* have reported the use of poly(2-(diisopropylamino)ethyl methacrylate) (PDPAEMA) for drug release at pH 7.4 [193]. pH-sensitivity in terms of equilibrium water content of poly(HEMA) and poly(acrylamide) hydrogels have been detailed by Rapado *et al.* [194]. Siegel *et al.* have demonstrated a system based on swelling of methyl methacrylate (MMA) and N,N-di- methylaminoethyl methacrylate (DMEMA) hydrogels for pH-sensitivity [195]. Hoffmann *et al.* have shown the pH-sensitivity for N-isopropyl acrylamide (NIPAAm) [196]. Guiseppi-Elie et al have studied DMAEMA containing copolymers of HEMA and 3-trimethoxysilylpropyl methacrylate(PMA) [197] as pH-responsive and glucose oxidase hosting

hydrogels for glucose responsive release of insulin in an all synthetic artificial pancreas [126]. Walker *et al.* showed changes in hydrogel properties arising from high salt concentrations that alter the activity of water, causing local charge shielding, and changes to inter- and intra-chain hydrogen bonding (virtual crosslinks) [198]. Along with the mechanical properties influenced by water distribution, electrical conductivity of the hydrogels, and the correlations between these two factors were studied for their application in using hydrogel-based sensors for biomedical applications [199]. The electrical resistance of a hydrogel membrane can be extracted from equivalent circuit modeling of EIS data. For a simple Randles equivalent circuit, the membrane resistance, R_M, and the parallel combination of charge transfer resistance, R_{CT}, and the double layer capacitance at the electrode-hydrogel interface, C_{DL},[200] , the mathematical representation of the system is as per Eq. 10, Eq.11, and Eq. 12. [201] [78]

Acidosis is a condition pursuant to tissue hypoxia and a consequence of anaerobic glucose metabolism wherein the pH of blood and interstitial fluid falls below 7.35 [13]. Monitoring the pH associated with acidosis is important in stabilizing the hemorrhaging patient [202]. Hence, a sensor is required to monitor the small fluctuations in pH in the pathophysiological range of 7.35-7.45 with high sensitivity. The measurement of membrane resistance of a pH-responsive hydrogel via EIS and equivalent circuit analysis represents an option to achieve this objective. Key considerations in performance are the device sensitivity [$d(R_M)/d(pH)$] and its stability.

This paper [203]investigates the role of hydrogel composition and its effects on hydration and conductance in search of a highly sensitive and robust hydrogel for impedimetric pH sensing in the pathophysiological range associated with the hemorrhaging trauma patient. The material composition of the stimuli-responsive hydrogel can be molecularly engineered[204] for

differential ionic distribution around the pK_a of the ionogenic group thereby affecting its water content, water distribution and impedance. This paper employed two methods: i) a parallel plate method that employed nano-platinum enobled stainless steel mesh electrodes [79], and ii) a microfabricated interdigitated pair of coplanar gold electrodes [205]. Using the parallel plate method, four hydrogels were investigated. The base system of poly(2-hydroxyethyl methacrylate) [poly(HEMA)] and alternate molecular compositions altered by introducing 4.4 mol% of hydrophilic and hydrophobic pendant groups; 2-aminoethyl methacrylate (AEMA, pKa=8.46)[140] and *N*-(2-(dimethylamino) ethyl)-methacrylate (DMAEMA, pKa=7.84)[206], respectively. The effects of a hydrophilic/hydrophobic mixture (AEMA/DMAEMA) 2.2 Mol%/2.2 Mol% was also investigated. The pH responsiveness of each composition was measured by EIS over the range pH 4-10 and specifically investigated over the pH range 7.35-7.45. Correlation by ANOVA was used to identify the water state that was best correlated with the impedance of the hydrogel. Additionally, Taguchi mixed-level fractional factorial design was used to establish a robust system devoid of influence of noise [207] [208]. Optimization was accomplished using the Response Surface Method (RSM) optimizer. RSM optimizer uses a quadratic fit modeling to identify within a design space the location of a point where the maximum or the minimum value of the response lies [209].

3.2 Materials and Methods

Hydrogels were synthesized from monomers 2-hydroxyethyl methacrylate (HEMA), cross-linker tetra(ethylene glycol) diacrylate (TEGDA), poly(ethylene glycol)(360)methacrylate (PEG(360)MA), hydrophilic support monomer N-[tris(hydroxymethyl)methyl]acrylamide (HMMA, 93%), biocompatible viscosity modifier polyvinylpyrrolidone (pNVP, MW ~1,300,000), photo-initiator 2,2-dimethoxy-2-phenylacetophenone (DMPA, 99+%) procured

from Sigma Aldrich Co. (St. Louis, MO, USA). To remove the polymerization inhibitors, hydroquinone and monomethyl ether hydroquinone, methacrylate and diacrylate reagents were passed through an inhibitor removal column (306312, Sigma-Aldrich Co., St. Louis, MO). Deionized water was obtained using a Milli-Q® plus water system (Millipore Inc., Bedford, MA). The 4-(2-hydroxyethyl)-1-piperazineethanesulfonic acid sodium salt (HEPES) buffer of 25 mM was pH adjusted to the nominal values of 5, 6, 7, 8, 9, 10 by dropwise addition of 0.1 M NaOH and pH adjusted to 4 with 0.1 M HCl. Dulbecco's Modified Eagle Medium (DMEM, high glucose with 4500 mg/L glucose) at pH 8.14 was pH adjusted to 7.35, 7.40 and 7.45 by dropwise addition of 0.1 M HCl. DMEM is a pseudo-body fluid that acts as a physiologic mimicking fluid [210] when used under physiologic conditions (T = 37 ºC and 5% CO_2). DMEM contains the full suite of physiologically relevant inorganic salts of calcium, potassium, sodium, and magnesium, amino acids, vitamins and other components including glucose (4500 mg/L) and pyruvic acid (110 mg/L). Acryloyl-PEG (3500)-NHS and 3-aminopropyltriethoxysilane (ϒ-APS) were used for conjugation and surface modification for the attachment of hydrogel to chips. Octadecyltrichlorosilane (OTS) was used for creating hydrophobic glass slides. All materials were procured from Sigma Aldrich Co. (St. Louis, MO, USA) unless stated otherwise.

3.2.1 Hydrogel cocktail formulation and sample preparation

All monomers were handled in a UV-free laboratory with UV filtering sleeves (TG-T8TG-UV, Lightbulbsurplus.com) placed over the fluorescent light bulbs. The monomers were added as per their mol% compositions and mixed with ethylene glycol:water (1:1 v/v ratio) to form 20 volume% of the formulation. The reference hydrogel was synthesized from 84.2 mol% HEMA. Three ionogenic hydrogels were synthesized containing monomer substitutions of 4.4 mol% hydrophilic (AEMA), 4.4 mol% hydrophobic (DMAEMA) or 2.2 mol%/ 2.2 mol%

hydrophilic/ hydrophobic (AEMA/ DMAEMA) to create four hydrogel compositions. The AEMA containing hydrogel was also investigated at 1, 3 and 30 mol%. The mol% compositions are tabulated in **Table 10.** Degassed hydrogel cocktails were pipetted into the wells of non-adhesive, press-to-seal silicone isolators of diameter 4.5 mm and thickness 1.6 mm (JTR12R, Grace Biolabs, Bend, OR) placed on and then sandwiched between OTS-silanized glass microscope slides. Following UV-cross linking, slides were removed and hydrogels were retained in the isolators with the help of platinized Type 304 Stainless Steel mesh electrodes (5 mm x 1 mm) [79] attached on either sides of the isolator and secured with a plastic retaining clip. This was done to ensure that during hydration, the hydrogels were kept within the isolators. The hydration process involved sequential incubation for 1 h each in ethanol (99%) and 25 mM HEPES buffer (pH 7.40) mixtures in proportions of 100/0, 75/25, 50/50, 25/75 and 0/100 (mL/mL%). Following this, the hydrogels were placed inside an incubator (VWR 2310, Marshall Scientific, Hampton, NH) which was maintained at physiological conditions of 37 ºC and 5% CO_2 and equilibrated in pH-adjusted HEPES buffer at nominal pH values of 4, 5, 6, 7, 7.35, 7.40, 7.45, 8, 9, and 10. The samples were removed from the buffer and excess liquid was removed by gentle blowing with nitrogen gas prior to conducting EIS measurements within the incubator which also served as a Faraday cage.

Table 10. Monomer components with their mol% composition for the various poly(HEMA)-based hydrogels.

Polymer constituents	Mol% of monomer components						
	4-mol% HEMA	4-mol% AEMA	4-mol% DMAEMA	2-mol% AEMA 2-mol% DMAEMA	1-mol% AEMA	3-mol% AEMA	30-mol% AEMA
HEMA (Base monomer: hydrophilic)	79.8	79.8	79.8	79.8	83.2	81.2	54.2
TEGDA (Cross-linker)	3.3	3.3	3.3	3.3	3.3	3.3	3.3
PEGMA(360) (Confers biocompatibility)	5.8	5.8	5.8	5.8	5.8	5.8	5.8
HMMA (Support monomer: hydrophilic)	4.4	4.4	4.4	4.4	4.4	4.4	4.4
pNVP (Pre-polymer: Increases viscosity) (on the basis of repeat unit structure)	1.9	1.9	1.9	1.9	1.9	1.9	1.9
HEMA (Monomer: hydrophilic)	4.4	0	0	0	0	0	0
AEMA (Monomer: hydrophilic)	0	4.4	0	2.2	1	3	30
DMAEMA (Monomer: hydrophobic)	0	0	4.4	2.2	0	0	0
DMPA (Photoinitiator)	0.4	0.4	0.4	0.4	0.4	0.4	0.4

3.2.2 Electrochemical impedance spectroscopy (EIS)

EIS was conducted over the range 1 MHz - 10 mHz using 10 mVpp sine wave (5 points per decade) using a Versastat4 (Princeton Applied Research, AMETEK, Inc., Oak Ridge, TN). The data was modeled using Randles equivalent circuit R(QR) or R(QR)(QR) in ZSimpWin software version 3.60 (AMETEK, Inc., Oak Ridge, TN). Parameters like membrane resistance (R_M) of the hydrogel, charge transfer resistance (R_{CT}) and double layer capacitance (Q_{DL}) were extracted. R_M versus pH graphs was plotted to reveal the pH responsiveness of the hydrogel. All measurements were conducted with the hydrogel placed inside the incubator. Control experiment

included the impedance characterization of pH adjusted HEPES buffer over the pH values of 4, 5, 6, 7, 7.35, 7.40, 7.45, 8, 9, and 10.

3.2.3 Hydration characteristics of hydrogels

3.2.3.1 Hydration of hydrogels using gravimetric methods

Gravimetric methods were employed to determine the degree of hydration (DoH) of the hydrogels. Hydrogel discs were weighed after equilibrium hydration and upon complete dehydration. Hydrogels were stored in a -80 ºC freezer for a period of 12 hours and lyophilized under 0.01 mbarr at -50 ºC to yield the dehydrated weight. The hydrated and dehydrated hydrogel weights were recorded as W_h and W_d respectively. DoH was calculated as fractional percentage change in weights upon drying. W_w was termed as the total water content.

3.2.3.2 Differential scanning calorimetry (DSC)

Differential Scanning Calorimetry (Q2000, TA instruments, New Castle, DE) was used to determine the distribution amongst water states within the hydrated hydrogels [211]. About 5-10 mg of hydrated hydrogel was sealed into a hermetic pan (Tzero hermetic lid, 901684.901; Tzero pan, 901683.901) and equilibrated at -40 ºC and heated to 30 ºC at 10 ºC/min under purging nitrogen (50 mL/min). Using TA analysis software, the endothermic peak was integrated to reveal the enthalpic contribution ΔH_m, of hydrogels at 0°C [212]. The enthalpy of freezable and bound water was assumed to be same as that of the bulk water (ΔH_0 = 334 J/g)[213]. The freezable free water content and non-freezable bound water content was calculated using the equations (Eq. 8 and Eq. 9):

3.2.4 Design of experiments approach

3.2.4.1 Taguchi orthogonal arrays

Taguchi orthogonal arrays, which is a form of a design of experiments (DoE) approach, was used to find the optimal mol% composition for AEMA, while making a robust system by minimizing the effect of control factors and its fluctuations on the targeted output, sensitivity [214]. **Figure 24** shows the concept of the Taguchi design of experiments construct. The internal factor, AEMA mol%, was considered at 3 levels (1, 4.4 and 30 mol%), external factors were frequency, temperature and pH. Frequency was considered at 2 levels, f_τ-22.37 and f_τ+22.37 mHz, where f_τ is the frequency corresponding to the characteristic time constant of the hydrogel, temperature was considered at 2 levels (36 and 38 ºC) and pH was considered to be a factor with two levels (7.35 and 7.45). The two frequency levels were established as the difference between the smallest and the largest characteristic frequencies (Z" (ω_{max}) = -1/[ωC_{DL}l) from the Nyquist plots among the various AEMA mol%. The output was considered to be sensitivity [d(R_M)/d(pH)]. Weibull++ software (HBM Prenscia, Southfield, MI) was used to construct the Taguchi matrix design. The analysis estimated 36 experiments to be performed to complete the construct. The data table was imported and Taguchi analysis was completed in statistical software (Minitab, Inc., State College, PA) to generate plots for signal-to-noise ratio (higher the better) and data means, from which the optimal parameters were determined. Similarly, optimal parameters for freezable water content and non-freezable bound water content were determined. For maximizing the response, larger the better signal-to-noise ratio is expressed as (Eq. 22):

$$\frac{S}{N} = -10log\sum\frac{\left(\frac{1}{Y^2}\right)}{n} \qquad (22)$$

where *Y* is the observed data and *n* is the number of observations [215].

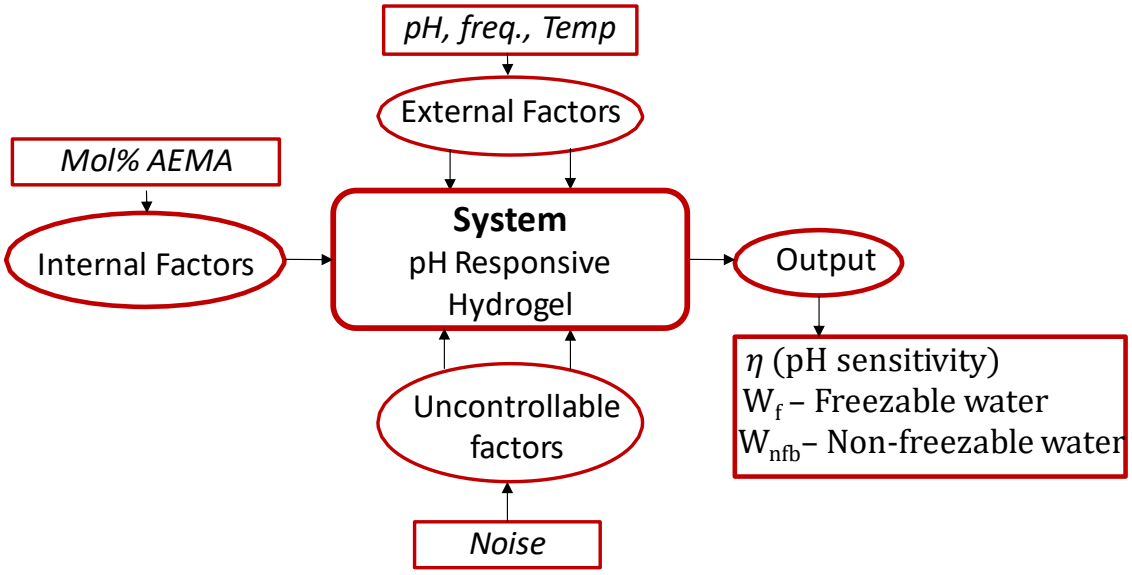

Figure 24. Concept of the Taguchi design of experiments construct for the generation of a robust hydrogel composition.

3.2.4.2 Response surface methodology (RSM) optimizer

An optimization approach using RSM was used to find the optimal sensitivities (membrane resistance, R_M versus pH) for AEMA, DMAEMA and AEMA/DMAEMA hydrogel subsystems. One factor RSM was performed using Design Expert software version 11 (Stat-Ease, Inc., Minneapolis, MN). A second-degree polynomial equation was fitted to identify the optimal sensitivity for each subsystem within design space of mol% from 0 to 30 mol%.

3.2.5 Hydrogel on IME chip

3.2.5.1 Surface inspection and cleaning

Microlithographically fabricated independently addressable microband electrodes and interdigitated microsensor electrodes (IAME-*co*-IME 2-1 Au) chips of dimensions 1.0 cm x 1.0 cm x 0.05 cm were supplied by ABTECH Scientific Inc. (Richmond, Virginia, USA). These chips were made from borosilicate glass substrates with patterns of gold electrodes and a windowed, insulating layer of silicon nitride (Si_3N_4) that revealed the region of interdigitation

but passivated the array buses. The chips were fabricated using the standard industry microlithography lift-off technique. Both the IAME and IME portion have finger dimensions of 1.0 mm x 2.0 μm with line separations of 1.0 μm each. The IME portion has a pattern of five interdigitated fingers. The electrodes on the IAME-*co*-IME chip were inspected using Stereo Microscope (Omano OM-113-1LP 10X / 30X, Roanoke, VA) to check for their integrity. The electrodes on the IAME-*co*-IME chip were cleaned by heating in trichloroethylene for 3 minutes, 1 min in acetone and 1 min in isopropyl alcohol to remove any organic residues and render the surface free from impurities, and subsequently treated with plasma cleaning (Basic Plasma Cleaner PDC-32G, Harrick Plasma, Ithaca, NY). Cathodic cleaning was performed in 0.1 M PBS buffer, pH=7.3 to remove adsorbed siloxane from the gold digits by employing three-electrode electrochemical cell set-up with reference electrode (Ag/AgCl, 3 M KCl) and sweeping the potential between 0 and -1.2 V using cyclic voltammetry at a scan rate of 100 mV/s for 40 cycles[216].

3.2.5.2 Surface chemistry for attachment of hydrogel on IAME-co-IME chip

A 0.01 M solution of ϒ-APS in toluene was freshly prepared, into which the IAME-*co*-IME chip was submerged under dark conditions. This allowed for physical adsorption of ϒ-APS molecules onto the -OH groups on the exposed glass substrate. The electrodes were sequentially rinsed in 100% toluene, 50:50% toluene: ethanol and 100% ethanol(v/v) for 1 min each. These were then heated using a vacuum oven (51221162, Precision, Swedesboro, NJ), at 40°C for 20 min and 110 °C for 10 min [217] to enforce covalent bonding between the ϒ-APS and -OH groups. Cooled slides having covalently-attached ϒ-APS groups were then immersed in deionized water for a period of 24 hours. This allowed for the extension of hydrophilic amine groups from the silica surface and for the hydrolysis of any unbonded ethoxy groups. The

electrodes were then immersed in a 0.1 mM solution of APN in HEPES buffer with the pH adjusted to 8.5. This enabled the ϒ-APS (primary amine group) to be covalently conjugated to the n-hydroxysuccinimide group of Acryloyl-PEG (3500)-NHS. The identified optimal mol% composition of the hydrogel was prepared, cast and cross-linked on the interdigitated IME portion as per the procedure described in the previous section.

3.2.5.3 Electrochemical impedance spectroscopy (EIS)

Electrochemical impedance spectroscopy (EIS) was performed to extract the membrane resistance of the optimally identified hydrogel composition cast onto the interdigitation region of the IME part of the IAME-*co*-IME chip. The hydrogel was placed in an incubator (VWR 2310, Marshall Scientific, Hampton, NH) which was maintained at 37 ºC and 5% CO_2 and equilibrated overnight in DMEM cell culture media pH adjusted to 7.35,7.40,7.45 from 8.14 using 0.1 M HCl. Excess DMEM was removed from the hydrogel and the Versastat-4 (Princeton Applied Research, AMETEK, Inc., Oak Ridge, TN) was employed for the characterization of the hydrogel over the frequency range 1 MHz-10 mHz using a 10 mVpp interrogation sine wave. The data was modeled using Randles equivalent circuit R(QR) in ZSimpWin software version 3.60 (AMETEK, Inc., Oak Ridge, TN). Parameters like membrane resistance (R_M) of the hydrogel, charge transfer resistance (R_{CT}) and double layer capacitance (Q_{DL}) were extracted. R_M versus pH graphs were plotted to reveal the pH responsiveness of the optimally identified mol% composition of the hydrogel.

3.2.6 Statistical Analysis

Results were presented as mean ± 95% confidence intervals (C.I.) with n = 3. Student's t-test with $p < 0.05$ was employed to determine the statistical significance of the results.

3.3 Results and Discussion

3.3.1 Electrical characterization of poly(HEMA)-based hydrogels in HEPES buffer

To establish reference parameters for the equivalent circuit modeling of pH-responsive hydrogels, EIS measurements employing the parallel plate method with silicone isolators were made in hydrogel-free, pH-adjusted HEPES buffer of pKa = 7.31 [218]. Parameters extracted from the Randles equivalent circuit [$R_S(Q_{DL}R_{CT})$] modeling of this hydrogel blank, particularly R_{CT} (7.4E-04±2.6E-05) Ω and Q_{DL}(5.4E+04 ±5.2E+04) $S.sec^n$, served as starting points for the parameterization of hydrogel equivalent circuit modeling. Hydrogel equivalent circuit modeling was accomplished with an [$R_S(Q_MR_M)(Q_{DL}R_{CT})$]. The first QR term reflected information about the resistive and capacitive behavior of the hydrogel membrane. The resistive behavior (R_{CT}) arose from charge transfer at the electrode-liquid interface, in this case from a platinized stainless steel electrode to the HEPES buffer and is likely dominated by hydrogen evaluation and oxygen reduction [201, 209]. The concentration of ions and their mobilities within the hydrogel can be related to total conductance [219], the reciprocal of which is the membrane resistance of the hydrogel. **Figure 25** shows the global trends of solution resistance (R_S, HEPES buffer only) and membrane resistance (R_M, various hydrogels) versus pH (4 – 10) in pH-adjusted HEPES buffer for the four poly(HEMA)-based hydrogels at physiological conditions (37 ºC, 5% CO_2) at 4.4 mol%. Across the range of pH explored (4.0 - 10.0) there was no significant change in the R_S, R_{CT} and Q_{DL} values of the HEPES blank system. This is shown as an essentially flat line ~ 40 Ω. When viewed closely, the observed change in the solution resistance, R_S, as a function of pH reflected the change in ion concentration associated with the protonation of HEPES below pH 6.0 and deprotonated above pH 9.0, with the pKa of the buffer being at 7.31 [218]. Hydrogels on the other hand had resistances that varied with pH, being low at low pH values, rising to ~$5x10^3$

Ω at pH=7 and low again at high pH values, reflective of the partition of H^+ and OH^- ions into the hydrogel.

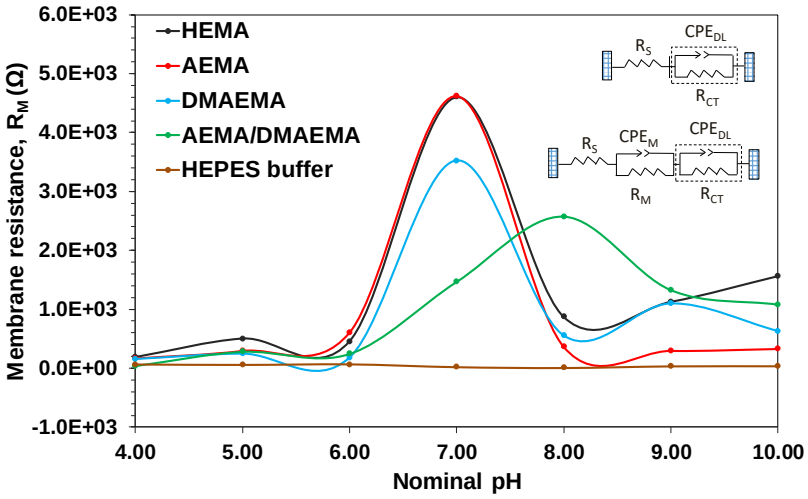

Figure 25. Plots of the solution resistance, R_S (Ω), of HEPES buffer blank and hydrogel membrane resistance, R_M (Ω), of various poly(HEMA)-based hydrogels of 4.4 mol% ionogenic monomer versus nominal pH at physiological conditions (HEPES buffer, T=37 °C, 5% CO_2).

Among the various poly-(HEMA)-based hydrogels tested, the AEMA containing hydrogels showed the possibility of a steep slope or high pH-sensitivity in the region from 7.0 to 8.0. From these results and from the fact that AEMA is a cationogenic moiety that promotes swelling of the hydrogel at lower pH [197, 220] [220], various mol% AEMA containing hydrogels were subsequently studied. **Figure 26** shows the global trends of solution resistance (R_S, HEPES buffer only) and membrane resistance (R_M, various hydrogels) versus pH (4 – 10) in pH-adjusted HEPES buffer for the five AEMA containing hydrogels (0, 1, 3, 4.4, 30 mol%) at physiological conditions (37 ºC, 5% CO_2). Across the range of pH explored (4.0 - 10.0) AEMA containing hydrogels of mol% that varied from 0-4.4 mol% had resistances that varied with pH, being low at low pH values, rising to ~$5x10^3$ Ω at pH=7 and low again at high pH values, reflective of the partition of H^+ and OH^- ions into the hydrogel. At 30 mol% AEMA, the

hydrogel behaved just like the hydrogel-free buffer, confirming that it was highly swollen with ion transport characteristics that were dominated by the buffer. Close inspection of the responses of the 0-4.4 mol% AEMA containing hydrogels in the region pH = 7.35 – 7.45 showed the 1 mol% AEMA hydrogel to present the steepest slope or highest sensitivity that was significantly different ($p<0.05$) relative to other compositions. Accordingly, the 1 mol% AEMA hydrogel was judged the most sensitive material for pH sensing in the desired pH region and investigated further.

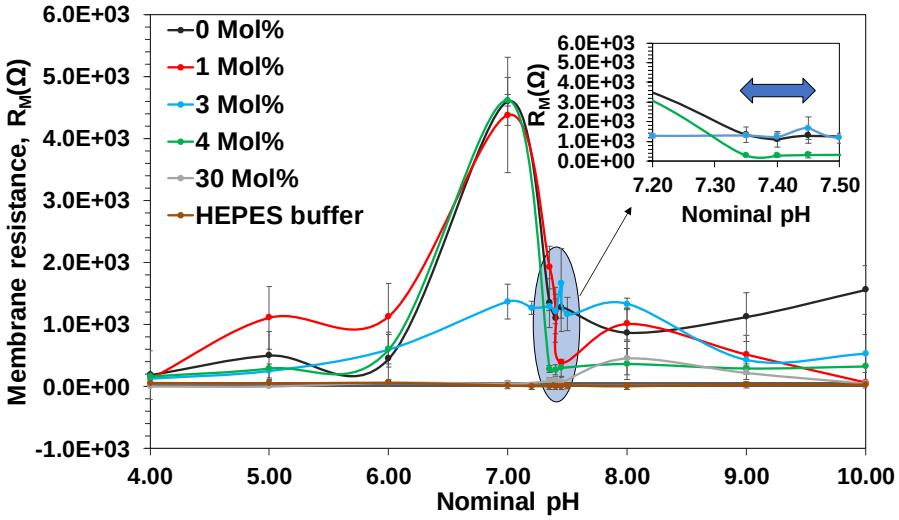

Figure 26. Plots of the solution resistance, R_S (Ω), of HEPES buffer blank and hydrogel membrane resistance, R_M (Ω), of various poly(HEMA)-based hydrogels of varying AEMA mol% monomer versus nominal pH at physiological conditions (HEPES buffer, T=37 °C, 5% CO_2).

3.3.2 Taguchi design and RSM optimization

Along with AEMA (above), electrical impedance characterization was performed over various mol% DMAEMA and AEMA/DMAEMA containing hydrogels in order to identify the significantly highest sensitivity corresponding to that molecular composition. The data from the

electrical impedance characterization was fed into the Taguchi robustness design construct and the RSM optimizer.

The aim was to produce a sensor that is less variable (more robust) in the face of variation over which the engineer has little or no control. For this approach, different factors (internal, external and outputs) with their levels were identified and the orthogonal array design was constructed, **Figure 24**. The robust design involves finding those factors which most affect the signal-to-noise ratio. For each control factor with its respective levels, the optimal or the highest signal-to-noise ratio was chosen. A maximization of the overall signal-to-noise ratio is selected to make the output devoid of any fluctuations in the control factors and thereby render the system robust [221]. Statistically, the effect of factor levels on the output responses can be depicted as (Eq. 23):

$$A_{L_n} = \left(\frac{1}{n_{L_n}} \sum_{i_{L_n}} Y_{i_{L_n}}\right) - \overline{Y} \qquad (23)$$

Where A_{L_n} is the effect of n^{th} factor level on the corresponding output, n_{L_n} depicts the number of outputs corresponding to the n^{th} level, and i_{L_n} refers to the rows corresponding to n^{th} level [222].

Two types of main effects plots are obtained from the Taguchi construct, higher signal-to-noise ratio and data mean. The higher signal-to-noise ratio plot identifies the robustness of the system using the setting of control factors which minimizes the effect of noise. This is accomplished by capturing the variation in the response under different conditions for noise. From the main effects plot for signal-to-noise ratio the composition was identified to be the most robust factor ($p<0.05$) and the factors' combinations for the most robust system was observed to be 1 mol% at pH 7.35, temperature 38 ºC, and frequency f_{τ}-22.37 mHz. For each combination of

the levels of external factors, the main effects plot for data means, such as combination of factors was identified to be 1 mol%, pH 7.35, temperature 36 ºC, and frequency = f_τ-22.37 mHz. In the combination of external factors; pH = 7.35, temperature = 38 °C and frequency = f_τ-22.37 mHz were the other robust factors to make the output of the system free of any fluctuation in the control factors. Thus, AEMA 1 mol% was the most robust hydrogel composition pH-responsive sensing in the desired pH region.

One-Factor RSM methodology[223] was used to find the optimal sensitivity corresponding to the mol% of all the systems. A general form of RSM can be written as (Eq. 24)[224].

$$y = \beta_0 + \sum_{i=1}^{k} \beta_i x_i \; + \; \sum_{i=1}^{k} \sum_{j \geq i}^{k} \beta_{ij} x_i x_j + \; \varepsilon \qquad (24)$$

Where y is the response surface, $x_i\, x_j$ are the independent variables, β is the intercept and ε is the error due to noise. From the RSM optimization, composition was identified to be a significant factor ($p<0.05$). For the AEMA system, optimal mol% was identified as 1 mol%, for DMAEMA it was observed to be 2 mol% and for AEMA/DMAEMA system it was seen to be 4 mol%. One factor RSM on AEMA, DMAEMA and AEMA/DMAEMA hydrogel compositions, performed by maximizing the sensitivity or slope, [$d(R_M)/d(pH)$], in the desired pH region 7.35-7.45, revealed optimal parameters. The predicted optimal sensitivity was 10,056 Ω/pH for the 2.2 mol% of DMAEMA hydrogel, and was 15,282 Ω/pH for the 4.4 mol% AEMA/DMAEMA hydrogel. However, both of these were less than the highest sensitivity obtained for AEMA 1 mol% hydrogel of 15,816 Ω/pH. Among all the mol% compositions identified experimentally or via prediction, the robust 1 mol% AEMA hydrogel was also the optimal composition for highest sensitivity.

3.3.3 Comparison of methods for impedimetric pH sensing under physiological mimetic conditions

The electrical characterization of sensitive, robust, optimal 1 mol% AEMA was performed using parallel plate mesh electrodes and microfabricated, co-planer interdigitated microsensor electrodes (IME) on a chip was determined in DMEM cell culture media at T=37 °C, 5% CO_2. DMEM cell culture media effectively simulates a physiological fluid, being comprised of a wide range of physiologically relevant monovalent and divalent inorganic ions but free of proteins. Both electrode formats allowed easy access of the test fluid as well as free expansion of the responsive hydrogel. The fundamental difference between these two configurations is the linear electric field and the fringing electric field[225], respectively. **Figure 27** shows the impedimetric response as the membrane resistance, R_M (Ω), versus pH in the pH region of interest for the pH-responsive hydrogel of 1 mol% AEMA. These dose-response curves [221] over the region of nominal pH = 7.0-8.0 is shown in **Figure 27a** and over the region of actual pH = 7.35-7.45 is shown in **Figure 27b**.

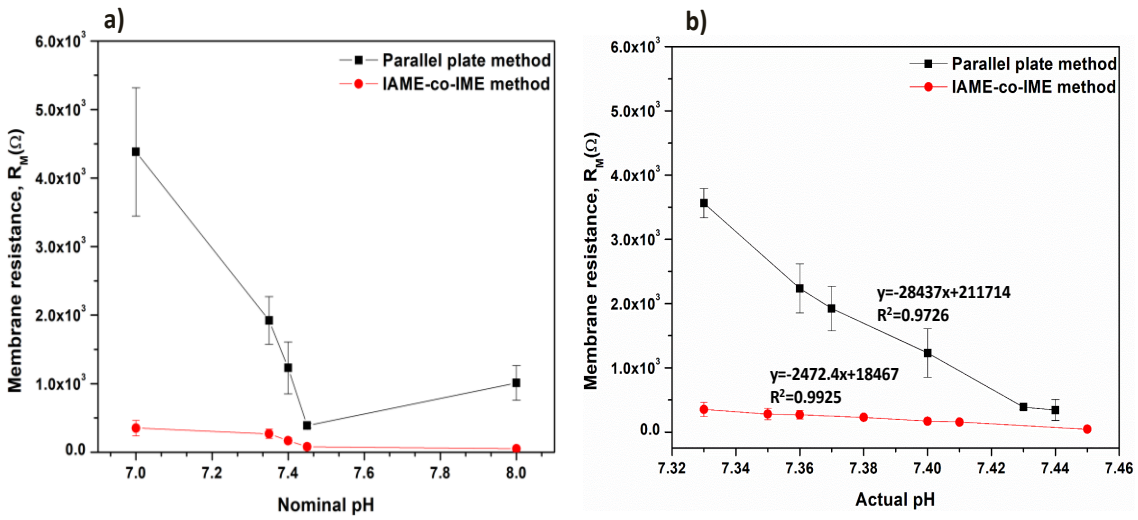

Figure 27. Plot of membrane resistance, R_M (Ω), versus pH in the pH region of interest for pH-responsive hydrogel sensors fashioned using the parallel plate method and co-planar, interdigitated microsensor electrode method in DMEM cell culture media at T=37 °C, 5% CO_2.

The parallel plate method and the impedimetric chip method yielded sensitivities in the desired pH range (7.35-7.45), [d(RM)/d(pH)], of is -28,437 Ω/pH and -2,472 Ω/pH, respectively. From the dose-response curves, additional sensor performance characteristics such as angle [$\theta = tan^{-1}(slope)$], detection limit [$DL = \frac{3S_{y/x}}{slope\ of\ regression\ line}$], dynamic range [$DR = 20log_{10}\left(\frac{Maximum\ Signal}{Noise}\right)$ dB, and chi square, a statistic for goodness of fit that shows how well the observed signal matches with the ideal expected signal [$\chi^2 = \sum\frac{(O_i-E_i)^2}{E_i}$] , were calculated and are summarized in **Table 11** [226, 227] [227] [221].

Table 11. Performance characteristics of the 1 mol% AEMA containing hydrogel sensor using the parallel plate method and the interdigitated microsensor electrode array method in DMEM cell culture media at T=37 °C, 5% CO_2 (for actual pH=7.35-7.45).

Parameters	IME method	Parallel plate method
Sensitivity (slope)	-2,472.4 Ω/pH	-28,437 Ω/pH
$\Theta=\tan^{-1}$(slope)	-89.976 º or -1.5703 rad	-89.997 º or -1.5707 rad
Detection limit	7.37 Ω	7.47 Ω
Dynamic range	11.06 dB	52.24 dB
Chi square	0.29	0.14

To be effective as a pH sensor, the buffer capacity of the responsive hydrogel should not itself perturb the pH of the test medium. Considering the size of the volume element (voxel) of hydrogel to be sampled, the Zaretsky convention[225] gives *d* x *w* x *h* where *d* is the length of the digits (1,000 µm), *w* is the width of the region of interdigitation [5 x λ = 5(2*a*+2*a'*) = 30 µm], where λ is the spatial periodicity, *a* is the digit width (2 µm) and *a'* is the space width (1 µm), and *h* is the depth of penetration of the fringing electric field into the hydrogel in the z-axis and is given as $h = \lambda/3 = 2$ µm. The total sampled volume is thus 60,000 μm^3 or 6.0 $x10^{-4}$ cm^3. This is a very small volume compared to the volume of tissue which the device must subtend[228]. Accordingly, the hydrogel layer is not expected to have sufficient buffering capacity to influence/alter the extra-hydrogel pH. Similarly, to be effective as a sensor, the pH response must be insensitive to the range of ions that may potentially partition into the hydrogel[229]. Hence, all dose response characterizations were done in DMEM under physiological mimetic conditions of T=37 °C, 5% CO_2. Interestingly, the impedimetric response does not arise from the rate of change of hydrogel swelling brought about by entry or egress of bathing ions but rather a

shift in steady state equilibrium arising from ion concentration and/or ion mobility. Acidosis reflects a gradual change in tissue pH and is expected to be in pseudo-equilibrium with the hydrogel membrane. The estimated response time for hydrogel layers on the order of ~10 µm thick is on the order of min. The two media, HEPES and DMEM, behaved similarly as our interest was the change in resistance with pH and not the absolute resistance of each hydrogel. The reported parameter is thus the highest sensitivity and not absolute resistance of the hydrogel. Dulbecco's Modified Eagle Medium (DMEM, high glucose with 4500 mg/L glucose) at pH 8.14 was pH adjusted to 7.35, 7.40 and 7.45 by dropwise addition of 0.1 M HCl, has been used as the cell culture medium. The pH sensitivity using hydrogels placed in DMEM under physiologic conditions (T = 37 ºC and 5% CO_2) maintained using incubator VWR 2310, which mimics blood plasma (without plasma proteins) and interstitial fluid (without extracellular matrix proteins), is a suitable and appropriate parameter for demonstration.

3.3.4 Water content and the governing factor in pH response

The water content and distribution within the AEMA containing hydrogels 0, 1, 4.4 and 30 mol% AEMA was determined by gravimetry, confirmed by DSC and is summarized in **Figure 28a**. The degree of hydration is simplistically the sum of freezable water and non-freezable bound water. Hydrogels with 0, 1 and 4.4 mol% AEMA possess similar degrees of hydration (~40%) that was dominated by non-freezable bound water reflecting the strong hydrogen bonding between water and the abundant hydroxyl group of HEMA [180]. Increased abundance of AEMA (30 mol%) dramatically increased the degree of hydration [197], from ~40% to ~80%, and established an equitable balance between the freezable and non-freezable water, statistically similar ($p<0.05$). Interestingly, the non-freezable bound water remained

essentially the same regardless of hydrogel composition, it was the freezable water which increased with increasing AEMA content.

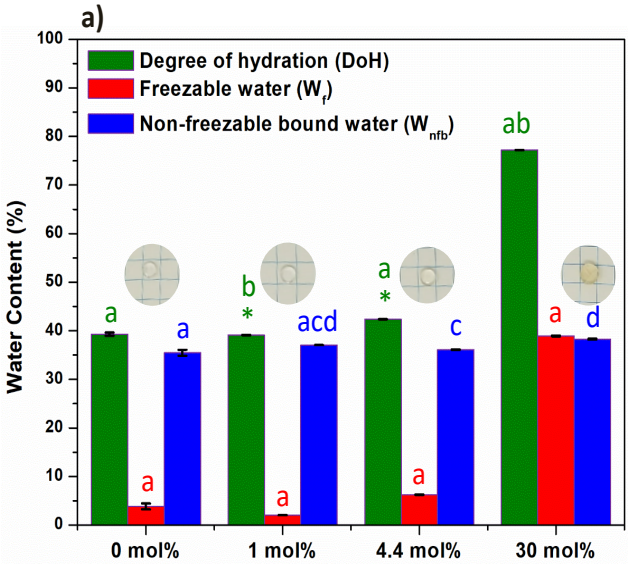

b)

	pH-Sensitivity
W_{nfb}	-0.82**
W_f	-0.70**
W_{nfb}/W_W	0.72**
W_f/W_W	-0.78**
W_f/W_{nfb}	-0.70*
DoH	-0.70*

Figure 28. (a) Degree of hydration (DoH), total freezable water, W_f, and non-freezable bound water, W_{nfb}, (%) for hydrogels synthesized with 0, 1, 4.4 and 30 mol% AEMA.

Correlations between pH-sensitivity and the type of water; total freezable water (W_f), total non-freezable bound water (W_{nfb}), degree of hydration (DoH), freezable water fraction (W_f/W_w), and non-freezable water fraction (W_{nfb}/W_w) was conducted using multivariate analysis in JMP software (SAS, Cary, NC). **Figure 28b** shows the calculated correlation coefficients. While there was the expected strong correlation of pH-sensitivity with total water content (-0.70), there was found a far stronger correlation between non-freezable bound water and hydrogel pH-sensitivity (-0.82). Non-freezable bound water is that portion of the imbibed water that interacts strongly with the polymer chains via hydrogen bonding and effectively shields the hydrated ions during transport. This implied that the non-freezable bound water may be the influential factor controlling the pH response of the hydrogel. It is the distribution of the water of hydration among freezable and non-freezable states that govern all the major biomedical

properties of hydrogels - not the total hydration [75, 230]. There was no significant difference in the total hydration of the 0 mol% and 1 mol% AEMA hydrogels. However, the addition of 1 mol% AEMA produced a significant difference ($p<0.01$) in the distribution of water states. Correlations between the states of water reveals that it is the non-freezable bound water which influences the total hydration and is the dominant factor governing the pH response of the hydrogels. Thus, hydrogel swelling was not what promotes the high pH sensitivity, but rather the most dramatic change in non-freezable water content. The possible mechanism involves increased responsiveness of the hydrogel with decreased non-freezing bound water due to more available, readily disreputable inter-chain hydrogen bonding interactions among moieties on the polymer backbone. Highly hydratable, high mol% AEMA hydrogels were less sensitive than the 1 mol% AEMA hydrogel which demonstrated the most dramatic change in non-freezable water content and was thus most sensitive to changes in external pH.

3.4. Conclusions

It was found that the molecular composition of a poly-(HEMA)-based hydrogel could be engineered for changes in hydration, distribution of water states and hence membrane resistance via impedance analysis. Minor compositional changes (<5mol%) manifest major changes in the biotechnical properties of the hydrogels through changes in the distribution of water states. A sensitive, robust and optimal poly-(HEMA)-based hydrogel for pathophysiological pH sensing in the region 7.35-7.45 was established with 1 mol% AEMA. The robustness and the optimization of this composition were confirmed using Taguchi Design of Experiments and the Response Surface Methodology. Water distribution within AEMA containing hydrogels was investigated and the type of water was correlated to the membrane resistance at physiological conditions to reveal non-freezable bound water as the most strongly inversely correlated parameter with the

membrane resistance and pH sensitivity. The highest sensitivity hydrogel was found to be that wherein the most dramatic change in non-freezable bound water occurs upon small changes in protonation-deprotonation of the ionogenic group. Since higher ionogenic compositions with higher hydration and higher ion concentration were not more sensitive, this suggests that it was changes to the ion mobility resulting from changes in non-freezable bound water that produced the highest pH sensitivity. A pH-sensitive hydrogel sensor chip to measure small fluctuations in pH associated tissue acidosis, intended for application in pH sensing during hemorrhage related trauma, has been demonstrated.

CHAPTER IV

ENGINEERING THE ABIO-BIO INTERFACE OF NEUROSTIMULATION ELECTRODES USING POLYPYRROLE AND BIOACTIVE HYDROGELS

4.1 Introduction

The biointerface is the contact region between an abio material and a material of biological origin [216]. Biointerface engineering refers to the purposeful manipulation of that interphasial region to achieve a desired technical objective. Chronically indwelling neurostimulation electrodes are needed to stimulate the vagus nerve of the chronically depressed [231], [232], [233] and to stimulate the spinal cord of paraplegics [234, 235],[236]. Typical electrodes are plagued by fibrous encapsulation [237] leading to increased interfacial impedance and an escalating power penalty [238]. Such fibrous encapsulation is the result of the inflammatory cascade [239] triggered by the foreign body response [240]. The goal of biointerface engineering in this context is to reduce interfacial impedance as well as mitigate the foreign body response [241]. In this paper, gold coated polyimide electrodes were sequentially coated with a layer of an electroconductive polypyrrole thin film for reduced interfacial impedance and a phosphoryl choline containing hydrogel layer to address the challenge of fibrous encapsulation at the ABIO-BIO or electrode-tissue interface.

It has previously been demonstrated that neurostimulation of the lumbar spinal cord in rats with spinal cord injuries can elicit motor movement of the legs [242]. While this treatment has produced promising results in several studies, its efficacy is hindered by increased impedance at the electrode-spinal cord interface. The foreign body response triggered by the presence of non-native material within the epidural space results in fibrous encapsulation of the electrodes in a layer of scar tissue [243]. Such encapsulation inhibits efficient charge transfer from electrode to

spinal cord, necessitating higher voltages in order to produce the same level of current stimulation. Therefore, modified electrodes with decreased impedance are critical to the success of neurostimulation treatments for spinal cord injury.

There are single biphasic constant current stimulators (0.25-0.3 ms per phase) [242] .The Precision® neurostimulator has a capability of multiple channels for constant current source. The Bion® microstimulator uses a single channel to provide currents between two electrodes [244]. In addition to constant current neurostimulators, there are constant voltage neurostimulators. For example, Synergy® neurostimulators [245] provide constant voltage over two sources. Restore® neurostimulators [246] provide constant voltage over a single source. Constant current neurostimulation has been reported by Silva et al. with current values from (0.4-2.0 mA) [247],[248],[249],[250]. Constant voltage values have been reported by Schade et al. from threshold of (3.6 ± 2.2) V to (5.3 ± 2.9) V [251], [252]. Neurostimulation electrodes are generally made from metallic materials[253] such as platinum[254], stainless steel[254], iridium, platinum-iridium, tungsten[255], gold, tantalum, tin, rhodium, and nichrome. Recently, porous graphene[256], reduced graphene oxide-gold oxide nanocomposite electrodes[257] have been used. The supporting but insulating materials[253] for these contacting electrodes include flexible polyimides, silicone sheets[258], and non-flexible glass and titanium nitride. Commonly used materials for modifying electrodes include polypyrrole (PPy) ,[259, 260], poly(3,4-ethylenedioxythiophene) (PEDOT) [261],[262],[263],[264] and polyaniline (PAn) [265],[266],[267].

Biocompatible electroconductive hydrogels provide a potential means of introducing electrodes into the body for long-term use[241] by inhibiting the foreign body response and reducing interfacial impedance. These hybrid polymers combine the biocompatible features of a

hydrogel with the electrochemical properties of inherently conductive electroactive polymers (CEPs) [268] such as polythiophene [269], polyaniline [270], and polypyrrole [129] [271]. Specifically, polypyrrole has been incorporated in a variety of biomedical applications, including nanofibrous guidance structures for nerve regeneration [272], photothermal chemotherapy treatment of breast cancer [273], and enzyme biosensors [274] for subcutaneous glucose monitoring [275], among others. Given its versatility, biocompatibility, and ease of synthesis, polypyrrole [276] has been identified as a conductive electroactive polymer of interest for use in neurostimulation [277].

This work [278]entails the fabrication and characterization of layered electroconductive polypyrrole [279] and a biocompatible hydrogel [197] intended to engineer the ABIO-BIO interface [142] as a means of decreasing interfacial impedance [280] and increasing biocompatibility [124]. The work identifies an optimum charge density of polypyrrole for modification of neurostimulation electrodes and explores the relationship between charge density, electroactive area, and charge transfer resistance. Electrodeposited polypyrrole thin films were synthesized from 0-100 mC/cm^2 and characterized by multiple scan rate cyclic voltammetry using the Fe(II)/Fe(III) system as a probe to reveal changes in the effective surface area, by electrical impedance spectroscopy to show changes in the charge transfer resistance, and by scanning electron microscopy to reveal changes in surface morphology pursuant to the growing conductive polymer film. By forming a copolymer of pyrrole with pyrrolyl butyric acid (PyBA) and by using EDC-NHS conjugation of the free acid with N-(2-aminoethyl) methacrylate (AEMA) and by using a UV-polymerizable dopant in the form of sulfopropyl methacrylate (SPMA), the hydrogel layer could be covalently bonded to the pyrrole layer.

Continual glucose and lactate monitoring is of importance in the measurement of physiological conditions such as hyperlactatemia (>2.0 mM) and hyper- and hypo-glycemia (>5.5 mM and <3.88 mM). Such monitoring can guide patient-specific therapeutic interventions in the management of conditions such as hemorrhaging trauma and diabetes (hyperglycemia). In this study, we have engineered amperometric-enzyme biotransducers for the monitoring of glucose and lactate wherein the enzymes lactate oxidase (LOx) and glucose oxidase (GOx) were hosted within hydrogel membranes consisting of 2-hydroxyethyl methacrylate (HEMA), and other monomers. Enhancements were pursued by forming supramolecular conjugates of the enzymes with Single-Walled Carbon Nanotubes (SWCNT) to promote direct electron transfer[281] and with polypyrrole:poly(styrenesulfonate) (PPy:PSS) nanoparticle inclusions to support redox mediation. Enhancements improved the electronic properties of the responsive hydrogels as characterized by amperometry. The surface modification was extended to test different electrode systems using Fe(II)/Fe(III) system as a probe to reveal changes in the effective surface area, suitable to build a sensitive LOx/GOx biotranduscer for amperometric sensing.

4.2. Materials and Methods

4.2.1 Materials

Chemicals and materials were purchased from Sigma Aldrich Co. (St. Louis, MO, USA) as described in earlier publications [75]. Briefly, the monomers 2-hydroxyethyl methacrylate (HEMA) (40.75 mol%), N-(2-hydroxypropyl) methacrylamide (HPMA) (40.75 mol%), poly(ethylene glycol)(360)methacrylate (PEG(360)MA) (5 mol%), N-[tris(hydroxymethyl) methyl]acrylamide (HMMA, 93%) (5 mol%), 2-Methacryloyloxyethyl phosphorylcholine

(MPC) (5 mol%), the cross-linker tetra(ethylene glycol) diacrylate (TEGDA, technical grade) (1.0 mol%), the biocompatible viscosity modifier polyvinylpyrrolidone (pNVP, MW ~1,300,000) (2.0 mol%, as monomer repeat unit) and the photo-initiator 2,2-dimethoxy-2-phenylacetophenone (DMPA, 99+%) (0.5 mol%) were prepared as a cocktail. Prior to mixing, methacrylate and diacrylate reagents were passed through an activated alumina column (306312, Sigma-Aldrich Co., St. Louis, MO) in order to remove the polymerization inhibitors hydroquinone and monomethyl ether hydroquinone. A Milli-Q® plus (Millipore Inc., Bedford, MA) ultrapure water system was used to prepare deionized water. The 4-(2-hydroxyethyl)-1-piperazineethanesulfonic acid sodium salt (HEPES, 99.5+%) buffer was prepared to 25 mM and the pH was adjusted to 7.4 using dropwise addition of 10 M NaOH [75]. Dulbecco's Modified Eagle Medium (DMEM), with high glucose (4500 mg/L glucose) was used where indicated.

The conjugation reagents 1-ethyl-3-(3-dimethylaminopropyl) carbodiimide (EDC) and sulfo-N-hydroxysuccinimide (sulfo-NHS) were purchased from Pierce. The polypyrrole dopant, sulfopropyl methacrylate (SPMA), was purchased from Sigma Aldrich. A Milli-Q® plus (Millipore Inc., Bedford, MA) ultrapure water system supplied deionized water. All other common chemicals and solvents were purchased from Sigma Aldrich Co. (St. Louis, MO, USA) and were used as received, unless otherwise stated. Polyimide, 8 mil thick Cirlex® laminate were purchased as 23.5” x 23.5” sheets (Fralock, Valencia, CA) and cut into 6”x 6” sheets, cleaned, plasma treated and sputtered deposited with 100 Å TiW and 1,000 Å Au on one side (Thin Films Industries, Inc., Morrisville, PA). These served as a source of gold-coated polyimide electrodes used for *in vitro* studies.

4.2.2 Electrode fabrication and cleaning

Electrodes, shown in **Figure 29**, were rectangular, gold-coated polyimide (10 x 15 mm) masked with adhesive-backed polyimide tape to create a circular (ϕ = 0.7 mm) electrodeposition window, **Figure 29A**. Although polypyrrole was successfully electrodeposited onto this design, use of polyimide tape in this way produced variations between discrete electrodes. Furthermore, because the three characterization methods were inherently destructive and altered the electrode surface, three separate deposition areas per charge density performed in triplicate were required. An additional design, created in SolidWorks® and manufactured with an LS100 Gravograph CO_2 laser at 5% power (Gravotech Inc., Duluth, GA) started with a single rectangular piece of gold-coated polyimide (7.5 x 20 mm) and produced three isolated deposition areas as shown in **Figure 29B**. A single rectangular piece of polyimide tape (7.5 x 8 mm) was used as a mask to confine electrodeposition within the intended areas. With this design, polypyrrole could be deposited across all three sections at the same time, with the same charge density, then the sections could each be cut apart for use with one of the three characterization methods. Electrodes were cleaned first with DI water to remove residual dust from the laser, then with ethanol to remove organic compounds from the gold surface. Electrodes were cleaned with UV-ozone for 5 minutes (UV-ozone Cleaner, Boekel Industries Inc., Feasterville, PA) to remove adsorbed organic debris and rinsed in isopropyl alcohol. Finally, electrodes were made the working electrode of a three-electrode setup, suspended in PBS 7.4, and processed through 20 cycles of cathodic cleaning (scan rate 0.1 V/s, potential range 0 to -1.2V) to remove surface oxides [216].

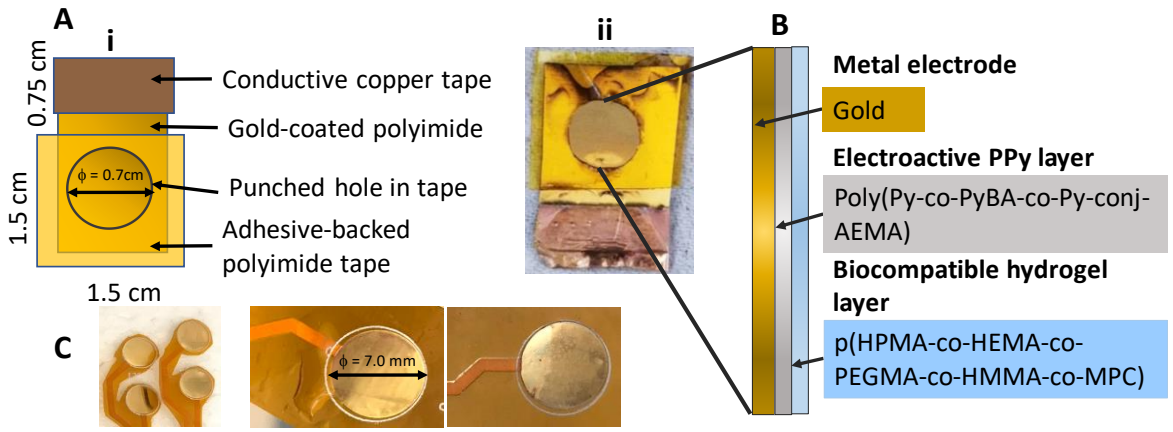

Figure 29. A) i) Design and construction of electrodes for in vitro assessments of electropolymerized charge densities of 0 – 1,000 mC/cm^2.

4.2.3 Preparation and electrodeposition of polypyrrole

A unique pyrrole solution was formulated for electrodeposition. To aid in the crosslinking of the hydrogel layer to the electrodeposited polypyrrole film, amino ethyl methacrylate (AEMA, 0.25M) was conjugated to pyrrolyl butyric acid (PyBA) via carbodiimide chemistry. The 1-ethyl-3-(3-dimethylaminopropyl) carbodiimide (EDC) bonds covalently to PyBA under acidic conditions, forming an unstable o-acylisourea intermediate. Then, N-hydroxysuccinimide (NHS) displaces EDC to form an ester intermediate with increased stability and efficiency for reaction with the primary amine group of AEMA. The chemistry for the conjugation of PyBA-*conj*-AEMA using EDC-NHS is depicted in **Figure 30.** This PyBA-*conj*-AEMA, combined with pyrrole (Py, 0.5M), pyrrolyl butyric acid (PyBA, 0.5M), and the dopant sulfopropyl methacrylate (SPMA, 0.25M) were incubated in the dark and pH adjusted to 5.0 in order to initiate electropolymerization from the pyrrole solution to yield poly(Py-*co*-PyBA-*co*-PyBA-*conj*-AEMA):SPMA which shall be referred to as PPy:SPMA. Electrodeposition of polypyrrole was conducted using a VerstaSTAT 4 Potentiostat/Galvanostat (Princeton Applied Research, AMETEK, Inc., Oak Ridge, TN) and analyzed with VersaStudio software (10 cycles, 0 to +0.75

V). Laser fabricated gold electrodes were made the working electrode of a three-electrode setup, with a large area platinum mesh as the counter electrode and Ag/AgCl (3 M KCl) as the reference electrode (RE803, ABTECH Scientific, Inc., Richmond, VA). A film of polypyrrole was deposited at seven charge densities (1, 5, 10, 30, 50, 100, 1,000 mC/cm^2).

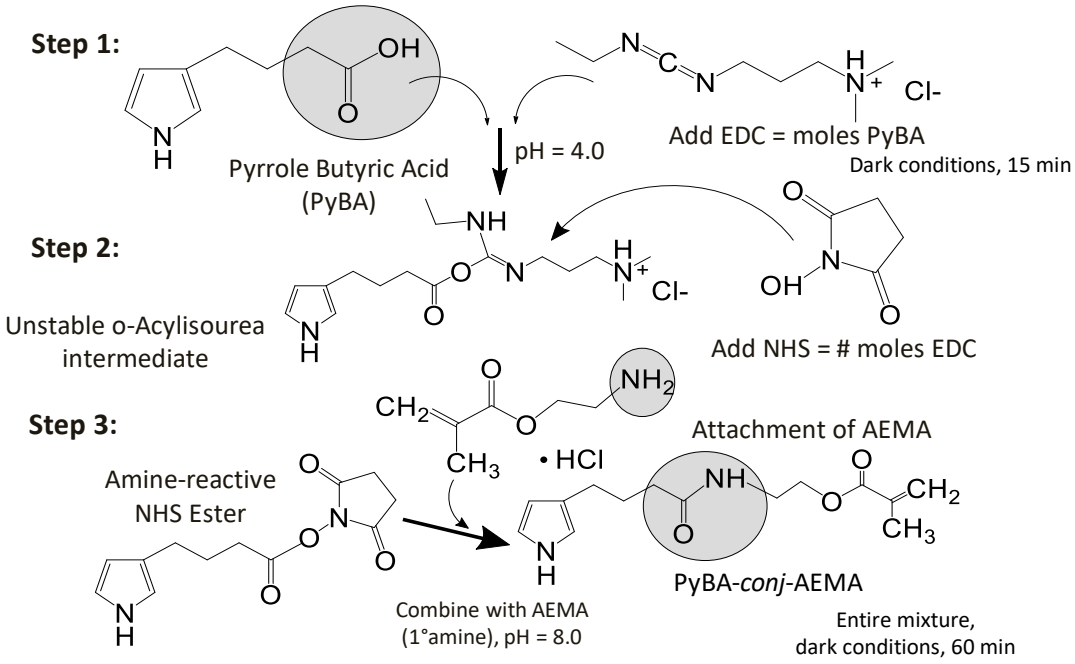

Figure 30. Schematic illustration of the conjugation of PyBA with AEMA to yield PyBA-conj-AEMA using EDC-NHS (Adapted from [273]).

4.2.4 Preparation and crosslinking of hydrogel

Fluorescent light bulbs within the laboratory space were fitted with UV filtering sleeves (TG-T8TG-UV, lightbulbsurplus.com) to maintain a UV-free environment for monomer handling. The monomers HEMA, TEGDA, and PEGMA were filtered through an alumina column to remove polymerization inhibitors added during manufacturing. The following solid monomers were added to a solution of the three filtered liquid monomers in deionized water: HPMA, HMMA, MPC, pNVP (biocompatible viscosity modifier), and DMPA (photoinitiator).

This cocktail was degassed with nitrogen, stirred on a stir plate, and placed in an ultrasonicator (Branson 1510, Gaithersburg, MD) to ensure complete dissolution of solid monomers in the liquid solution. The hydrogel cocktail was then pipetted onto the PPy:SPMA-modified gold electrodes and crosslinked for five minutes under UV (CX-2000, UVP, Upland, CA) . Hydrogels were hydrated in the DMEM (Dulbecco's Modified Eagle Medium, high glucose with 4500 mg/L glucose, Sigma-Aldrich Co., St. Louis, MO)) solution which was used for impedance measurements.

4.2.5 Characterization of PPy:SPMA|Hydrogel electrodes

Electrodes were characterized by scanning electron microscopy (SEM), multiple scan rate cyclic voltammetry (MSRCV) and AC electrical impedance spectroscopy (EIS). To compare differences in surface morphology across the specified range of charge densities, electrodes were sputter-coated with a gold layer using a Cressington 108 Sputter Coater (Cressington Scientific Instruments, UK) and placed on a viewing mount using carbon tape, with additional carbon tape across the top of the electrodeposited area to dissipate charge while imaging. Electrodes were viewed with a JEOL JSM-7500F FE-SEM at 2.0 kV and a magnification of x 20k. SEM images were analyzed using ImageJ software [282]. Prior to hydrogel layer attachment, PPy:SPMA-modified electrodes were characterized by multiple scan rate cyclic voltammetry (MSRCV) [283] in 50 mM potassium ferrocyanide/*ferricyanide* [$(K_4Fe(CN)_6)/(K_3Fe(CN)_6)$] in a background of 0.1M KCl. The Au|PPy:SPMA-modified gold electrodes were made the working electrode of a three-electrode setup, with a large area platinum mesh as the counter electrode and Ag/AgCl (3 M KCl) as the reference electrode (RE803, ABTECH Scientific, Inc.). MSRCV measurements were taken across a voltage range of 0 to 0.75 V at variable scan rates (10, 25, 50, 75, 100, 125, 150, and 200 mV/s). Two cycles were applied to allow the system to reach a steady

state, with the first cycle discarded and the second set aside for analysis using the Randles-Sevcik equation. Electrical impedance spectra were obtained with a VerstaSTAT 4 Potentiostat/Galvanostat (Princeton Applied Research, AMETEK, Inc., Oak Ridge, TN) and analyzed with VersaStudio software (VersaStudio version 1.51, AMETEK, Inc., Oak Ridge, TN). PPy:SPMA-modified gold electrodes were made the working electrode of a two-electrode setup, with a large surface area platinum mesh acting as both the counter and reference. Measurements were taken across a frequency range of 0.01 Hz to 1 MHz at an RMS amplitude of 7.07 mV with 5 points per decade. Impedance parameters such as membrane and charge transfer resistance were obtained in ZSimpWin software version 3.60 (AMETEK, Inc., Oak Ridge, TN) through equivalent circuit analysis using the Randles R[QR] model. The Au|PPy:SPMA|Hydrogel electrodes were similarly characterized. In order to most closely simulate internal body conditions, electrodes were immersed in DMEM and incubated at 37 $^{\circ}$C using a VWR2310 Water-Jacketed CO_2 Incubator (Marshall Scientific, Hampton, NH) while carrying out these experiments.

4.2.6 Statistical Analysis of Impedance Parameters

Impedance values for cleaned and pristine electrodes, electrodes modified following electropolymerization with polypyrrole:sulfopropyl methacrylate (PPy:SPMA), and electrodes modified by PPy:SPMA and coated with a UV-crosslinked poly(HEMA-*co*-HPMA-co-MPC)) hydrogel are reported as average values with n = 5. Pearson's correlation coefficient compared with charge density is reported for electroactive area, percent fracture area, charge transfer resistance, and membrane resistance, with +/- 0.8 representing a strong correlation.

4.2.7 Fabrication and Performance of Lactate and Glucose Responsive Hydrogel Biosensors Incorporating Polypyrrole and Carbon Nanotubes

Blank hydrogels were prepared using the monomers 2-hydroxyethyl methacrylate (HEMA), 2-hydroxypropyl methacrylamide (HPMA), poly(ethylene glycol)(360)methacrylate (PEG(360)MA), N-Tris(hydroxymethyl)methyl]acrylamide (HMMA, 93%), the cross-linker tetra(ethylene glycol) diacrylate (TEGDA, technical grade), the biocompatible viscosity modifier polyvinylpyrrolidone (pNVP, MW ~1.3M) and the photo-initiator 2,2-dimethoxy-2-phenylacetophenone (DMPA, 99+%) purchased from Sigma Aldrich Co. (St. Louis, MO). Blank hydrogels were made increasingly conductive and responsive by inclusion of 1.0 wt% PPy:PSS nanoparticles (Sigma-Aldrich) to support redox mediation. SWCNTs (purity, 95wt%) and GOx (EC 1.1.3.4 from Aspergillus niger, G7141-250KU, type X-S, 146,000 units/g solid, Sigma Aldrich) or LOx (EC: 1.13.12.4 from Pediococcus sp., L-1175-1xKU, 1K units/g solid, A.G. Scientific™) were used to create supramolecular conjugates (SWCNT-GOx, SWCNT-LOx) fabricated via ultrasonication and ultracentrifugation according to previously published procedures. Samples were stored at 4 °C. Amperometric dose-response curves (+0.65V vs. Ag/AgCl) were produced for hydrogel-coated, gold-on-polyimide electrodes for 0.0-50.0 mM lithium-L-lactate and D-(+)-glucose (Sigma-Aldrich) in 0.01 M PBS. Amperometric dose-response curves (+0.65V vs. Ag/AgCl) were produced for hydrogel-coated, gold-on-polyimide electrodes for 0.0-50.0 mM lithium-L-lactate and D-(+)-glucose (Sigma-Aldrich) in 0.01 M PBS.

4.2.8 Surface modification and characterization of systems for improving sensitivity of amperometry

Several electrode substrates like glassy carbon electrode (ϕ = 3 mm, Bioanalytical Systems, Inc., West Lafayette, IN), graphitic carbon electrode (ϕ = 0.47 cm, Bioanalytical Systems, Inc.,

West Lafayette, IN), titanium electrode (ϕ = 0.47 cm, Bioanalytical Systems, Inc., West Lafayette, IN), platinized stainless steel electrode (ϕ = 0.48 cm, Bioanalytical Systems, Inc., West Lafayette, IN) platinized for a charge density of 50 mC/cm^2 using one-pot platinization technique [79], Platinum microelectrode (Pt100, ϕ = 100 µm, Bioanalytical Systems, Inc., West Lafayette, IN), and gold microelectrode (Au 100, ϕ = 100 µm, Bioanalytical Systems, Inc., West Lafayette, IN) cleaned using alumina polish (15 um, Bioanalytical Systems, Inc., West Lafayette, IN) were tested by multiple scan rate cyclic voltammetry using the Fe(II)/Fe(III) system as a probe to reveal changes in the effective surface area. $Area_{effective}$ was found using the parameters from the Randles-Sevcik equation. The analysis for the ratio of $Area_{effective}$ versus $Area_{calculated}$ was accomplished to reveal the system showing high current density (A/cm^2). Electrical impedance spectra were obtained with a VerstaSTAT 4 Potentiostat/Galvanostat (Princeton Applied Research, AMETEK, Inc., Oak Ridge, TN) and analyzed with VersaStudio software (VersaStudio version 1.51, AMETEK, Inc., Oak Ridge, TN) to reveal the charge transfer resistance (R_{CT}) of these subtrates.

4.3. Results and Discussion

4.3.1. Evolving surface morphology of polypyrrole films

Potentiostatic electropolymerization of Py, PyBA and PyBA-*conj*-AEMA to various charge densities (0-100 mC/cm^2) produced an inherently conductive polymer layer, [P(Py-*co*-PyBA-*conj*-AEMA):SPMA], on the gold electrode. **Figure 31A** shows SEM image analysis of polypyrrole across seven electrodeposition charge densities (1, 5, 10, 30, 50, 100 and 1,000 mC/cm^2), compared to a bare gold surface. Isolated deposits of polypyrrole were observed at 1 mC/cm^2, with a semi-continuous film forming at 5 mC/cm^2. To fully exploit the electroconductive properties of polypyrrole, a uniform, homogenous film with consistent thickness and minimal surface features was anticipated. The density of such features gradually decrease with electrodeposition charge density up to 50 mC/cm^2. Above this charge density, a second film appears to begin to deposit on top of the first, introducing larger surface features such as those seen at 100 mC/cm^2. At 1,000 mC/cm^2 saturation was observed. The plot for percent area with surface features is shown in **Figure 31B**, showing the clear minimum at 50 mC/cm^2.

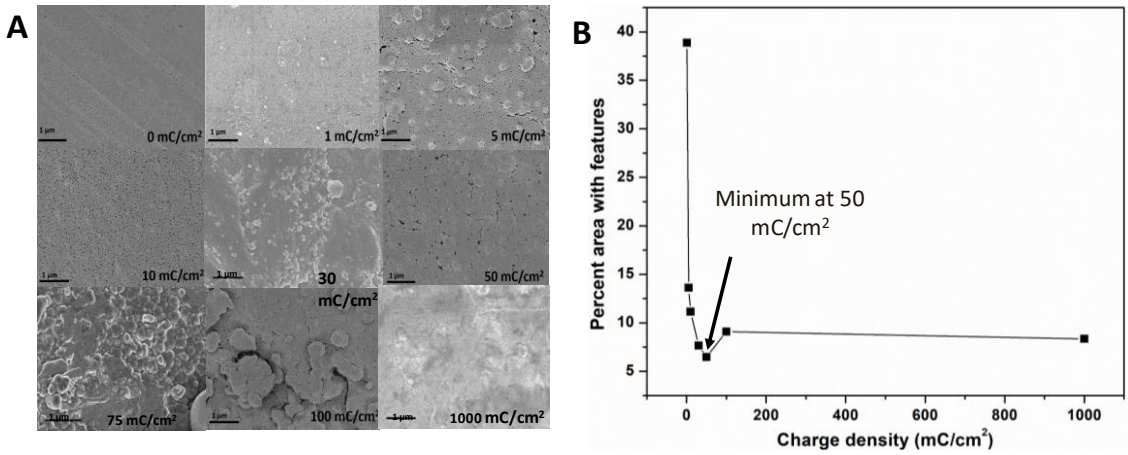

Figure 31. A) SEM images of PPy:SPMA electrodeposited onto gold-sputtered polyimide via potentiostatic electropolymerization at charge densities at 0, 1, 5, 10, 30, 50, 100 ,and 1000 mC/cm^2, each taken at acceleration voltage 2.0 kV and ×20 k magnification.

4.3.2. Determination of effective electroactive area from multiple-scan rate cyclic voltammetry

Multiple-scan rate cyclic voltammetry in Fe(II)/Fe(III) serves to delineate the ability of the substrate electrode to support the one-electron charge transfer reaction associated with the reversible Fe(II)-Fe(III) couple. In this regard, performance at bare the gold electrode serves as a reference or control condition to which PPy:SPMA-modified electrodes may be compared. The anodic peak current, i_{pa}, was determined at each scan rate for each PPy:SPMA modified gold electrode. **Figure 32A** is a plot of anodic peak current, i_{pa}, as a function of the square root of scan rate, $\boldsymbol{\nu}^{1/2}$ $(V/s)^{1/2}$, in the familiar form of the *Randles–Sevcik equation* (Eq. 1) [284]. *The plot following electrodeposition to* 1 mC/cm^2 demonstrates a similar linear relationship with scan rate when compared with bare gold with only a modest change in slope consistent with SEM observations at that charge density. The addition of 5, 10 and 30 mC/cm^2 reveals considerably reduced anodic current and independence of increasing scan rate. This behavior is consistent with a diffusion free, surface confined or mediated reaction. The linear relationship once again emerges at and above 50 mC/cm^2, with only a slight increase in linearity at 100 mC/cm^2 and a

further larger increase at 1,000 mC/cm^2. These patterns confirm a return to the active diffusion-controlled redox reaction at an electrode-active surface. The slopes of each line corresponding to the various electrodeposition charge densities was used to calculate the effective electroactive area via the Randles-Sevcik equation (Eq. 6).

Where i_{pa} is the peak anodic current (μA), n is the number of electrons involved in the redox reaction, A_{eff} is the effective electroactive area (cm^2), D_o is the diffusion coefficient for ferri/ferrocyanide, C_o is the concentration of ferri/ferrocyanide (mM) in solution, and ν is the scan rate (V/s). Here electroactive area is defined as the portion of the electrode's surface actively engaged in charge transfer with the ferri/ferrocyanide solution. Given that the test electrodes were comprised of two conductive materials, Au and PPy:SPMA, this could refer to charge transfer between gold and solution, or between polypyrrole and solution. A charge density of 1 mC/cm^2 produced electrodes with an electroactive area of 8.83 mm^2, 79% of the actual reference electroactive area (11.22 mm^2). Given that SEM revealed only a few isolated deposits of polypyrrole at this charge density, electroactive area most likely corresponds with exposed bare gold in this case. Similar to the observed peak current trends, 5, 10, and 30 mC/cm^2 exhibit a substantial decrease in electroactive area (0.45, 0.36, and 0.38 mm^2 respectively), with the polypyrrole films formed at these charge densities acting as an barrier against charge transfer between the electrode and Fe(II)/Fe(III) in solution. Electroactive area increases to 2.96 mm^2 at 50 mC/cm^2, suggesting a threshold at or near this charge density at which polypyrrole begins exhibiting its own electrode-like behavior. Electroactive area further increases only slightly at 100 mC/cm^2 (3.46 mm^2), and increases appreciably at 1,000 mC/cm^2 (5.88 mm^2 or 52% of bare gold). As shown in **Figure 32B**, polypyrrole initially acts as a barrier to charge transfer until 50 mC/cm^2. Above 50 mC/cm^2, it acts like an electrode material [285] and supports diffusion linked

charge transfer of Fe(II)/Fe(III) from solution. It is noteworthy that the electrode-activity of Au|PPy:SPMA, as manifiest in the effective surface area, follows a similar trend as the SEM feature analysis, with 50 mC/cm^2 emerging as a charge density of interest.

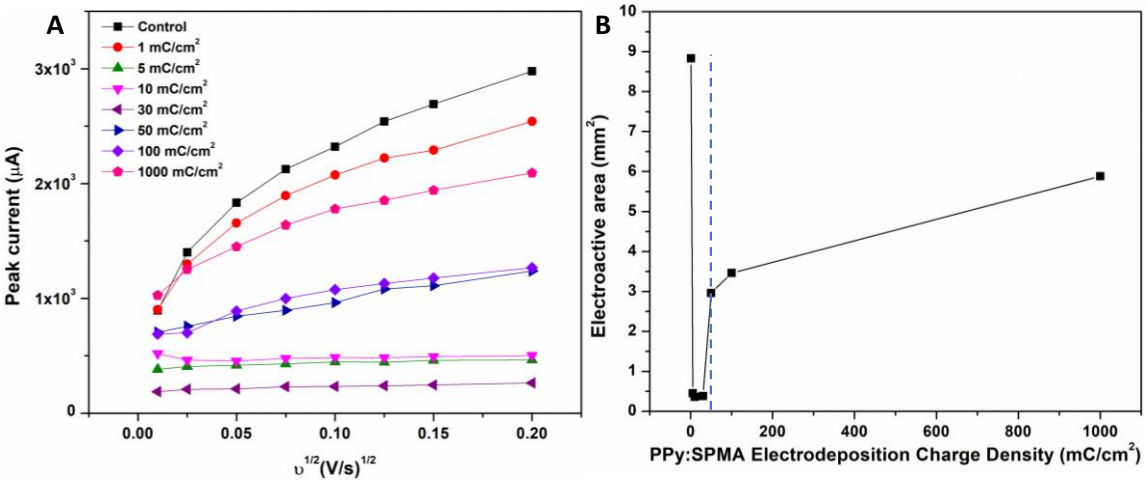

Figure 32. A) Plots of anodic peak current, i_{pa}, versus the square root of eight scan rates (10, 25, 50, 75, 100, 125, 150, 200 mV) for seven charge densities of electrodeposited PPy:SPMA and control (0 mC/cm^2).

4.3.3 Changes in charge transfer resistance by EIS

EIS was used to investigate the electrode characteristics of Au|PPy:SPMA as well as the impact of the hydrogel layer on the impedance characteristics of Au|PPy:SPMA|Hydrogel. **Figure 33A** shows the Nyquist plots for control and the seven charge densities studied in DMEM at 37 ºC and 5% CO_2. **Figure 33B** depicts the plot of the charge transfer resistance as a function of the electrodeposition charge of PPy:SPMA films. Electrical impedance spectroscopy (EIS) revealed that on average, gold electrodes electrodeposited with polypyrrole and hydrogel exhibited an 82% decrease in charge transfer resistance, R_{CT}, compared with bare gold electrodes. Polypyrrole is known to contribute its characteristic redox chemistry with E_{OX} and E_{RED} corresponding to ~0.2 V [286] and -3.6 V [286, 287], respectively. **Table 12** shows the impedance parameters extracted from R(QR) model fitting, including R_M (Ω) and R_{CT} (Ω) for the

control and the seven charge densities. Technical triplicates of PPy:SPMA films formed from 50 mC/cm^2 experimentally showed modest *in vitro* variability. A Pearson's correlation coefficients[288] analysis between the electrodeposition charge density and the various parameters extracted from model fitting of the EIS data established a strong anti-correlation between electrodeposition charge density and charge transfer resistance, R_{CT}, of Pearson's correlation coefficient, r = -0.83. All other parameters were uncorrelated or very weakly correlated (Due to membrane resistance, R_M, the Pearson's correlation coefficient, r=0.11).

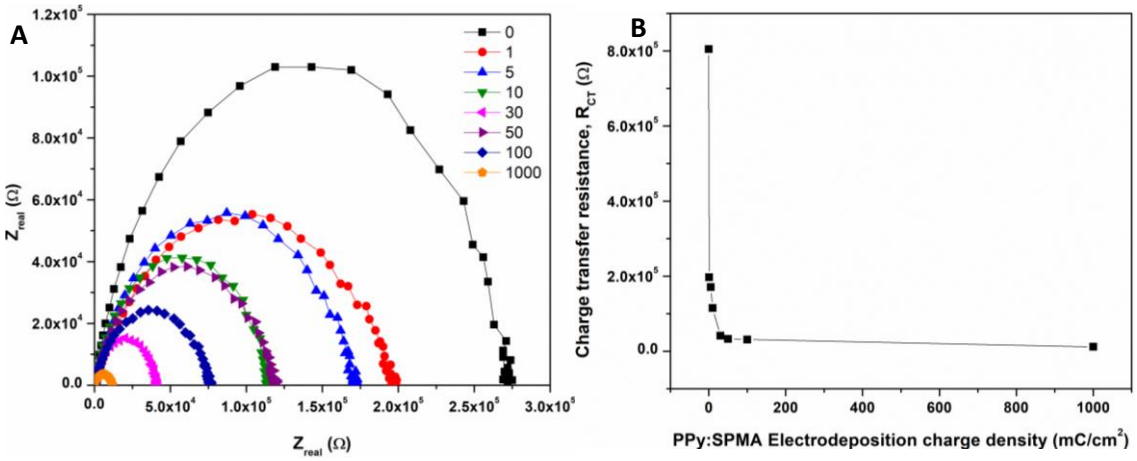

Figure 33. A) Nyquist plots showing real and imaginary components of the complex impedance, where, for a simple Randles R(QR) equivalent circuit, the rightmost x-intercept of each curve represents the sum of membrane resistance and charge transfer resistance.

Table 12. Electrical impedance parameters obtained for the range of charge densities studied, including membrane resistance (R_M) and charge transfer resistance (R_{CT}).

Charge Density (mC/cm²)	R_M (Ω)	R_{CT} (Ω)	Y_o (S-sec^n)	n	χ^2
0	77.67	8.05E+5	6.45E-6	0.84	1.08E-4
1	100.8	1.97E+5	3.44E-5	0.65	1.09E-4
5	69.34	1.71E+5	5.41E-5	0.73	1.13E-4
10	67.06	1.15E+5	1.00E-5	0.80	1.08E-4
30	53.35	4.12E+4	1.14E-5	0.80	1.73E-4
50	87.64	3.25E+4	1.43E-4	0.91	3.72E-4
100	88.21	3.10E+4	1.63E-4	0.72	1.09E-4
1000	21.58	1.16E+4	1.06E-4	0.71	6.36E-4

4.3.4 Interlayer attachment

Films were incubated in DMEM at 37 ºC and 5% CO_2 and monitored for delamination. Up to 72 h films maintained their integrity. After 72 h hydrogel layers showed some evidence of lifting, but not complete delamination. Electrodeposited PPy:SPMA films that did not contain the PyBA-*conj*-AEMA (control) were similarly prepared and incubated. These films produced interlayer delamination within 30-45 min and upon hydration. Electrode assemblies were tested in the DMEM solution at current intensities from 20mA - 100mA (biphasic pulses, 1.0 Hz), with maximum current limited to 30 mA. Current was passed through these electrodes to test the coating stability. The stability test for the electrodes subjected to neurostimulation currents limited to 30 mA showed a stability of 0.5 hour. Future work will focus on improving the interlayer adhesion, measurement of the *in vitro* biocompatibility and the conduct of animal studies.

4.3.5 Amperometric sensing for LOx/GOx biotransducers

From the amperometry, CNTs being inherently conductive, show more current when incorporated into the LOx hydrogel. CNTs also serve to facilitate Direct Electron Transfer (DET)

to the electrode from the active site of the enzyme. Addition of PPy:PSS, an intrinsically conductive polymer (ICP) further adds to the current response of the hybrid hydrogel containing LOx-CNT and PPy. The most complex hydrogel composed of LOx-CNTs and PPy:PSS showed the highest sensitivity (5.0 $x10^{-4}$ A/mM). The sensitivity decreased from the most complex LOx-CNT|PPy:PSS/Gel to the LOx/Gel control which was $2.0x10^{-4}$ A/mM. The sensitivities of the GOx-CNT|PPy:PSS/Gel and GOx/Gel control to glucose were $5.0x10^{-4}$ and $4.0x10^{-4}$ A/mM respectively. Thus, addition of supramolecular complexes based on SWCNTs and PPy:PSS increased the current response and sensitivity from lactate and glucose (not sown) responsive hydrogel biotransducers. **Figure 34** shows the glucose and lactate hydrogels of increasing complexity, and reports the sensitivity of these gels compared to that of literature. These can be extended to sense glucose and lactate of varying concentrations pertinent to various pathologies.

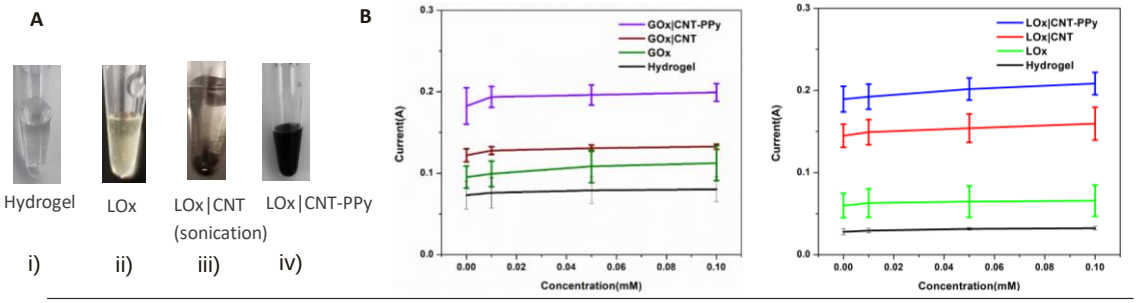

Parameters	Hydrogel		GOx (Control)	LOx (Control)	GOx|CNT	LOx|CNT	GOx|CNT-PPy	LOx|CNT-PPy	Literature	
	Response to Glucose	Response to Lactate							Glucose sensor	Lactate sensor
Response time(sec)	115	83	278	60	117	50	106	67	3	-
Sensitivity: A/[mM]	3.0E-04	9.0E-05	4.0E-04	2.0E-04	2.0E-04	6.0E-04	5.0E-04	5.0E-04	4.05E-04	7.97E-04
LOD(mM)	13.012	7.640	6.352	11.720	7.614	4.230	8.190	4.660	0.007	0.003

Figure 34. Glucose and Lactate responsive hydrogels of increasing complexity; i) Blank hydrogel cocktail, ii) LOx/Gel, iii) LOx-CNT/Gel, iv) LOx-CNT|PPy:PSS/Gel, B) Amperometric responses, and C) Sensitivity from four types of lactate responsive hydrogels [286].

4.3.6 Surface modification and characterization of systems for improving sensitivity of amperometry

The surface modification and characterization of systems for improving sensitivity of amperometry showed graphitic carbon electrode as the electrode system with the highest current density as per **Figure 35 A and B**. This was followed by platinum, glassy carbon, gold, platinized stainless steel, and titanium electrode. γ was the correction factor used for area (Eq. 25).

$$A_{eff} = A_{geometric} * \gamma \quad (25)$$

γ>1 indicated an enhanced film and γ<1indicated a passivated electrode.

As per **Figure 35 C and D**, impedance was modeled according to (Eq. 26)

$$Z_{tot} = R_M + \frac{R_{CT} - jR_{CT}^2 C_{DL}\omega}{\omega^2 R_{CT}^2 C_{DL}^2 + 1} \quad (26)$$

R_{CT}/γ was of the order of ($x10^8$) for titanium, with the order of R_{CT}/γ of graphitic carbon ($x10^2$), for glassy carbon and platinum ($x10^5$), for gold and platinized stainless steel ($x10^6$). For the carbon-based electrodes, graphite has more sp^2 domains than glassy carbon, hence capability to support conduction is more (pz orbitals).

Area available (calculated) for graphite ($1.73\ x10^{-1}\ cm^2$) is much more than glassy carbon ($7.0\ x10^{-2}\ cm^2$). Thus, further experiments would entail using glassy carbon electrode to check improved sensitivity for amperometric sensing. Carbonization of electrode can be performed on the gold of the biosensor system to improve the sensitivity for amperometric sensing using LOx/GOx biotransducers. Structurally, glassy carbon is an amorphous form of carbon, whereas graphite has a more ordered structure, with distinct planes – the basal plane and the edge plane.

The edge plane is considerably more conductive than the basal plane. Glassy carbon is mechanically more durable than pyrolytic graphite.

A)

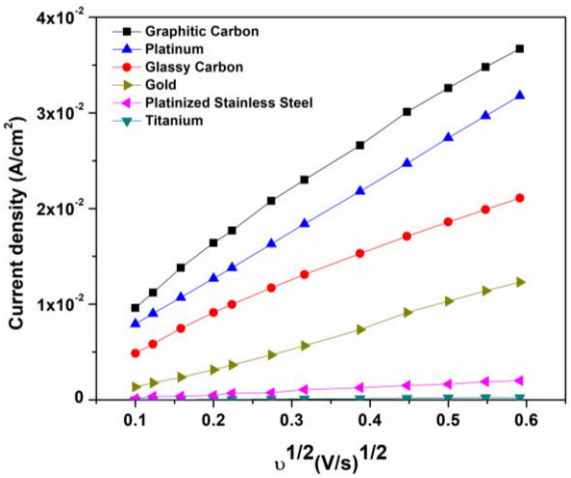

B)

Electrode material	Slope of R-S Plots	γ
Graphitic Carbon	5.5E-02	1.58
Platinum	4.9E-02	1.40
Glassy Carbon	3.3E-02	0.94
Gold	2.3E-02	0.66
Platinized Stainless Steel	3.8E-03	0.11
Titanium	4.0E-04	0.01

C)

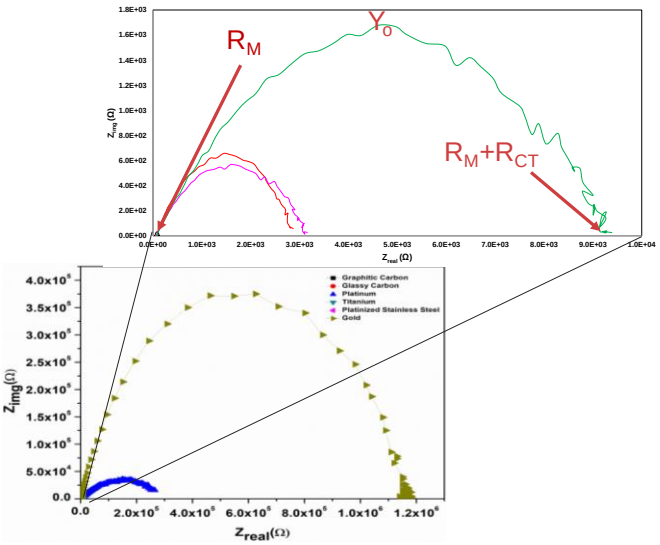

D)

Electrode material	R_{CT}	R_{CT}/γ (Ω)
Graphitic Carbon	1.90E+02	1.20E+02
Platinum	3.04E+05	2.17E+05
Glassy Carbon	1.17E+05	1.24E+05
Gold	1.16E+06	1.76E+06
Platinized Stainless Steel	1.64E+05	1.49E+06
Titanium	5.60E+06	5.60E+08

Figure 35. Characterization using cyclic voltammetry in 50mM Fe(II)/50mM Fe(III): A)Plots of current density (anodic peak current, ipa/cm^2), versus the square root of twelve scan rates (10, 15, 25, 50, 75, 100, 125, 150, 200, 250, 300, 350 mV) on the electrode substrates of graphitic carbon, platinum, glassy carbon, gold, platinized stainless steel and titanium.

4.4 Conclusion

Neurostimulation electrodes were successfully modified for the potential treatment of spinal cord injury and vagus nerve stimulation. Test electrodes electrodeposited with polypyrrole and hydrogel exhibited markedly decreased interfacial impedance over the bare gold electrodes currently used in neurostimulation techniques. Characterization techniques revealed deposition patterns of polypyrrole at different charge densities as well as electrochemical properties such as electroactive area and charge transfer resistance. An optimum charge density of 50 mC/cm^2 was identified for use in neurostimulation based on SEM analysis and electroactive area calculations. Future work will explore interfacial impedance of modified electrodes *in vivo* in porcine models at the Houston Methodist Research Institute, Houston, TX. The final bio-electrode assembly can be improved by incorporating vascular endothelial growth factor (VEGF) [289], anti-inflammatory agents [290], various drug payloads [291], and rendering some electrode pads as enzyme-based biosensors.

Preliminary experiments showed the sensitivity of LOx-CNT|PPy:PSS/Gel as 5.0×10^{-4} A/mM, and of GOx-CNT|PPy:PSS/Gel as 5.0×10^{-4} A/mM. Future work to improve the sensitivity of the amperometric system would entail building the LOx/GOx biotransducer on glassy carbon substrate. Explorations for the medium for the dose-response curves can include Tetramethyl Urea-Urea-Water conjugates[292] or the use of Dimethyl sulfoxide. The system can be checked for sensitivity for chronoamperometry at -0.475 V, and 0.6 V potentials in deoxygenated (nitrogen gas purging) and fully oxygenated (air purging) conditions in 5 mM concentrations of lactate and glucose.

CHAPTER V

FUSING FIVE PHYSIOLOGICAL BIOMARKERS: TOWARD A HEMORRHAGE INTENSIVE SEVERITY AND SURVIVABILITY (HISS) SCORE

5.1 Introduction

Trauma accounts for 47% of mortalities in individuals 1-46 years of age in the United States [6]. Trauma-induced hemorrhage with its attendant peripheral vasoconstriction [293], [294] insulin resistance [295], hyperlactatemia, [296], [297], [298] acidosis [299], hyperkalemia [89], [300] and hypoxia [12], [301] can rapidly lead to death or may be followed by Multiple Organ Dysfunction Syndrome (MODS), a consequence of a "cytokine storm", which can also be fatal [299], [301]. The field triage decision scheme for the national trauma triage protocol provides guidelines to identify the status of the patient [302]. The physiological criteria includes identification of vital signs such as; systolic blood pressure (Hypotension <90 mmHg) [303], [304], [305], [306], abnormal respiratory rate (<10 or >29 breaths per minute) [302], abnormal heart rate (Tachycardia >100 beats per minute) [307], [308] and the Glasgow coma scale (≤ 13) [309, 310]. The Glasgow coma scale categorizes the patients according to the severity of head injury. Simple Triage and Rapid Treatment (START) is the commonly used algorithm for mass casualty triage in the USA [311], [312], [313], [314], which is used in conjunction with secondary triage for Secondary Assessment of Victim Endpoint (SAVE) when the resource supply is restricted [311]. START and SAVE employ criteria such as respiratory rate, cognitive function (ability to listen and respond to commands), and radial pulse to identify the category for triage. Another example is the Injury Severity Score (ISS) [315] based on the Abbreviated Injury Scale (AIS) system which aggregates the assessed injury to six regions of the body and establishes correlations with mortality and morbidity [316]. A MODS severity score was

developed by Marshall *et al.* in 1995, wherein a score (0-4) is applied following physiologic measurement of dysfunction in 6 organ systems (i) respiratory function (pO_2/FIO_2 ratio), ii) renal function (serum creatinine), iii) liver function (serum bilirubin), iv) cardiovascular function (PAR), v) Hematologic (Platelet count) and vi) Neurologic (Glasgow Coma Score)) [105]. The total number of input points were then added to achieve a score corresponding to the patient's ICU mortality %, hospital mortality %, and ICU stay.

Since the introduction of the MODS score, new rapidly deployable micro-analytical technologies have enabled measurement of key physiological indicators and the opportunity for the emergence of scores based on molecular biomarkers of physiological stress. A Hemorrhage Severity and Survivability Score (HISS) is herein introduced to allow for patient stratification based on the fusion of micro-analytical measurements of multiple physiological biomarker values [317]. HISS is a severity index intended as an adjunct to inform the providers of healthcare to the victims of hemorrhaging trauma of the criticality of the patient's health and so assist them in the delivery of timely and appropriate attention and care. HISS, therefore, can help in timely triage and in the stabilization of the most critically ill patients, and as a consequence, reduce patient mortality. An adjunct device in the form of an indwelling biosensor system, the Physiologic Status Monitoring (PSM) Biochip, has been proposed and is under development to help healthcare providers of trauma care in mass military and civilian triage situations [51, 318]. A dual-responsive biosensor for glucose and lactate has been proposed, designed, fabricated and tested in rodent and piglet animal models of hemorrhaging trauma [318]. The PSM Biochip is a bio-SONDE, an indwelling device which measures, monitors and wirelessly transmits physicochemical information from within a victim of hemorrhaging trauma [51]. Here, a penta-analyte bio-SONDE capable of acquiring the physiological data pertinent to hemorrhagic shock

states is proposed as the source of the data for subsequent fusion. When implanted intramuscularly, the PSM-Biochip enables the continuous, real-time monitoring of the patient's physiological status via the following key biomarkers; glucose, lactate, pH, potassium and oxygen tension. Such a system has the potential to go beyond single immediate datum (stat) capability to reveal evolving and predicted temporal trend status. This bio-SONDE, combined with a wireless processing hardware and a software algorithm to enable data fusion from the five identified biomarker analytes, can guide evidence-based decision making [319] derived from the real-time pathophysiological profile of the patient.

The present work evaluates multiple data fusion algorithms and seeks to identify the minimum patient and expert data sets needed to arrive at reliable and confident patient stratification decisions using the HISS Score. Here, multiple patient physiological data are originated and multiple individual experts score the data. A key consideration is thus the real-time fusion of disparate pathophysiological data to yield an actionable HISS score. Such data integration has medical and biomedical engineering applications such as in rapid, wearable health monitoring and internet of things (IoT) monitoring [320], [321], [322]. Data fusion can also be applied to implantable devices to generate data telemetry systems [323] with patient profiles [324]. Decision trees [325], support vector machine [326], neural networks [327], uncertainty index [328] and hybrid intelligent systems consisting of fuzzy logic and genetic algorithms [329] have been employed as classification approaches for data fusion in medicine. Decision tree classifiers were used to build a classification model in the form of a tree from the patient biomarker data [330]. The classifier provides a score for the data by testing each attribute and sorting and classifying particular instances in the data [331]. Ensemble bagged decision trees helped to reduce variance by the 'bagging' effect [332]. The support vector machine classifier

[333] makes use of an optimal hyperplane and calculates the margin or the distance of the points from the hyperplane [334]. The points closest to the hyperplane are called the support vectors [335]. Support vector machines are often used because they are robust [336] and fast [333]. Neural networks mimic the structure of biological neurons, have input, output and/or hidden layers, and propagate to adjust the weights between the elements of the networks [337]. They are often used because of their value in tuning of data [338]. Genetic algorithms are employed to find an optimal solution for systems based on natural evolution [339] and have been used in time-series based neural networks [340] and in steady-state gene regulatory networks [341]. Similar approaches for the application of artificial intelligence in medicine and for developing a score for patients in the ICU [342] include the DeepSOFA [343], an automated alert functions for the patient status [344]. Decision support-systems employing an artificial intelligence clinician for sepsis in the ICU have also been generated [345].

In many of the machine learning applications, it is assumed that data belong to a certain class with complete certainty. However, in some applications, such hard class association does not accurately reflect the true nature of the problem. In real-world problems, different forms of uncertainty such as fuzziness, imprecision, and incompleteness may coexist. This is the case specifically in applications where expert knowledge plays a crucial role. Expert data tends to be incomplete and in many cases uncertain, though less so than naive information, and in some cases may be erroneous. Possibility theory [346] is a framework devoted to the handling of incomplete and/or uncertain data and is particularly applicable to expert knowledge. Unlike probability theory, possibility theory uses a pair of dual set-functions, namely possibility and necessity measures which make it capable of representing partial ignorance [347]. The possibility rule-based classification using function approximation (PRBF) algorithm has been

shown to successfully handle the uncertainty in class labels of data and make an efficient use of the available data provided in the incomplete expert evaluation, a condition which is generally neglected in traditional supervised learning techniques. In Nazmi et al. [348], this algorithm was used to determine the at-fault level of drivers engaged in rear-end collision car accidents using labels calculated from evaluations elicited from five subject-matter experts. Possibility labels may be directly extracted from an expert [349] by a) the expert weighting the possibility of data belonging to each of the given c classes by a number between 0 and 1, or 2) to use possibility histograms from an empirical distribution of multiple expert opinions.

To achieve these objectives, viable penta-analyte patient data sets should be available. However, in the absence of actual patient data, strategies to generate synthetic data sets must be developed. Thus, a secondary objective of this work was to generate sufficient data using a synthetic data generation algorithm that produces Sensible Fictitious Rationalized Patient (SFRP) data. The SFRP algorithm (detailed later) creates a hidden seed layer and then generates biomarker values with filters to add noise/fuzziness and introduce variance to the five physiological biomarkers of interest. Practitioner input was sought in refining the filters and noise/fuzziness for each biomarker. The five biomarker values for each SFRP maps to a single output, the HISS score. The SFRP data was then shared with practicing physician experts who provided their individually rationalized HISS scores. Thus, the physicians' scores serve as the ground truth but carry the inherent uncertainty born from disagreement among experts. Multiple SFRP data sets scored by a single expert, allowed an assessment of intra-professional variance. Correspondingly, multiple physicians providing ground truths of a single SFRP data set allowed accommodation of inter-professional variations. Multiple physician experts, given the results of a single set of measurements of physiological biomarkers, evaluate the status of patients in the

form of a HISS score. In the decision-making processes, which incorporates bioanalytical diagnostic data and expertly sourced scores, uncertainty is inevitable. That is, given a reported set of measurements of the five biomarkers for a patient, different physicians may provide different evaluations, i.e. scores, for the status of the patient. In such cases, it is possible to represent the uncertain scores in the form of a range of values. The generated data were used to make predictions for the status of the hemorrhaging patients by training a decision tree classifier and rule-based evolutionary classifier [347] to handle uncertainty in scores. The results of training models are presented in terms of their prediction accuracies. Furthermore, this allowed forecasting of the size of the patient data set and the number of clinician experts required to achieve stratification accuracies of 99% and 99.9%.

5.2 Materials and Methods

On-line data engines were searched for the availability of anonymized actual patient biomarker data for the hemorrhaging trauma patient (glucose, lactate, pH, potassium and oxygen tension). Owing to necessary HIPAA-based security policies at hospitals, actual data for hemorrhaging patients could not be directly accessed. The authors are currently in discussions with clinicians to gain access to diagnostic data sets under appropriate approvals. Accordingly, the classification methods were each employed on the synthetically derived Sensible Fictitious Rationalized Patient (SFRP) data.

5.2.1 Patient data generation -Sensible Fictitious Rationalized Patient data and evaluation by practitioners

In lieu of actual patient data, synthetic (SFRP) data sets were generated via a scripted algorithm in Python 3.7.0. The flowchart for the SFRP data set generator is shown in **Figure 36** and is based on the pathophysiological data in **Table 13**. The general algorithm begins with a

seeded hidden layer of HISS scores that ranged from low(0) to severe(4). The initial seeding distribution for trauma scores was evenly distributed among the five levels. Each of the five biomarker values associated with each level was subsequently filled by randomly selecting a value from within a pathophysiological range that can be attributed to that trauma level (based on normal physiologic values and specific trauma and hemorrhage perturbations). The noise was introduced by controlling the relative level of deviation from initially seeded values into other trauma regimes – i.e. letting initially chosen values drift into other regimes not originally occupied by the primary, hidden trauma seed score. Glucose noise was based on potentially convoluting scenarios (adrenergic response) or by a simple, tunable probability of taking on a value, not within the seeded range. Lactate was similarly assigned. Potassium noise was added via post mathematical calculation. Acidosis (pH) noise was introduced by allowing for physiologically normal values to be taken at any hidden seed (with the rationale being that pH is a late and severe biomarker). Oxygen tension (pO_2) noise was introduced via a convoluting scenario (respiratory compensation based on pH – determined randomly) and simple, random noise. The algorithm, in the most direct sense, allowed for initial seed values to bleed over into other regimes and create data that was confounded. For proof of concept, random number generators of no bias were used – although extension into Gaussian and other distributions may be readily implemented.

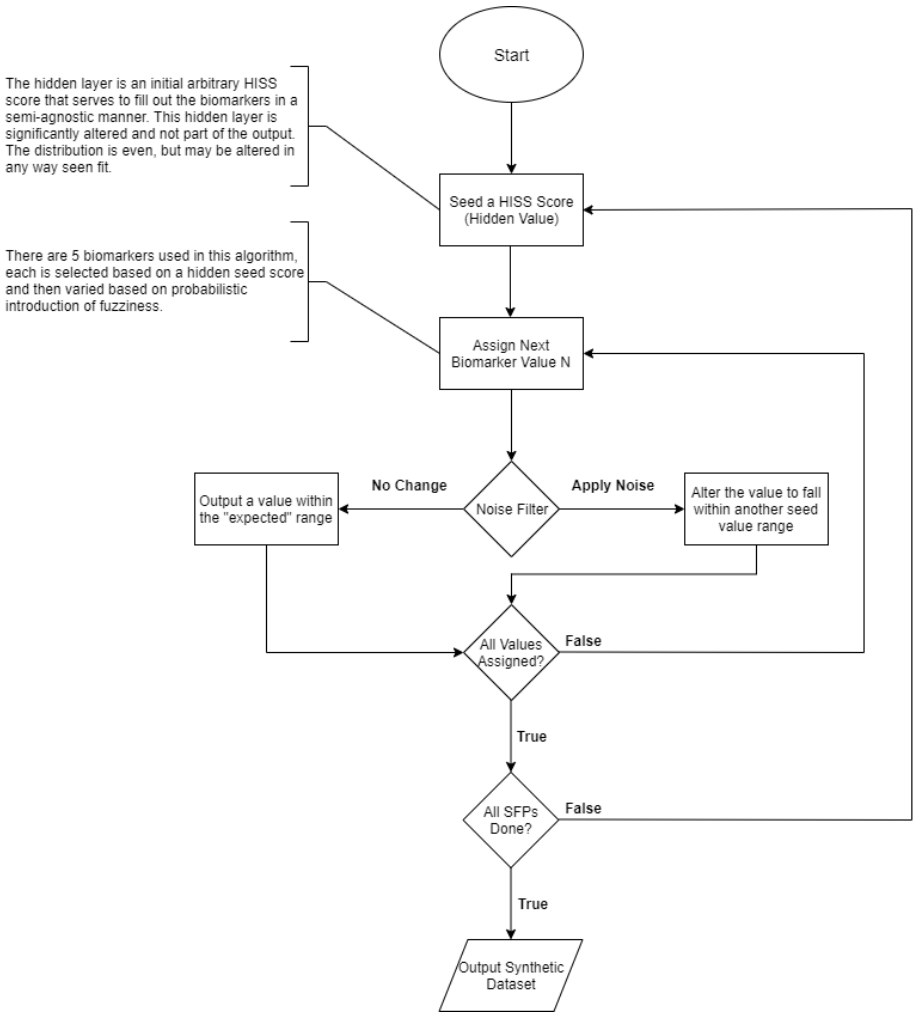

Figure 36. Flowchart for data generation using Sensible Fictitious Rationalized Patient (SFRP) data generator.

The algorithm may be run for any number of synthetic patients to generate SFRP data sets for each. For assessment, the initial hidden layer seeding was not output and was not revealed to any evaluator of the datasets. Potassium was determined via the empirical relationship from Burnell et al. [350], which details that a 0.1 unit drop in pH raises the $[K^+]$ by 0.6 mM. This is implemented in pseudocode in the following way for each output (Eq. 27):

$$[K^+]_i = random([K^+]_{normal}) + (7.35 - pH[i]) * 6 \qquad (27)$$

Where $[K^+]_i$ denotes the potassium of the i^{th} patient, and $pH[i]$ that patient's pH level generated earlier. The random function action yields a normal potassium concentration within physiologic ranges, and is then altered if the pH of the patient displays acidosis via the relation described. This concept is illustrated for the entries shown in bold in **Table 13.**

Table 13. Bounded pathophysiological ranges of key biomarkers of physiological stress in the hemorrhaging trauma patient.

	Pathophysiological range		
Analyte	Low	Normal	High
Glucose	Hypoglycemia <3.88 mM <70 mg/dL	Euglycemia 3.88–5.50 mM 70-99 mg/dL	Hyperglycemia 5.50–10.00 mM 99-180 mg/dL
Lactate	Hypolactatemia < 0.50 mM	Eulactatemia 0.50–1.00 mM	Hyperlactatemia 2.00–4.00 mM
Potassium	Hypokalemia (<3.50 mM)	Eukalemia 3.50-5.50 mM	Hyperkalemia (>5.50 mM)
pH	Acidosis (<7.35)	7.35-7.45	Alkalosis (>7.45)
pO_2	Hypoxia <5.18 mM <100 mmHg	5.18-6.22 mM 100-120 mmHg	Hyperoxia (>6.22 mM) >120 mmHg

In this way a complete set of Sensible Fictitious Rationalized Patient data for *n*+25=100 fictitious avatars (not patients) were created and ported into an excel spreadsheet for expert scoring and fusion considerations. Empirical relationships among the biomarker variables are possible and are being explored to enhance the robustness of the SFRP data sets. **Table 14** shows a possible outcome for generating the training and testing data sets using the SFRP data generator. Accordingly, 100 unique Sensible Fictitious Rationalized Patient (SFRP) data sets were scored by five clinical experts. Each of the five experts assigned a HISS score, valued 0-4,

to each penta-analyte data set while providing a rationale for their selection of the assigned score for a particular patient (0=LOW, 1=GUARDED, 2=ELEVATED, 3=HIGH, 4=SEVERE). This resulted in a multi-class/expert framework [351] for the model-based predictions.

Table 14. Partial data set for "fictitious patients", including training data set (1 to n) and testing data set (n+1 to n+25) generated using the Sensible Fictitious Rationalized Patient (SFRP) data generator and corresponding expert assigned Hemorrhage Intensive Severity and Survivability (HISS) score.

Fictitious Patient	Sensible Fictitious Rationalized Patient (**SFRP**) Data					**HISS**				
	Glucose (mg/dL)	Lactate (mmol/L)	pH	Potassium (mmol/L)	pO_2 (mmHg)	D1	D2	D3	D4	D5
1	70	2.7	7.42	5.10	78	1	1	1	1	0
2	160	6.0	7.11	6.14	44	4	2	3	3	3
n	41	9.7	7.26	4.84	97	3	3	4	3	3
..	..	..	..	..	..	..	..	..	..	..
n+1	123	3.3	7.41	5.00	86	UD	UD	UD	UD	UD
n+2	49	8.7	7.13	5.92	53	UD	UD	UD	UD	UD
..	..	..	..	..	..	..	..	..	..	..
n+25	220	8.6	7.23	4.52	92	UD	UD	UD	UD	UD

5.2.2 Classification algorithms

Data from different sources can be fused via estimation, association and decision fusion [352]. Multi-class [353] ensembled bagged decision tree (EBDT), linear support vector machine (SVM-linear), artificial neural network with Bayesian regularization algorithm (ANN:BR) and possibility rule-based using function approximation (PRBF) classifiers were used to classify the SFRP data sets. **Figure 37** shows the concept for a fused score from the data of the five biomarkers. Five unique data sets, each of size 100, corresponding to the pathophysiological profile of 100 fictitious patients and along with the HISS scores of five healthcare provider

experts: [100][D1], [100][D2], [100][D3] [100][D4] and [100][D5] were thus created from the available 100 penta-biomarker, patient data sets. Testing data comprised 25% of the total data set and the same testing data was used for all algorithms. **Figure 38** is a flowchart that illustrates the generalized approach to classification.

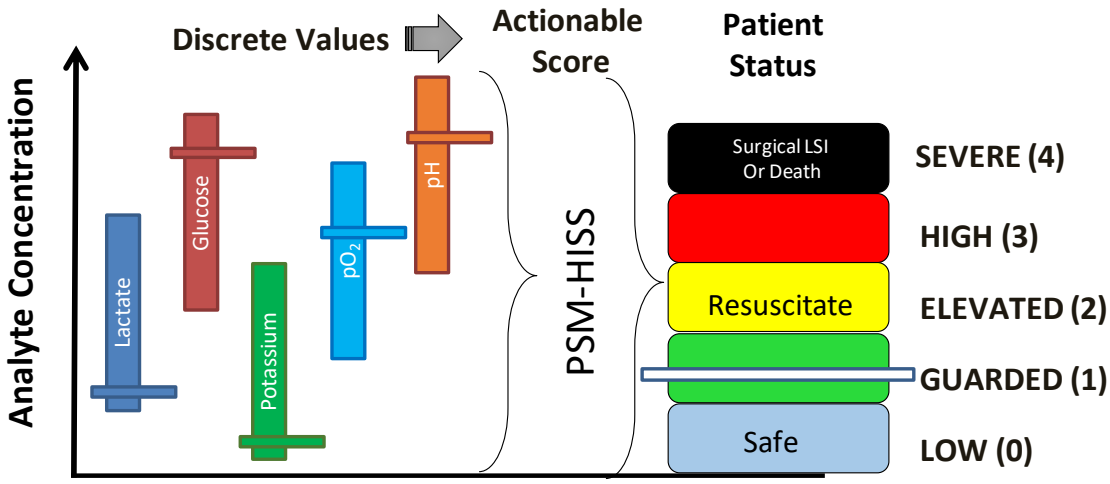

Figure 37. Immediate and continual measurement of key biomarkers may serve as a "gauge" for identifying shock states.

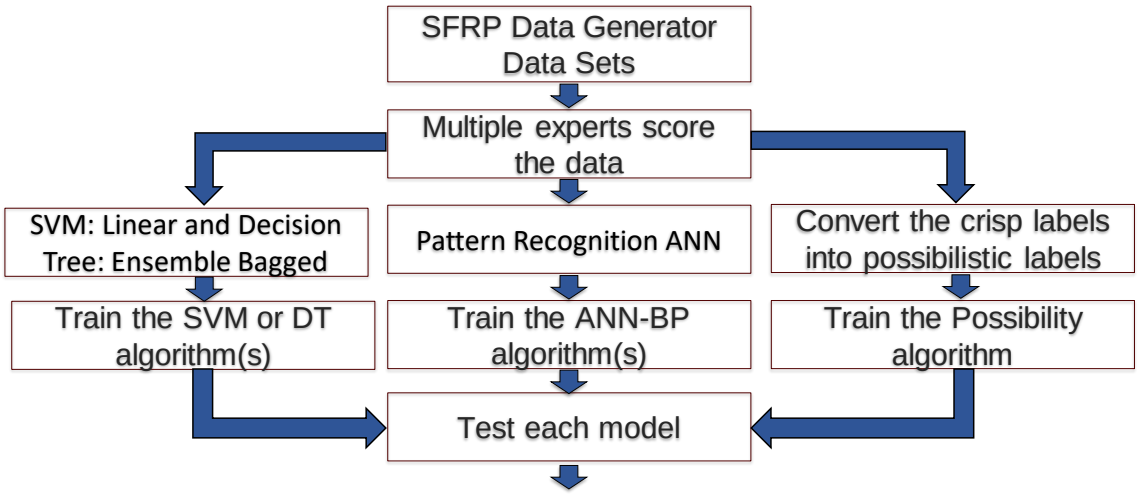

Figure 38. Flowchart illustrating the generalized approach to classification, pattern recognition and possibility analysis that results in an accuracy assessment from the confusion matrix (CM).

The multi-class ensembled bagged decision tree and linear support vector machine classifiers were used for predictions over the entire data sets (D1-D5). Neural networks [354] were used to determine the adequate number of training size for accurate predictions over the five data sets. Possibility rule-based classifers were used to capture the uncertainty in the responses of the experts over the five data sets. Each algorithm was trained and then the same test data set (25%) was used to validate each model. The accuracy was established as the performance metric and was determined from the generated confusion matrix. For all algorithms, the mean test and mean training accuracy were determined by varying the size of the training set between 30 and 80 instances with steps of 5. To test the trained models, a fixed set of instances of size 20 was used. The experiment for each training set size was repeated twenty times to reduce the effect of variance on the results and the mean accuracy was reported. This served as a self-consistent approach across all classifier algorithms. However, each algorithm was also uniquely approached as described following.

5.2.2.1 Multi-class ensembled bagged decision tree and linear support vector machine classifiers

SVM-linear and EBDT were based on the 5-fold, cross-validated classification accuracy. SVM-linear was used as it requires lower computational cost as compared to the non-linear SVM. Additionally, an ensemble technique (bagging) was applied in order to reduce an error of DT, as the combination of several weak predictors into one high-quality ensemble model improves predictive performance[355]. Moreover, classifiers were trained using hyperparameter (maximum number of splits, number of learners, learning rate) optimization by Bayesian optimization and 50 iterations, which allows for minimization of cross-validation loss, and in turn increases the overall accuracy of the predictions. The computations were performed using MATLAB R2019b Classification Learner App run on a PC [355]. The computations were repeated three times and the mean accuracy ± standard deviation were presented.

5.2.2.2 Artificial Neural network with Bayesian regularization algorithm

A Bayesian regularized neural network (ANN:BR) capable of classifying patients using an assigned HISS score was developed in MATLAB 2018a Neural Network Pattern Recognition App run on a PC [356]. The neural network was trained to a max epoch size of 100 using Bayesian regularization algorithm[357] (training stops according to adaptive weight minimization) using Mean-Square Error as the performance metric. Responses from the five (5) experts were used to create a single label by calculating the mathematical mode as the best metric of central tendency. The mode was chosen over the mean due to possible skew in HISS scores. The NN was trained using i) sorted and ii) unsorted data. Sorted data served to ensure that HISS scores were normally distributed among the training and test data. Sorting established

groups of 5 different patient data using the 80:20 rule (e.g. 80% of HISS score "1" was used in the training set, while 20% of HISS score "1" was used in the test set). Unsorted data employed no such grouping and hence carried the risk that the test data could be unbalanced in its representation of certain HISS scores. Neural network performance was measured by using a constant test set size of 25 with 4 or 5-fold cross-validation, where the training set size varied from 15% to 75% of the total data set size. In yet a totally different and additional approach, the mean test and mean training accuracy were determined by varying the size of the training set between 30 and 80 instances with steps of 5. To test the trained models, a fixed set of instances of size 20 was used. The experiment for each training set size was repeated twenty times to reduce the effect of variance on the results and the mean accuracy was reported. This served as a self-consistent approach across all classifier algorithms.

5.2.2.3 Possibility rule-based classifier

The possibility rule-based classifier was implemented using Python 3.7.5 run on a PC. A 5-fold cross-validation was used with population size = 4000, stretch = 25, learning rate = 0.1, and training iterations = 100,000. Having the assigned scores from five expert physicians for the generated SFRP data sets, it is probable that any two physicians might disagree on the score of any one patient's values or the same physician assigns different scores to patient's values that are nearly similar. This problem may be addressed with the use of possibility theory [358], capturing the inherent intra-expert and inter-expert variation in the responses of physicians. More specifically, scores provided by the physicians for each set of measurements, the SFRP data set, were converted into possibility values that were values between 0 and 1. For a given measurement vector $\mathbf{x}$ and a hypothetical class, ω^k, the possibility distribution, $\pi_{\mathbf{x}}$, defined for $\mathbf{x}$

represents the knowledge contribution of an information source about the actual state of **x**. In other words, $\pi_{\mathbf{x}}(\omega) = 0$ means that state ω is rejected as impossible, and $\pi_{\mathbf{x}}(\omega) = 1$ means that state ω is totally possible (plausible). In a machine learning framework, this concept is employed to solve classification problems by taking $\pi_{\mathbf{x}}$ to represent the degree of belonging of SFRP data to classes which are provided by the expert(s) [349].

PRBF has two main mechanisms to generate a problem solution; a rule-based evolutionary algorithm to approximate possibility labels, and an information fusion method to make plausible inferences for unseen data. When trained on a dataset with possibility labels, PRBF iteratively evolves a population of overlapping rules which are piece-wise linear approximations of the target possibility distributions. Moreover, the data fusion technique employed in PRBF combines the data provided by multiple sources, i.e., rules of the model, and calculates the most plausible values for the class membership of the unseen data set. Consequently, for an unseen patient data set, the model generates a possibility distribution (π). This distribution may then either be interpreted by an expert for decision-making purposes or processed to extract a crisp class by taking the one with the highest possibility. To demonstrate the benefit of employing a model that is robust in the presence of HISS score uncertainty, the same training data that were generated using SFRP data generator were used to train the PRBF algorithm and the trained model was evaluated against the 100 instances used in the previous sections for the model evaluation. The disagreement among the physicians' evaluations, was captured by repeating the process for all of the 100 SFRP samples by calculating a set of possibility labels as well as a class label based on the majority vote.

5.2.2.4 Performance metric, cross-validation, adequacy of patient data size and predicted patient data size with the number of experts

In general, the performance of a multi-class classification can be measured using accuracy, precision and F–score [359]. A confusion matrix plot can be used to evaluate the quality of the classifier [360]. The matrix contains values corresponding to true labels and predicted labels. The values in the major diagonal of the confusion matrix can determine how well the classifier has performed. In this work accuracy was used as a performance metric to report the prediction performances, which can be obtained from the major diagonal elements of a confusion matrix as follows (Eq. 28),

$$Accuracy = \frac{\#\ Correct\ predictions}{\#\ predictions} = \frac{\Sigma\ of\ elements\ in\ the\ major\ diagonal}{\#\ of\ elements} \qquad (28)$$

Cross-validation [361] [362] helps with using all the available data for model training and hence in making more robust predictions. To do so, the data were randomly split into equal sets for training of multiple models. Here a 5-fold cross-validation [363] was used. The adequacy for the patient data size was tested with the minimal point for stabilizing validation accuracy. The adequacy for the number of experts and the prediction for the patient data size for a test accuracy of 0.99 and 0.999 with the predicted number of experts necessary to achieve that accuracy was arrived at using the regression model fit and application of predictive modeling in JMP Pro software version 14.0 run on a PC.

5.2.2.5 Comparison of classification algorithms

The classification algorithms employed in the previous sections were compared for their respective accuracies. To train each model, 5-fold cross-validation was employed and the average test accuracies along with the standard deviation of the accuracies was reported. To train

the PRBF algorithm, the uncertain labels (u) were used and the other classification algorithms were trained on D1-D5 and using the majority vote of the labels obtained from the five physician experts.

For each classification model, a set of hyper-parameters was tuned and the model with the highest test accuracy was chosen to be reported. For ANN:BR, the number of nodes was selected from [5, 60] with step 5. Different activation functions were tested and a ‘tanh’ function was selected. The solver that was used to train the models was the 'adam' solver and the model was trained for 100,000 iterations. For the random forest model, the maximum depth of each tree was selected from [1, 7] and the number of trees was selected from [10, 150] with step 10. The entropy was employed as the selection criterion at each node. A similar strategy was used for the decision tree algorithm wherein the maximum depth was selected from [1, 5]. Moreover, for the bagged decision tree algorithm the number of estimators was selected from [6, 20] with step 2. For the SVM model, different kernel functions (linear, polynomial, radial base function, and sigmoid) were tested. In the case of the polynomial kernel, the degree of the polynomial was selected from [2, 6]. Finally, for the PRBF model, the maximum number of rules was selected from {500, 1000, 3000, 4000, 5000, 6000}. The maximum condition stretch was selected from [317 20, 25, 30, 35] which modifies the proportional size of the rule condition and effects the accuracy of the rules. The learning rate was set to 0.1, and the number of training iterations was 30,000.

For the decision tree classifiers, support vector machine and the neural network, their Python implementation that was available in Scikit-learn [364] library was used. For the PRBF algorithm, its implementation in Java was used. All experiments were carried out on a 2.70 GHz Windows 10 machine with a 16.0 GB RAM. One -way Analysis of Variance (ANOVA) was

used to determine the significance levels for the performance of these algorithms using JMP Pro software version 14.0 run on a PC.

5.3 Results

5.3.1 Classification via Ensembled bagged decision tree and linear support vector machine

Two well-established classifier algorithms, namely Decision Tree (DT) and Support Vector Machine (SVM-linear), were used in the classification of SFRP data. **Figure 39A and 39B** provide the accuracy versus the number of training samples for DT:EB and SVM:L. **Table 15** presents the findings of the DT:EB and SVM:L classifiers in terms of their validation accuracy.

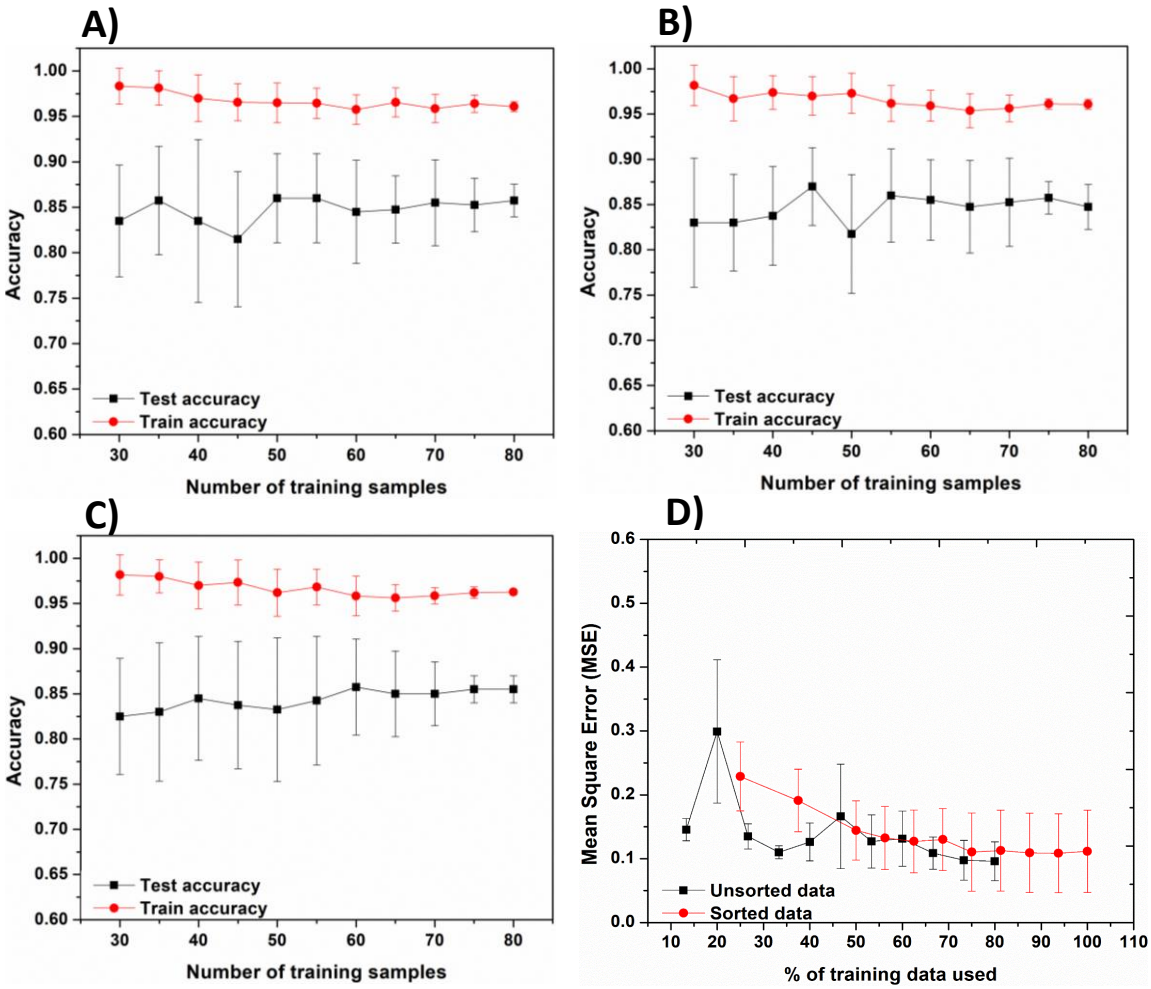

Figure 39. Evaluation of the mean test and mean train accuracy versus the number of training samples for the training size varied from 30-80 in steps of 5.

Table 15. Application of two different algorithms (SVM: Linear and Decision Tree: Ensemble Bagged) to the five (5) unique SFRP data sets; [100][D1], [100][D2], [100][D3], [100][D4] and [100][D5].

Class	Frequency [%]				
	D1	D2	D3	D4	D5
0	56	43	37	43	53
1	14	20	27	18	17
2	5	18	7	15	13
3	19	17	11	24	17
4	6	2	18	0*	0*
SVM-L accuracy [%]	78.3±0.5	92.7±0.5	78.3±2.4	88.3±0.5	86.7±0.9
EBDT accuracy [%]	83.3±1.2	96.3±0.9	72.3±0.9	90.0±0.0	87.7±1.2
Class with the highest confusion (TPR – sensitivity for EBDT)	4 (17%)	4 (0%)	2 (14%)	2 (60%)	2 (77%)

Analysis of each experts' model individually, revealed that DT:EB generally performs better than SVM:L (**Table 15**). Although the differences between both predictors for each dataset were slight (in the range of 2-6%), when it comes to patient stratification decisions, small improvements may be consequential to the therapeutic intervention for a patient. The highest cross-validated accuracy was achieved for the expert D2 dataset and the DT:EB classifier (96.3±0.9%). However, a confusion matrix revealed that D2 failed completely to predict Class 4 (Severe), as 100% of labels were misclassified. Among all experts, the highest confusion (TPR) occurred for Class 2 (Elevated), which was the most frequently misclassified as either Class 1 (Guarded) or 3 (High) and for Class 4 (Severe) misclassified as Class 3 (High). There was no single instance where all the five experts concurred on the score of 2. This is due to the fact that 2 is a score in the mid-range of 0-4 and hence higher variability for this score was introduced compared to the extremities [365]. As shown in **Table 15**, a high level of misclassification may

result from an imbalanced number of instances in each class. For example, for expert D1, only 6 instances out of 100 were labeled with Class 4 (Severe), which leads to only 17% TPR. For D3, only two data rows were labeled as Class 4 (Severe), which caused complete misclassification of this score (0% TPR). While for D4 and D5, despite the high performance, none of the input instances were scored as Class 4 (Severe), leading to a model which will fail to make predictions of this class for the new data. Bagging classifiers may reduce the misclassification rate and improve overall accuracy of algorithms. Thus, the DT:EB classifier, while being more time-consuming, performed with high accuracy compared to the SVM:L. However, the support vector machine classifiers had a higher accuracy for the data set D3 whereas the decision tree algorithm was less effective in capturing the localized accuracy of D3. From the literature, accuracies of 83-88% for SVM [366], and accuracies of 70-83% have been reported for decision trees in medical applications [367].

5.3.2 Classification via artificial neural network classifier

With a constant size of 25 validation data sets, it was observed that the error increased with increase of the SFRP training data sets (**Figure 40**). From the literature, it is known that the error should have stabilized or be shown a decrease to some extent with increasing training data sets [368]. This was attributed to the difference in the opinions of the experts. Consequently, a sliding window of validation data sets was used. Using the approach of Mode to allow the doctors to vote together along with a sliding window of validation data sets showed a decrease in error with an increase in the training data sets, in agreement with the literature as shown in **Figure 39D** [369]. Here it was observed that sorting improved output quality with a smooth

trend towards equilibrium or limiting error. However, the unsorted data appeared chaotic with stochastic noise.

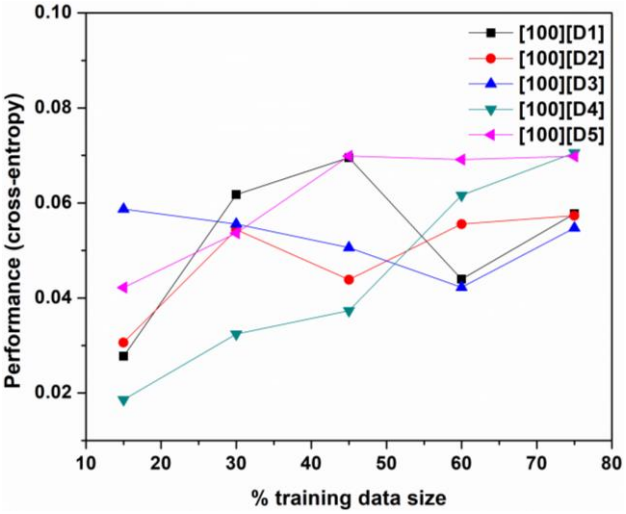

Figure 40. Evaluation of the influence of the size of the training set, expressed as a % of available data, on the performance of the ANN-BR as expressed in the cross–entropy for constant epochs of 100.

Unsorted data at a very low training set size (15-20%) showed a very high standard deviation of MSE due to a lack of heterogeneity within the training set. The probability of less frequently available HISS scores, such as 4, being withheld from the training set was very high. For example, at a training set size of 20%, the probability of a HISS Score of 4 showing up in the training set was 0.008. Unsorted data tended to the same MSE as sorted data (~0.12), but was variable in its descent due to probabilities of scores not being included in the training set because if low frequency (e.g. HISS Score 4). As shown in **Figure 39D**, improvement in the test accuracy of the ANN:BR was insignificant for the number of SFRP training samples larger than 75. Based on **Figure 39C and 39D,** 75 SFRP data sets were established to be an adequate data size to build a model for prediction. From the literature, prediction accuracies of 44% and training accuracies of 50% and above have been reported for neural networks in medical applications [370] [371].

When the accuracies were on a lower side, the neural network approaches were often combined with hybrid fuzzy systems [372].

5.3.3 Performance of PRBF

One simple way to resolve conflict among class evaluations from multiple experts is to take the class label that was most frequently identified. An alternative approach, which makes better use of the rich data provided by the experts, is to calculate a set of possibility labels using equation (4), which is expected to reflect the disagreement among experts better than solely taking the majority vote. **Figure 41A** depict the 5-fold training and validation accuracies. For the sample presented in **Figure 41B**, the majority vote opts for class zero to represent the patient's status, as shown in **Table 15**. The possibility labels calculated using the equation (4) for the same patient data are provided in column 'Uncertain labels' in **Figure 41B**. The uncertain labels assume the association of the patient data to class zero and one. The degree of possibility that the sample belongs to each class is different however and is equal to 1 and 0.5 for class zero and one, respectively. This graded association reflects the disagreement among the experts in deciding the true status of the patient.

A confusion matrix plot was used to represent the performance of the possibility rule-based classifier using function approximation (PRBF) [360]. The matrix contains values corresponding to true labels and predicted labels. The values in the major diagonal of the confusion matrix serve to determine how well the classifier has performed. Folds indicate the division of the data set to confirm that each of the folds has been used as a set. Uncertainty or error information has been utilized to support medical diagnostics where a prediction accuracy of 87% has been reported for a training accuracy of 90% [373]. Common approaches like

possibility rule-based classification for handling error include fuzzy probabilities [374], and hybrid fuzzy-NN systems [375].

A)

	Training accuracy	**Test accuracy**
Fold-1	0.950	0.90
Fold-2	0.963	0.90
Fold-3	0.975	0.95
Fold-4	0.950	0.95
Fold-5	0.938	0.90
Mean accuracy	0.955	0.92
Standard deviation	±0.014	±0.03

B)

Fictitious Patient	**Majority vote**	**Uncertain label (u)**	**PRBF prediction (π)**
72	0	[1,0.5,0,0,0]	[0.979,0.321,0,0,0]

Figure 41. A) Cross-validation model training results for PRBF algorithm for Population size = 4000, stretch = 25, learning rate = 0.1, and training iterations = 100,000, B) True labels and predicted uncertain labels for the tested SFRP sample of fictitious patient number 72.

The PRBF model was able to predict HISS scores with 92% accuracy for a testing and training accuracy of 96%. These results confirm that the idea of integrating evaluations from multiple experts and modeling them with a proper uncertainty handling tool, which is possibility theory in this work is beneficial for decision making. Note that by increasing the number of training samples of the SFRP data sets, the model will be better trained and able to produce more accurate predictions.

5.3.4 Comparison of the test accuracies of classification algorithms

The performance of the four classification algorithms, ensemble bagged decision tree (EBDT), linear support vector machine (SVM-linear), artificial neural network with Bayesian regularization algorithm (ANN:BR) and possibility rule-based using function approximation (PRBF) were compared for their ability to accurately classify the SFRP data sets. **Figure 42A** lists the test accuracies and **Figure 42B** shows the misclassification rates for the classification algorithms and the uncertainty labels of PRBF algorithm for different experts and the majority vote. The highest accuracy is highlighted in bold for each algorithm. EBDT, SVM-linear, ANN:BR and PRBF generated score predictions with testing accuracies corresponding to 93%, 91%, 92%, and 92%, respectively, with no statistically significant difference ($p>0.05$) in their means for ±95% confidence interval (C.I).

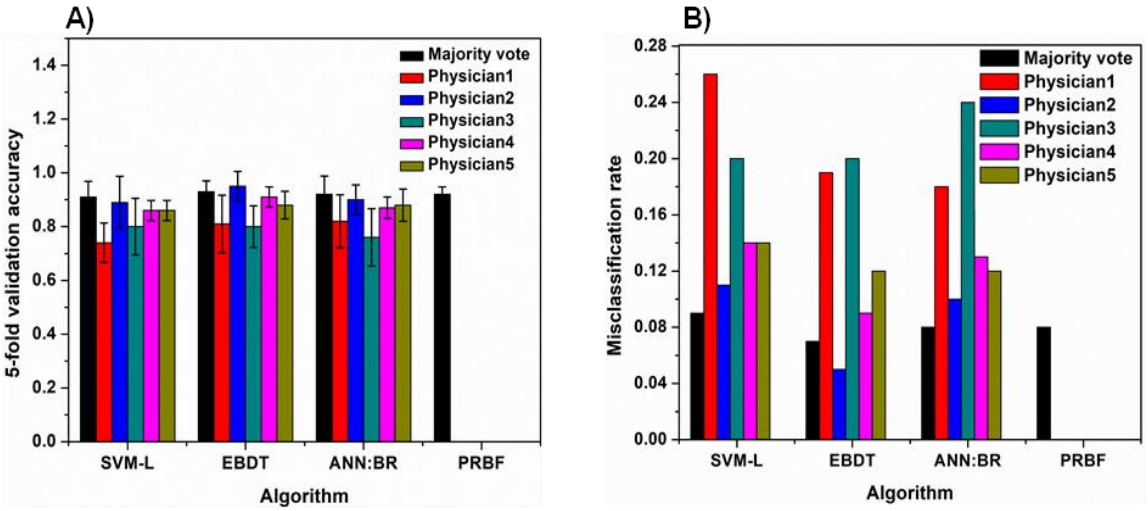

Figure 42. A) Comparison of test accuracies and B) Misclassification rates of EBDT, SVM-L, and ANN:BR along with the uncertainty labels of PRBF algorithms for experts D1-D5 as well as the majority vote.

5.3.5 Predictions for the adequacy of the patient data size and number of experts for improved accuracy

It is reasonable to ask, given the scoring accuracies obtained for the 100 patients and 5 physician experts 100[5], what data set size and how many experts will be required to improve scoring accuracies? Targeted accuracies of 99% and 99.9% could be achieved with SFRP data size and clinical expert scores of 147[7](99%) and 154[9](99.9%), respectively. The model fit for 99% was for a R^2=0.96 with the Total Sum of Squares (SS_{total}) as 0.04 with a statistical significance of $p \leq 0.05$ for a ±95% confidence interval (C.I). The model fit for 99.9% was for a R^2=0.89 with the Total Sum of Squares (SS_{total}) as 0.11 with a statistical significance of $p \leq 0.05$ for a ±95% confidence interval (C.I).

5.4 Discussion

5.4.1 Evaluation of individual classifiers

The collection, labeling and archiving of medical data is usually time-consuming, expensive and fraught with security concerns, appropriately so [376], [362]. Therefore, it is a challenge to build predictive models based on limited available training data. Moreover, the labels are often provided by multiple experts, who may have different opinions about the same patient's health status. Such disagreement may result from differences in experts' knowledge and clinical experience. As a worst-case scenario, differences in opinions may lead to patient misclassification [377], which may have serious consequences to their health [378]. The goal of the present study was to produce and use 100 instances of Sensible Fictitious Rationalized Patient data in the development of predictive models for patient stratification, to use expert

opinion to achieve the same stratification in order to ground truth the predictive models and to engage cognizance of intra-expert consistency and inter-expert variability. The study revealed that the more imbalanced the input data, the higher the misclassification penalty. The similarity in misclassification (high level of misclassification of Scores 2 and 4) for each dataset and for both DT:EB and SVM:L classifiers, may be the result of insufficient information provided to perform reliable labeling. It is, therefore, extremely important to compare various classifiers in terms of not only their accuracy but also their level of misclassification.

5.4.2 Qualitative evaluation of experts' HISS scoring

As a pilot study, the opinions of five experts, D1– D5, were obtained. Expert 1 based his bias weighing decisions on the abnormal levels of biomarkers, being driven by the extremes. For example, when the lactate levels were high, with potassium elevated but compensated, but with a normal pH, this produced a HISS score of 1. It is observed that a score of 2 was assigned when the lactate level does not correlate with other values (normal pH, Eukalemia, Euoxia). High lactate, very low glucose, low pH and normal oxygen produced a HISS score of 3. All values very deranged with pH almost out of physiologic non-recoverable range; hypoxia below 60, elevated lactate, potassium elevated suggesting cell injury, resulted in a HISS score of 4. While providing the scores, expert 2 was able to pick the ones that were similar. Hence, his scores were consistent across all different profiles. The scoring pattern of expert 3 was not localised. Expert 4 localised his scores from 0-3. While this paper is not concerned with expert performance, and the data set was far too small to allow the analysis of experts, the very low intra-expert variablity (8.0%) and larger inter-expert variability (20.6%) is worthy of mention.

5.4.3 Comparison of classifiers in terms of cross-validation accuracy

By the majority vote, SVM-L, EBDT, ANN:BR, and PRBF had cross-validated accuracies of 0.91±0.06, 0.93±0.04, 0.92 ±0.07, and 0.92±0.03 respectively. The results for EBDT, SVM-L, and ANN:BR were statistically significant. The misclassification is more prominent among the middle classes of 2 and 3. For example from **Figure 43**, misclassification rates were 71% for the class of 2 for SVM-L This is because the experts converge upon the extreme values but may have an overlap in the middle classes. Ensemble bagged decision tree (EBDT) and linear support vector machine (SVM-L) classifiers provided for classification in a simple hierarchy of a tree structure and SVM-L provided robust classification. An unquestionable advantage of the presented decision tree classifiers is that they are simple and rapid prediction tools which establishes the trauma severity score with a high accuracy. The results showed that the decision tree classifiers constitute a reasonable basis for the further extensive studies on more specific and complex prediction approaches which may overcome the limitations of the current methods such as a lack of external validation of the model, experts' opinion, or variation.

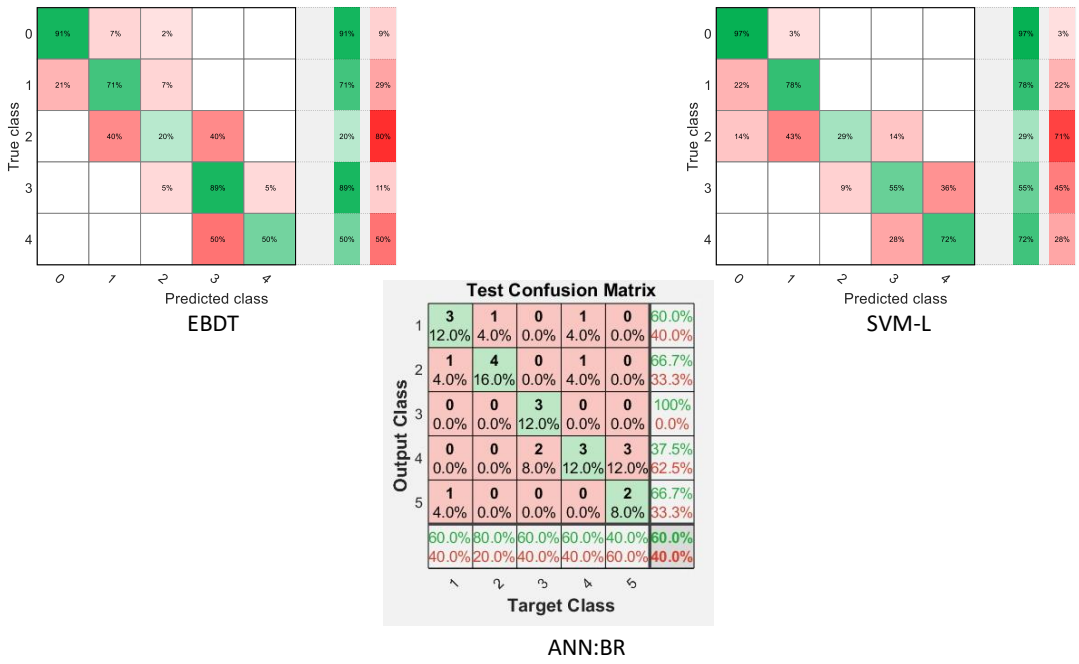

Figure 43. Representative confusion matrices for EBDT, SVM-L, ANN:BR.

5.4.3.1 Artificial Neural network with Bayesian regularization algorithm

ANN:BR has the advantage of tuning the incoming patient data sets. The term epoch in ANN is defined as the measure of the number of times all of the training vectors were used to update the weights [379]. The softmax activation function was used to introduce non-linearity into the model. The inputs were turned into a linear model (ωx+b), where ωx is the matrix multiplication of weights (ω) and inputs (x) and b is the bias. The scores obtained from this step were fed into the softmax function (equation 3) which converts them into probabilities (Eq. 29).

$$\sigma(z)_j = \frac{e^{z_j}}{\sum_{k=1}^{K} e^{z_k}} \; for\; j = 1, 2 \ldots, k \qquad (29)$$

Softmax function maps the set of outputs onto inputs. In this case, there are five outputs which when passed through the softmax function get distributed according to probability (0,1). This was useful for finding the most probable occurrence or classification for a particular output.

5.4.3.2 Performance of PRBF relative to other classifiers

In the possibility rule-based classifier system using function approximation (PRBF) [358], possibility theory is used to handle uncertainty in expert knowledge. The degree of belonging of an instance to the k^{th} class may be characterized by $u^k \in [0,1]$. Different theoretical frameworks have been proposed to solve problems that suffer from uncertainty [380] including probability theory, set theoretic functions, and possibility theory. Under the possibility theory [358], [381] framework, $u^k$is the level of possibility that the given data point belongs to the class of score k and the following representation holds for the set of possibilistic classes assigned to the i^{th} instance (Eq. 30):

$$\boldsymbol{u}_i = (u_i^1, u_i^2, \ldots, u_i^c)\ \forall u_i^k \in [0,1] \qquad (30)$$

In Equation (4), c is the number of scores defined for the problem, i.e. in this case five scores, being LOW (0), GUARDED (1), ELEVATED (2), HIGH (3), SEVERE (4). Unlike the probabilistic labels, the values of the vector $\boldsymbol{u}_i$ do not have to sum up to unity. Instead, each parameter takes a value ranging from 0 to 1. The classification scheme proposed by Nazmi and Homaifar [358], namely, possibility rule-based classifier using function approximation (PRBF), employs this definition of a class assignment and trains a rule-based evolutionary model that given a data point, predicts the degree of possibility to which the SFRP data set belongs to each of the possible classes.

The PRBF classifier added a layer to the intra- and inter- expert variabilities addressed by the other classifiers by tapping into the votes (either majority or individual) of the experts for a particular patient data set and reporting the number of times a physician's label agrees with the consensus. It was interesting to note that expert 4 had the highest concurrence from his scoring

pattern localized for 0-3. This coincides with real-life scenarios when expert physicians try to categorize the patients from 0-3 and try to save them. Comparatively, the score of 4 corresponding to severe was rare. From the 5-fold cross-validation results, the improvement in the test accuracy is insignificant for the number of training samples larger than 70. The increase in the training samples from 30% to 70% improved the accuracy from 71% to 78.5%.

The PRBF model seeks to incorporate the inherent disagreement among the physician experts into the model training procedure. According to **Figure 42A**, integrating evaluations from multiple physicians through the possibility theory resulted in a better performance than EBDT, SVM-L, ANN:BR, and PBRF trained using the majority vote. This implies that employing different tools of modeling the uncertainty, allows for capturing different forms of uncertainty and potentially leads to better prediction accuracy. Moreover, training a model using PRBF allows for an additional level of interpretation of the model prediction during the decision-making process. To illustrate this point, consider the example of Fictitious Patient 72 presented in **Figure 41B**. When the trained PRBF model was elicited for predicting a label for this sample, it was able to correctly predict association to both classes with different degrees of belonging, as shown in **Figure 41B**. For each test sample, the PRBF model provides a degree of possibility to belong to each class. The possibility values can be used to gain more insight into the prediction process of the model and provides the decision-maker with more information about the potentially over-lapping classes. **Figure 42B** shows the misclassification rates for than EBDT, SVM-L, ANN:BR, and PBRF. PRBF has the least misclassification rates. As per the majority vote, SVM-L seems to have high misclassification followed by ANN:BR and then the EBDT. Representative confusion matrices have been shown in **Figure 43**.

5.4.4 Prediction for an adequate patient data size and predicted patient data size with the number of experts

An adequate testing patient data size of 75 was found beyond which the Mean Square Error and the validation accuracy were both stabilized for ANN:BR. This therefore establishes the minimum patient data set needed to conduct predictive patient classification. The present patient data size of 100 and five scoring experts produced accuracies of 0.93. The patient data size needed to obtain an improved accuracy of 0.99 was predicted to be 147 with the predicted number of 7 experts. Similarly, for an accuracy of 0.999, the predicted size of the number of patient data was 154 with 9 scoring experts. From the model, R^2 was 0.96, with the Total Sum or Squares (SS_{total}) as 0.04 with $p \leq 0.05$ for a ±95% confidence interval (C.I). Increasing the number of scoring experts from 5 to 7 can yield an accuracy of 99% but necessitates an increase in patient data set size from 100 to 147 (R^2=0.96). Likewise, increasing the number of scoring experts from 5 to 9 can yield an accuracy of 99.9% but necessitates an increase in patient data set size from 100 to 154 (R^2=0.89). There is less certainty in the prediction in going from 99 to 99.9 % because of the limitations of the resent data set.

5.4.5 Improvements to the existing model-based on a substantial number of experts

This is a preliminary evaluation of the multiple approaches for the fusion of discrete patient sensor data into an actionable HISS score. Hence, the model-based predictions along with the evaluations of the experts' opinions form a baseline and serve as a precursor to a larger study for which the following improvement strategies can be implemented:

Number of experts: The current study uses five experts, D1-D5, with 100 SFRP data sets. The robustness of the probability theory and capacity to ascertain and account for physician variance was tested by means of uncertainty in the experts' opinions. From the results, it is

observed that the self-consistency in the scoring of 4 experts can overcome the scoring inconsistency of 1 expert. Hence, a ratio of 4:1 is suggested for the number of experts. This aids in substantiating the robustness of the machine learning approaches to ascribe an accurate and actionable HISS score despite the presence of inter-physician variance. An alternative is working with the available number of experts (5) and tuning by increasing one expert at a time to check the limit beyond which the accuracy does not improve any further but stabilizes.

The confidence level of expert scores: It is believed that experts assign the patients to a particular class with a certain confidence level, in this case, 100%. However, they can be requested to reveal their confidence level in scoring each patient. Alternatively, the statistical confidence can be extracted by capturing the variability in the responses of the physicians using approaches like ANOVA. This could be implemented for a substantial number of experts (e.g. 100).

The relative weights of each patient attribute: In arriving at the class assignment, the expert physician reviews the five relevant physiological attributes. In its implementation, the classifier algorithms accept a single score with the assumption that each attribute is equally weighted in that decision-making assignment by the expert. In reality, experts inherently weigh each attribute and the weight is often influenced by that value and the values of other attributes. Based on their experience, the expert physician may treat certain biomarker attributes as being more or less important/influential than others when assigning the patient to the selected class. This can be extended for a substantial number of experts (e.g. 100), where a methodology can be developed to extract the relative weighting of each attribute. This relative weighting is thus a global factor assigned to the attribute. From the multiple expert physician responses obtained, a statistical assessment of the significance of each attribute can be determined. Techniques such as

"leave one out analysis" and ANOVA will allow the extraction of the relative sensitivity of each attribute to the class assignment.

Temporal variation in HISS scores: In the present implementation, SFRP data were presented to each classifier algorithm as STAT data. However, patients are known to display temporal changes or trends in these biomarker values during hemorrhage progression such as during evacuation from theatre to the Green Zone. There is increasing attention being given to the diagnostic relevance of trend data in patient stratification.

5.5 Conclusions

In this study, the Sensible Fictitious Rationalized Patient (SFRP) synthetic data generator was introduced for hemorrhaging trauma patients wherein five biomarkers; glucose, lactate, pH, potassium, and oxygen tension, served as the basis for an actionable HISS score rendered by four experts. Several classification algorithms; ensembled bagged decision tree (EBDT), linear support vector machine (SVM-linear), artificial neural network with Bayesian Regularization algorithm (ANN:BR) and possibility rule-based using function approximation (PRBF) were evaluated for their ability to accurately classify the 100 entries of the SFRP data set. These data-driven predictions are presented as an adjunct to help the decision-making of physicians regarding the status of the hemorrhaging patient during triage and uses a severity scale of (0=LOW, 1=GUARDED, 2=ELEVATED, 3=HIGH, 4=SEVERE). A training data set size of 75 has been identified as adequate to achieve the best performance by minimizing the Mean Square Error. This approach has the advantage of high validation accuracies from the ensembled bagged decision trees and linear support vector machines (93% and 91%) with the tunability of neural networks (92%), and the ability to capture the uncertainty in the responses of experts with the

help of a possibility theory-based approach (92%). The predictions generated using the classification methods would assist in an adjunct device in the form of a biosensor system for point-of-care monitoring of the trauma patient, especially in mass casualty situations. Improvement strategies are discussed with an increase in the number of experts to 100 scoring the SFRP data sets. This paper has a clinical utility in terms of classification by grouping data, prediction for incoming data and regression by means of prediction of continuous data. The predicted patient data size to obtain a test accuracy of 0.99 has been identified to be 147 with a predicted number of 7 experts.

Refined prediction model disclosed a predicted patient data size of 154 with a predicted number of 9 experts for a test accuracy of 0.999. Similarly, the adequacy of the patient data size has been identified to be 75 and of the number of experts has been noted as 5 to allow training and validation.

CHAPTER VI

SUMMARY AND FUTURE WORK

In this body of work, the development of a biocompatible, multi-analyte biotransducer and associated instrumentation that serves as a minimally invasive implantable biosensor system to improve patient stratification, guide resuscitation and monitor the stabilization of hemorrhaging trauma patients is addressed. Focus is given on the pH-responsive element of the multi-analyte biotransducer, with sensing elements for glucose, lactate, pH, potassium and partial pressure of oxygen (pO_2). A pH-responsive hydrogel for the measurement of acidosis under physiological conditions was synthesized from poly(2-hydroxyethyl methacrylate-co-poly(ethylene glycol) methacrylate)-based hydrogels that were molecularly engineered with AEMA and DMAEMA and surveyed for the distribution of water states within the hydrogel. It was found that bound water, not total hydration, correlated strongly with the biotechnical properties, determined the membrane resistance and thereby the pH sensitivity of hydrogels. Surface modification of electrodes was accomplished using polypyrrole and bioactive hydrogels to reduce the charge transfer resistance for ABIO-BIO interface engineering. Using multiplexed biomarker inputs and physician expert scoring, a Hemorrhage Intensive Severity and Survivability (HISS) score was obtained from a fusion of input data and could correlate to survivability using data-driven prediction models. For real-time monitoring, this biotransducer was interfaced externally with hardware components including front-end electronics and a display readout. This microsystem will be used as an intramuscular indicator for the pathophysiology of hemorrhage. Future work for the implementation of the biotransducer entails microlithographic fabrication of a penta-analyte, electroanalytical biotransducer for physiological status monitoring.

6.1 Microdisc Electrode Array (MDEA) and instrumentation assembly, validation and demonstration

For the dual biotransducer with glucose and lactate sensing regions, MDEA 5037[382, 383] was fabricated and packaged. Stop-off lacquer (Microshield, Tolber Chemical Division. Hope. Arkansas) was painted on the two sensing regions to protect them during packaging. The packaging consisted of soldering the MDEA chip to the lead connector using adhesive and encapsulant epoxy FP4323 (Henkel Adhesives, Rocky Hill, CT) to prevent it from being vulnerable to solvents. After packaging, the MDEA dual sensing regions were characterized using multiple scan rate cyclic voltammetry (MSCRV) in 50 mM Ferri/50 mM Ferro cyanide solution in 0.1 M PBS. **Figure 44A and 44C** show the layout and instrumentation assembly for MDEA 5037 dual-analyte sensor. **Figure 44B** shows the symmetrical voltammograms from the upper sensing region of MDEA 5037.

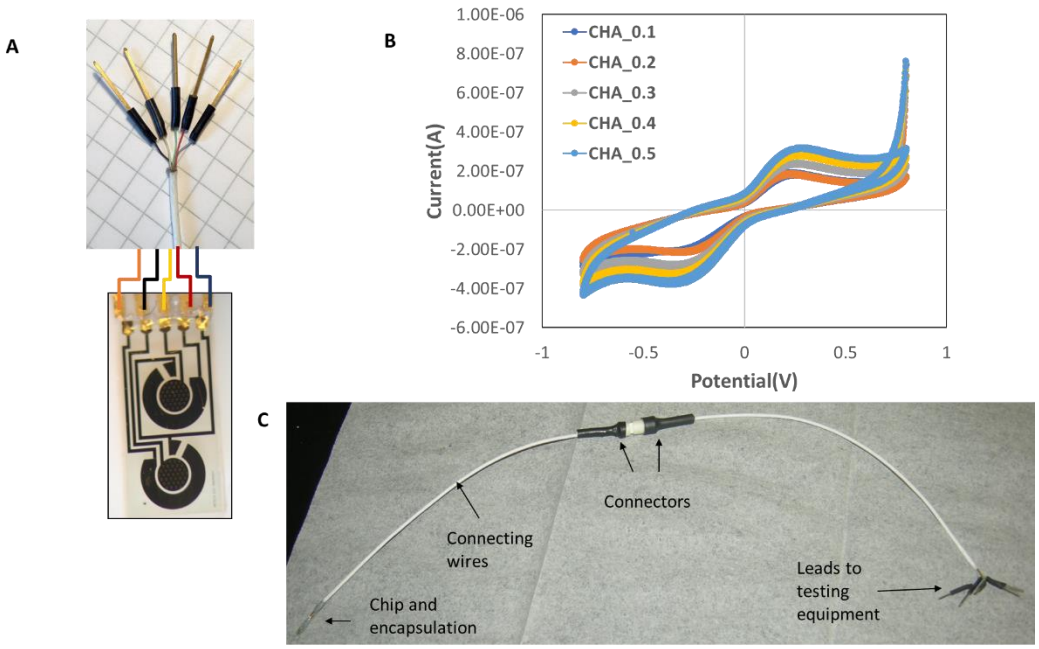

Figure 44. A) MDEA 5037 and the soldered lead connector, B) Cyclic voltammograms for 10 mV/s, 20 mV/s, 30 mV/s, 40 mV/s and 50 mV/s, C) Instrumentation assembly for MDEA 5037 containing MDEA dual-analyte sensor, connecting wires, connectors, and lead going to instrument.

6.2 Hardware sensor to support the penta-analyte, electroanalytical biotransducer for physiological status monitoring

A support hardware sensor along with a penta-analyte biochip can help to gather, process and store the exorbitant data generated by the biosonde for trauma management.

The scope of this work is the design of prototype hardware components involved in an implantable biosensor microsystem for the measurement of analytes relevant to the pathophysiology of hemorrhage. The hardware components of a biosensor microsystem can include the biotransducers, front-end electronics such as potentiostat, AD/DA, medical frequency wireless telemetry, base stations, remote computer, and display readout. Important considerations for hardware design include data collection (current, potential, etc.), information transfer,

security, signal processing, storage, device footprint, portability, and user friendliness. Hardware must be able to securely collect raw data from the biotransducers, in this case five separate biotransducers for five separate analytes, and transmit that to a computer processing station, temper and interpret the collected data, and display actionable data to the end user.

Measuring, recording and transmitting real time physiological measurements is important and plays a crucial role when responding to the etiology and pathophysiology of many diseases [110]. Thus, this project is oriented to the design of externalized hardware that enables the intramuscular measurement, capture, processing, and transmission of bioanalytical data of five implanted biosensors relevant in the resuscitative response to hemorrhage. The five biosensors used measure glucose (amperometry), lactate (amperometry), potassium (K^+) (potentiometry), pH (impedimetry), and pO_2 (voltammetry). The project has the goal of monitoring the levels of each biomarker via an integrated set of dedicated biotransducers formed into a sonde and applied during a case of hemorrhage. The injury caused by hemorrhage are lactate levels rise, and post-traumatic injury also includes hyperglycemia.

The system constraints for the externalized hardware system to support the penta-analyte biochip include portability, a battery life of 5 days, footprint of 2.1 cm x 5.1 cm, and an Intelligent Power Management (IPM) of 174 μs. Bluetooth Low Energy (BLE) mode would be selected as against other modalities like Bluetooth/Zigbee, BLE conserves energy and is more suited for power management.

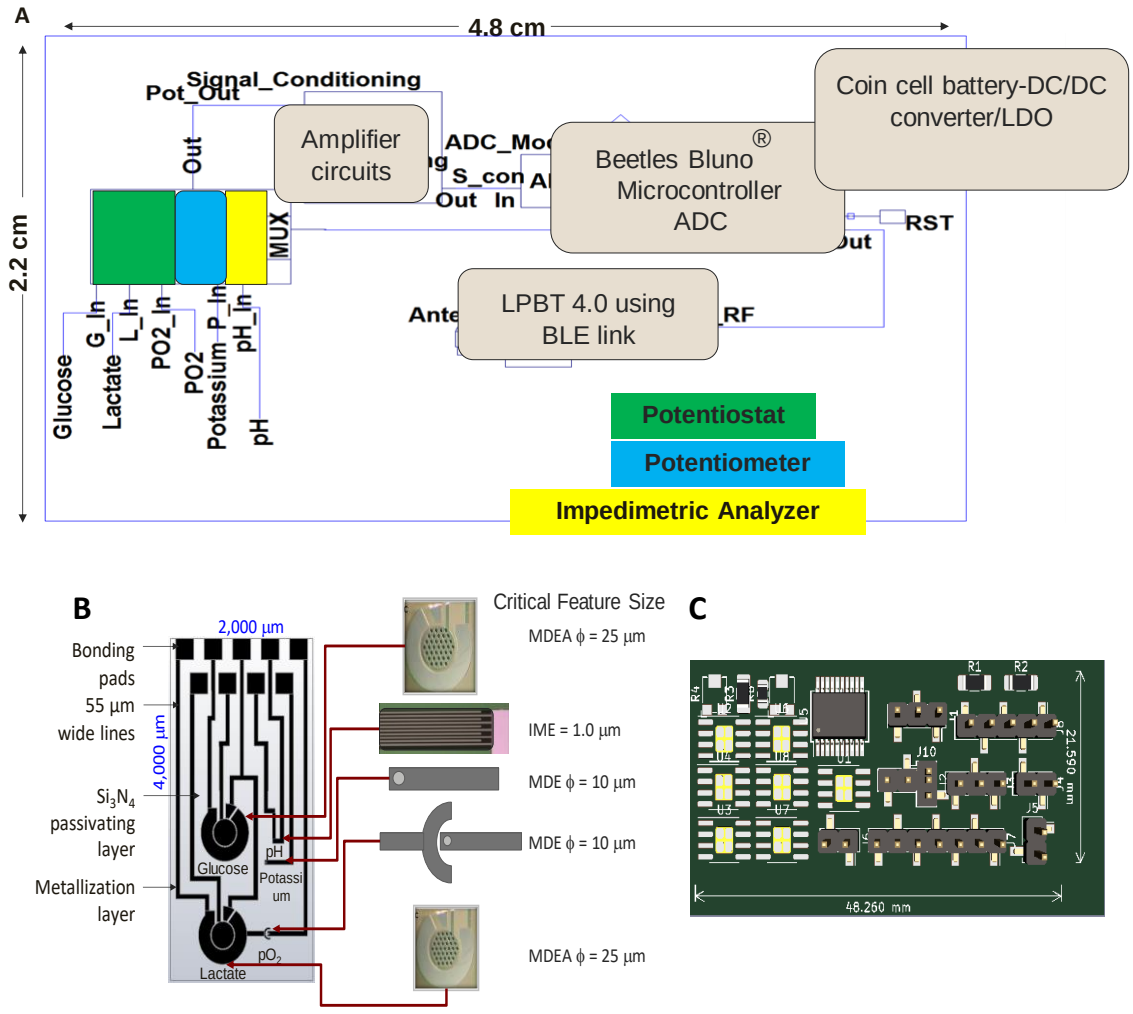

Figure 45. A) Design of hardware sensor in Eagle CadSoft, B) Design of the penta-analyte biochip comprising of glucose, lactate, pH, potassium and pO_2 in Solidworks, and C) PCB Schematic of hardware sensor.

As shown in **Figure 45A** glucose, lactate and pO_2 sensors will be interfaced with the potentiostat. Potassium will be interfaced with potentiometer, and pH will be interfaced with impedimetric analyzer. This forms the front-end. The signal is amplified using operational amplifiers (LMP7721, Texas Instruments, Dallas, TX) and conditioned using the Analog to Digital Converter using microcontroller ATMega328 from Beetles BLE (Bluno beetle V1.0, DFRobot, Shanghai, China). The data transmission is accomplished using the Bluetooth Low Energy Link. The final prototype shown in **Figure 45C** will be able to manage power usage for

all system components, collect and condition all analog signals from the five biotransducers of the sonde shown in **Figure 45B**, digitize those analog signals, store raw or conditioned data and operational parameters, wirelessly support unidirectional or bidirectional communication with a base station, rapidly wake up from a low-power "sleep" for immediate data collection. The microsystem will be externalized on animals and the sonde will be indwelling in the muscle of the animal which must be fully ambulatory. The pairing of these new types and architectures of biosensors, nanomaterials, and wireless communication and handheld devices, such as cell phones, remains a promising endeavor in telemedicine, remote healthcare, and biosensing. This study can be extended to integrate biotransducers, mixed signal electronics, low power devices and wireless communications into clinically relevant systems utilizing Hemorrhage Intensive Severity and Survivability (HISS) score for monitoring during trauma and surgery and for monitoring in the intensive care unit (ICU).

REFERENCES

1. Williams, M., A. Lockey, and M. Culshaw, *Improved trauma management with advanced trauma life support (ATLS) training.* Emergency Medicine Journal, 1997. **14**(2): p. 81-83.
2. Geeraedts, L.M.G., et al., *Exsanguination in trauma: A review of diagnostics and treatment options.* Injury, 2009. **40**(1): p. 11-20.
3. Blow, O., et al., *The golden hour and the silver day: detection and correction of occult hypoperfusion within 24 hours improves outcome from major trauma.* Journal of Trauma and Acute Care Surgery, 1999. **47**(5): p. 964.
4. Kauvar, D.S., R. Lefering, and C.E. Wade, *Impact of Hemorrhage on Trauma Outcome: An Overview of Epidemiology, Clinical Presentations, and Therapeutic Considerations.* Journal of Trauma and Acute Care Surgery, 2006. **60**(6): p. S3-S11.
5. Lerner, E.B. and R.M. Moscati, *The Golden Hour: Scientific Fact or Medical "Urban Legend"?* Academic Emergency Medicine, 2001. **8**(7): p. 758-760.
6. *National Trauma Institute, Trauma Statistics & Facts,.2018; Accessed: 12/18, Retrieved from: https://www.nattrauma.org/what-is-trauma/trauma-statistics-facts/.* [cited 2018 12/18]; Available from: https://www.nattrauma.org/what-is-trauma/trauma-statistics-facts/.
7. Pope A, F.G., Longnecker DE, , *Institute of Medicine (US) Committee on Fluid Resuscitation for Combat Casualties,*, in *Fluid Resuscitation: State of the Science for Treating Combat Casualties and Civilian Injuries,Washington (DC): National Academies Press (US);* . 1999,.
8. Lawton, L.D., et al., *The utility of Advanced Trauma Life Support (ATLS) clinical shock grading in assessment of trauma.* Emerg Med J, 2013: p. emermed-2012-201813.
9. Folmer, G.G., et al., *Resuscitation with Pooled and Pathogen-Reduced Plasma Attenuates the Increase in Brain Water Content following Traumatic Brain Injury and Hemorrhagic Shock in Rats.* Journal of Neurotrauma, 2017. **34**(5): p. 1054-1062.
10. Rezende-Neto, J., et al., *Rabbit model of uncontrolled hemorrhagic shock and hypotensive resuscitation.* Brazilian Journal of Medical and Biological Research, 2010. **43**(12): p. 1153-1159.
11. Hansen, J., et al., *Metabolic modulation of sympathetic vasoconstriction in human skeletal muscle: role of tissue hypoxia.* The Journal of Physiology, 2000. **527**(2): p. 387-396.
12. Chaudry, I.H., M.M. Sayeed, and A.E. Baue, *Effect of Hemorrhagic Shock on Tissue Adenine Nucleotides in Conscious Rats.* Canadian Journal of Physiology and Pharmacology, 1974. **52**(2): p. 131-137.
13. Kotanen, C.N. and A. Guiseppi-Elie, *Monitoring systems and quantitative measurement of biomolecules for the management of trauma.* Biomedical microdevices, 2013. **15**(3): p. 561-577.
14. Okuda, C., et al., *Lactate in rat skeletal muscle after hemorrhage measured by microdialysis probe calibrated in situ.* American Journal of Physiology-Endocrinology and Metabolism, 2006. **263**(6): p. E1035-E1039.

15. Paladino, L., et al., *The utility of base deficit and arterial lactate in differentiating major from minor injury in trauma patients with normal vital signs.* Resuscitation, 2008. **77**.
16. Lo, J., et al., *Increased prevalence of subclinical coronary atherosclerosis detected by coronary computed tomography angiography in HIV-infected men.* AIDS (London, England), 2010. **24**(2): p. 243-253.
17. Haut, E.R., et al., *Prehospital intravenous fluid administration is associated with higher mortality in trauma patients: a National Trauma Data Bank analysis.* Annals of surgery, 2011. **253**(2): p. 371-377.
18. Hietbrink, F., et al., *Trauma: the role of the innate immune system.* World Journal of Emergency Surgery, 2006. **1**(1): p. 15.
19. Plank, L.D. and G.L. Hill, *Sequential Metabolic Changes following Induction of Systemic Inflammatory Response in Patients with Severe Sepsis or Major Blunt Trauma.* World Journal of Surgery, 2000. **24**(6): p. 630-638.
20. Bone, R.C., *Immunologic Dissonance: A Continuing Evolution in Our Understanding of the Systemic Inflammatory Response Syndrome (SIRS) and the Multiple Organ Dysfunction Syndrome (MODS).* Annals of Internal Medicine, 1996. **125**(8): p. 680-687.
21. Vaddiraju, S., et al., *Emerging synergy between nanotechnology and implantable biosensors: a review.* Biosensors and Bioelectronics, 2010. **25**(7): p. 1553-1565.
22. Chen, X., et al., *Electrochemically Mediated Electrodeposition/Electropolymerization To Yield a Glucose Microbiosensor with Improved Characteristics.* Analytical Chemistry, 2002. **74**(2): p. 368-372.
23. Córcoles, E.P. and M.G. Boutelle, *Implantable Biosensors*, in *Biosensors and Invasive Monitoring in Clinical Applications*. 2013, Springer International Publishing: Heidelberg. p. 21-41.
24. Karpova, E.V., et al., *Noninvasive Diabetes Monitoring through Continuous Analysis of Sweat Using Flow-Through Glucose Biosensor.* Analytical Chemistry, 2019. **91**(6): p. 3778-3783.
25. Sharma, S., et al., *Minimally invasive microneedle array electrodes employing direct electron transfer type glucose dehydrogenase for the development of continuous glucose monitoring sensors.* Procedia technology, 2017. **27**: p. 208-209.
26. Sohrab, B., *Minimally invasive methods of monitoring analyte concentration*. 2004, Google Patents.
27. Mukerjee, E.V. and R.L. Smith, *Method and/or apparatus for puncturing a surface for extraction, in situ analysis, and/or substance delivery using microneedles*. 2010, Google Patents.
28. Gonnelli, R., *Microneedle with membrane*. 2005, Google Patents.
29. Davis, S.P., et al., *Insertion of microneedles into skin: measurement and prediction of insertion force and needle fracture force.* Journal of Biomechanics, 2004. **37**(8): p. 1155-1163.
30. El-Laboudi, A., et al., *Use of microneedle array devices for continuous glucose monitoring: a review.* Diabetes technology & therapeutics, 2013. **15**(1): p. 101-115.
31. Yu, B., et al., *An Investigation of Long-Term Performance of Minimally Invasive Glucose Biosensors.* Diabetes Technology & Therapeutics, 2007. **9**(3): p. 265-275.
32. Yetisen, A.K., et al., *Reusable, Robust, and Accurate Laser-Generated Photonic Nanosensor.* Nano Letters, 2014. **14**(6): p. 3587-3593.

33. Kiang, T., S. Ranamukhaarachchi, and M. Ensom, *Revolutionizing therapeutic drug monitoring with the use of interstitial fluid and microneedles technology.* Pharmaceutics, 2017. **9**(4): p. 43.
34. Rafael, K.R.S.M.C.S., Morgan & Claypool Life Sciences. **Chapter 5, Microvascular Fluid and Solute Exchange in Skeletal Muscle.**
35. Duret, J., et al., *Skeletal muscle oxygenation in severe trauma patients during haemorrhagic shock resuscitation.* Critical Care, 2015. **19**(1): p. 141.
36. Wittenberg, B.A. and J.B. Wittenberg, *Transport of oxygen in muscle.* Annual Review of Physiology, 1989. **51**(1): p. 857-878.
37. Kiang, T.K., S.A. Ranamukhaarachchi, and M.H. Ensom, *Revolutionizing therapeutic drug monitoring with the use of interstitial fluid and microneedles technology.* Pharmaceutics, 2017. **9**(4): p. 43.
38. *Sensor Biocompatibility and Biofouling in Real-Time Monitoring*, in *Wiley Encyclopedia of Biomedical Engineering*.
39. Turner, A.P.F., *Biosensors: sense and sensibility.* Chemical Society Reviews, 2013. **42**(8): p. 3184-3196.
40. Gifford, R., et al., *Protein interactions with subcutaneously implanted biosensors.* Biomaterials, 2006. **27**(12): p. 2587-2598.
41. Ekblad, T., *Hydrogel coatings for biomedical and biofouling applications*, in *Linköping Studies in Science and Technology. Dissertations*. 2010, Linköping University Electronic Press: Linköping. p. 74.
42. Hirshberg, E., G. Larsen, and H. Van Duker, *Alterations in glucose homeostasis in the pediatric intensive care unit: Hyperglycemia and glucose variability are associated with increased mortality and morbidity.* Pediatric Critical Care Medicine, 2008. **9**(4): p. 361-366.
43. Andersen, L.W., et al. *Etiology and therapeutic approach to elevated lactate levels*. in *Mayo Clinic Proceedings*. 2013. Elsevier.
44. Viera, A.J. and N. Wouk, *Potassium Disorders: Hypokalemia and Hyperkalemia.* American family physician, 2015. **92**(6).
45. de Jonge, E., et al., *Association between administered oxygen, arterial partial oxygen pressure and mortality in mechanically ventilated intensive care unit patients.* Critical care, 2008. **12**(6): p. R156.
46. Myers, J.A., K.W. Millikan, and T.J. Saclarides, *Common surgical diseases: An algorithmic approach to problem solving*. 2008: Springer Science & Business Media.
47. Thévenot, D.R., et al., *Electrochemical biosensors: recommended definitions and classification1International Union of Pure and Applied Chemistry: Physical Chemistry Division, Commission I.7 (Biophysical Chemistry); Analytical Chemistry Division, Commission V.5 (Electroanalytical Chemistry).1.* Biosensors and Bioelectronics, 2001. **16**(1): p. 121-131.
48. Putzbach, W. and N.J. Ronkainen, *Immobilization Techniques in the Fabrication of Nanomaterial-Based Electrochemical Biosensors: A Review.* Sensors, 2013. **13**(4): p. 4811-4840.
49. Bélanger, D., J. Nadreau, and G. Fortier, *Electrochemistry of the polypyrrole glucose oxidase electrode.* Journal of electroanalytical chemistry and interfacial electrochemistry, 1989. **274**(1-2): p. 143-155.

50. Sung, W.J. and Y.H. Bae, *Glucose oxidase, lactate oxidase, and galactose oxidase enzyme electrode based on polypyrrole with polyanion/PEG/enzyme conjugate dopant.* Sensors and Actuators B: Chemical, 2006. **114**(1): p. 164-169.
51. Guiseppi-Elie, A., *An implantable biochip to influence patient outcomes following trauma-induced hemorrhage.* Analytical and bioanalytical chemistry, 2011. **399**(1): p. 403-419.
52. Kotanen, C.N., et al., *Implantable enzyme amperometric biosensors.* Biosensors and Bioelectronics, 2012. **35**(1): p. 14-26.
53. Kiechle, F.L. and R.I. Main, *Blood Glucose: Measurement in the Point-of-Care Setting.* Laboratory Medicine, 2000. **31**(5): p. 276-282.
54. Mohan, A.M.V., et al., *Continuous minimally-invasive alcohol monitoring using microneedle sensor arrays.* Biosensors and Bioelectronics, 2017. **91**: p. 574-579.
55. Sharma, S., et al., *Evaluation of a minimally invasive glucose biosensor for continuous tissue monitoring.* Analytical and bioanalytical chemistry, 2016. **408**(29): p. 8427-8435.
56. Patil, S.A., C. Hägerhäll, and L. Gorton, *Electron transfer mechanisms between microorganisms and electrodes in bioelectrochemical systems.* Bioanalytical Reviews, 2012. **4**(2): p. 159-192.
57. Keel, M. and O. Trentz, *Pathophysiology of polytrauma.* Injury, 2005. **36**(6): p. 691-709.
58. Trzeciak, S., et al., *Serum lactate as a predictor of mortality in patients with infection.* Intensive Care Medicine, 2007. **33**(6): p. 970-977.
59. Backer, D.D., et al., *Microvascular Blood Flow Is Altered in Patients with Sepsis.* American Journal of Respiratory and Critical Care Medicine, 2002. **166**(1): p. 98-104.
60. Mikkelsen, M.E., et al., *Serum lactate is associated with mortality in severe sepsis independent of organ failure and shock*.* Critical Care Medicine, 2009. **37**(5): p. 1670-1677.
61. Lier, H., et al., *Preconditions of Hemostasis in Trauma: A Review. The Influence of Acidosis, Hypocalcemia, Anemia, and Hypothermia on Functional Hemostasis in Trauma.* Journal of Trauma and Acute Care Surgery, 2008. **65**(4): p. 951-960.
62. Ouellet, J.-F., et al., *Admission base deficit and lactate levels in Canadian patients with blunt trauma: Are they useful markers of mortality?* Journal of Trauma and Acute Care Surgery, 2012. **72**(6): p. 1532-1535.
63. Rossaint, R., et al., *Management of bleeding following major trauma: an updated European guideline.* Critical care, 2010. **14**(2): p. R52.
64. Vincent, J.-l., et al., *Serial lactate determinations during circulatory shock.* Critical care medicine, 1983. **11**(6): p. 449-451.
65. Higgins, C., *L-lactate and d-lacate–clinical significance in the difference.* Acute Care Testing. October, 2011.
66. Lin, C.-C. and A.T. Metters, *Hydrogels in controlled release formulations: network design and mathematical modeling.* Advanced drug delivery reviews, 2006. **58**(12-13): p. 1379-1408.
67. De las Heras Alarcón, C., S. Pennadam, and C. Alexander, *Stimuli responsive polymers for biomedical applications.* Chemical Society Reviews, 2005. **34**(3): p. 276-285.
68. Alarcón, C.d.l.H., S. Pennadam, and C. Alexander, *Stimuli responsive polymers for biomedical applications.* Chemical Society Reviews, 2005. **34**(3): p. 276-285.

69. Sheppard Jr, N.F., et al., *Microfabricated conductimetric pH sensor.* Sensors and Actuators B: Chemical, 1995. **28**(2): p. 95-102.
70. Koetting, M.C., et al., *Stimulus-responsive hydrogels: Theory, modern advances, and applications.* Materials Science and Engineering: R: Reports, 2015. **93**: p. 1-49.
71. Sheppard, N.F., et al., *Electrical conductivity of pH-responsive hydrogels.* Journal of Biomaterials Science, Polymer Edition, 1997. **8**(5): p. 349-362.
72. Ziglar, M.K., *Application of base deficit in resuscitation of trauma patients.* International Journal of Trauma Nursing, 2000. **6**(3): p. 81-84.
73. Kaplan, L.J. and J.A. Kellum, *Initial pH, base deficit, lactate, anion gap, strong ion difference, and strong ion gap predict outcome from major vascular injury.* Critical care medicine, 2004. **32**(5): p. 1120-1124.
74. Gun'ko, V.M., I.N. Savina, and S.V. Mikhalovsky, *Properties of Water Bound in Hydrogels.* Gels, 2017. **3**(4): p. 37.
75. Bhat, A., et al., *Molecular engineering of poly(HEMA-co-PEGMA)-based hydrogels: Role of minor AEMA and DMAEMA inclusion.* Materials Science and Engineering: C, 2019. **98**: p. 89-100.
76. Summersgill, A., et al., *Determining the Utility of Metabolic Acidosis for Trauma Patients in the Emergency Department.* The Journal of Emergency Medicine, 2015. **48**(6): p. 693-698.
77. Leach, R.M. and D.F. Treacher, *Oxygen transport2. Tissue hypoxia.* BMJ, 1998. **317**(7169): p. 1370-1373.
78. Yang, L. and A. Guiseppi-Elie, *Impedimetric Biosensors for Nano-and Microfluidics.* Encyclopedia of microfluidics and nanofluidics, 2015: p. 1364-1380.
79. Aggas, J.R., et al., *Nano-Pt ennobling of stainless steel for biomedical applications.* Electrochimica Acta, 2019. **301**: p. 153-161.
80. Culver, H.R., J.R. Clegg, and N.A. Peppas, *Analyte-Responsive Hydrogels: Intelligent Materials for Biosensing and Drug Delivery.* Accounts of Chemical Research, 2017. **50**(2): p. 170-178.
81. Yin, M.-J., et al., *Rapid 3D Patterning of Poly(acrylic acid) Ionic Hydrogel for Miniature pH Sensors.* Advanced Materials, 2016. **28**(7): p. 1394-1399.
82. Tamayol, A., et al., *Flexible pH-Sensing Hydrogel Fibers for Epidermal Applications.* Advanced healthcare materials, 2016. **5**(6): p. 711-719.
83. Au, B.K., et al., *Hyperkalemia Following Massive Transfusion in Trauma1.* Journal of Surgical Research, 2009. **157**(2): p. 284-289.
84. Palmer, B.F., *Regulation of Potassium Homeostasis.* Clinical journal of the American Society of Nephrology : CJASN, 2015. **10**(6): p. 1050-1060.
85. Uyehara, C.F. and J. Sarkar, *Role of vasopressin in maintenance of potassium homeostasis in severe hemorrhage.* American Journal of Physiology-Regulatory, Integrative and Comparative Physiology, 2013. **305**(2): p. R101-R103.
86. Zhou, Y., et al., *Potentiometric monitoring DNA hybridization.* Biosensors and Bioelectronics, 2009. **24**(11): p. 3275-3280.
87. Nowak, L. and R. Macdonald, *Substance P: ionic basis for depolarizing responses of mouse spinal cord neurons in cell culture.* Journal of Neuroscience, 1982. **2**(8): p. 1119-1128.

88. Rocha Filho, J.A., et al., *Potassium in hemorrhagic shock: a potential marker of tissue hypoxia.* Journal of Trauma and Acute Care Surgery, 2010. **68**(6): p. 1335-1341.
89. Rocha Filho, J.A., et al., *Potassium in Hemorrhagic Shock: A Potential Marker of Tissue Hypoxia.* Journal of Trauma and Acute Care Surgery, 2010. **68**(6): p. 1335-1341.
90. Wilson, M., D.P. Davis, and R. Coimbra, *Diagnosis and monitoring of hemorrhagic shock during the initial resuscitation of multiple trauma patients: a review*. The Journal of Emergency Medicine, 2003. **24**(4): p. 413-422.
91. Collins, J.-A., et al., *Relating oxygen partial pressure, saturation and content: the haemoglobin–oxygen dissociation curve.* Breathe, 2015. **11**(3): p. 194-201.
92. Fuller, B.M. and R.P. Dellinger, *Lactate as a hemodynamic marker in the critically ill.* Current opinion in critical care, 2012. **18**(3): p. 267-272.
93. Żelechowska, K., et al., *Oxygen biosensor based on carbon nanotubes directly grown on graphitic substrate.* Sensors and Actuators B: Chemical, 2017. **240**: p. 1308-1313.
94. Bolger, F.B., et al., *Characterisation of carbon paste electrodes for real-time amperometric monitoring of brain tissue oxygen.* Journal of neuroscience methods, 2011. **195**(2): p. 135-142.
95. Zhang, J., et al., *Platinum monolayer electrocatalysts for O2 reduction: Pt monolayer on Pd (111) and on carbon-supported Pd nanoparticles.* The Journal of Physical Chemistry B, 2004. **108**(30): p. 10955-10964.
96. Ngamchuea, K., et al., *Planar diffusion to macro disc electrodes—what electrode size is required for the Cottrell and Randles-Sevcik equations to apply quantitatively?* Journal of Solid State Electrochemistry, 2014. **18**(12): p. 3251-3257.
97. Shimizu, K., L. Sepunaru, and R.G. Compton, *Innovative catalyst design for the oxygen reduction reaction for fuel cells.* Chemical science, 2016. **7**(5): p. 3364-3369.
98. Ward, K.R., et al., *Near infrared spectroscopy for evaluation of the trauma patient: a technology review.* Resuscitation, 2006. **68**(1): p. 27-44.
99. Salinas, J., et al., *Advanced monitoring and decision support for battlefield critical care environment.* US Army Medical Department journal, 2011: p. 73-82.
100. Salinas, J., et al., *Computerized decision support system improves fluid resuscitation following severe burns: An original study**. Critical Care Medicine, 2011. **39**(9): p. 2031-2038.
101. Theusinger, O.M. and J.H. Levy, *Point of Care Devices for Assessing Bleeding and Coagulation in the Trauma Patient.* Anesthesiology Clinics, 2013. **31**(1): p. 55-65.
102. Liu, N.T., et al., *Utility of vital signs, heart rate variability and complexity, and machine learning for identifying the need for lifesaving interventions in trauma patients.* Shock, 2014. **42**(2): p. 108-114.
103. Jiang, C., et al., *Machine Learning Paradigms for Next-Generation Wireless Networks.* IEEE Wireless Communications, 2017. **24**(2): p. 98-105.
104. Guiseppi-Elie, A., *Implantable biochip for managing trauma--induced hemorrhage*. 2012, Google Patents.
105. Marshall, J.C., et al., *Multiple organ dysfunction score: a reliable descriptor of a complex clinical outcome.* Critical care medicine, 1995. **23**(10): p. 1638-1652.
106. Bhat, A., Nazmi, S., Podstawczyk, D., Walther, B. K., Aggas, J. R., Homaifar, A., Ward, K. R.,and Guiseppi-Elie, A., *Fusing Five Physiological Biomarkers: Toward A*

Hemorrhage Intensive Severity and Survivability (HISS) Score. Submitted to Journal of Biomedical and Health Informatics, 2020.
107. Chen, C., et al., *Recent advances in electrochemical glucose biosensors: a review.* RSC Advances, 2013. **3**(14): p. 4473-4491.
108. Mac Kenna, N., P. Calvert, and A. Morrin, *Impedimetric transduction of swelling in pH-responsive hydrogels.* Analyst, 2015. **140**(9): p. 3003-3011.
109. Vassilev, P. and M.T.M. Koper, *Electrochemical Reduction of Oxygen on Gold Surfaces: A Density Functional Theory Study of Intermediates and Reaction Paths.* The Journal of Physical Chemistry C, 2007. **111**(6): p. 2607-2613.
110. Farahi, R.H., et al. *Integrated electronics platforms for wireless implantable biosensors*. in *2007 IEEE/NIH Life Science Systems and Applications Workshop*. 2007.
111. Othman, S.B., et al. *Secure Data Transmission Protocol for Medical Wireless Sensor Networks*. in *2014 IEEE 28th International Conference on Advanced Information Networking and Applications*. 2014.
112. Nagarajan, R. and R. Dhanasekaran. *Implementation of wireless data transmission in monitoring and control*. in *2013 International Conference on Communication and Signal Processing*. 2013.
113. Ottenbrite, R.M., K. Park, and T. Okano, eds. *Biomedical Applications of Hydrogels Handbook.* 1st Edition ed. 2010, Springer: New York. 700 p.
114. Nicolson, P.C. and J. Vogt, *Soft contact lens polymers: an evolution.* Biomaterials, 2001. **22**(24): p. 3273-3283.
115. Hassan, C.M. and N.A. Peppas, *Structure and applications of poly(vinyl alcohol) hydrogels produced by conventional crosslinking or by freezing/thawing methods.* Biopolymers/Pva Hydrogels/Anionic Polymerisation Nanocomposites, 2000. **153**: p. 37-65.
116. Nguyen, K.T. and J.L. West, *Photopolymerizable hydrogels for tissue engineering applications.* Biomaterials, 2002. **23**(22): p. 4307-4314.
117. Zhu, J.M. and R.E. Marchant, *Design properties of hydrogel tissue-engineering scaffolds.* Expert Review of Medical Devices, 2011. **8**(5): p. 607-626.
118. Alakpa, Enateri V., et al., *Tunable Supramolecular Hydrogels for Selection of Lineage-Guiding Metabolites in Stem Cell Cultures.* Chem. **1**(2): p. 298-319.
119. Guenther, M. and G. Gerlach, *Hydrogels for Chemical Sensors.* Hydrogel Sensors and Actuators: Engineering and Technology, 2009. **6**: p. 165-195.
120. Brahim, S., D. Narinesingh, and A. Guiseppi-Elie, *Polypyrrole-hydrogel composites for the construction of clinically important biosensors.* Biosensors & Bioelectronics, 2002. **17**(1-2): p. 53-59.
121. Peppas, N.A., et al., *Hydrogels in pharmaceutical formulations.* European Journal of Pharmaceutics and Biopharmaceutics, 2000. **50**(1): p. 27-46.
122. Aucoin, H.R., et al., *Release of Potassium Ion and Calcium Ion from Phosphorylcholine Group Bearing Hydrogels.* Polymers, 2013. **5**(4): p. 1241-1257.
123. Guiseppi-Elie, A., et al., *Design of a subcutaneous implantable biochip for monitoring of glucose and lactate.* Ieee Sensors Journal, 2005. **5**(3): p. 345-355.
124. Abraham, S., et al., *Molecularly engineered p(HEMA)-based hydrogels for implant biochip biocompatibility.* Biomaterials, 2005. **26**(23): p. 4767-4778.

125. Brahim, S., D. Narinesingh, and A. Guiseppi-Elie, *Release characteristics of novel pH-sensitive p (HEMA-DMAEMA) hydrogels containing 3-(trimethoxy-silyl) propyl methacrylate.* Biomacromolecules, 2003. **4**(5): p. 1224-1231.
126. Guiseppi-Elie, A., S.I. Brahim, and D. Narinesingh, *A Chemically Synthesized Artificial Pancreas: Release of Insulin from Glucose-Responsive Hydrogels.* Advanced Materials, 2002. **14**(10): p. 743-746.
127. Schellekens, H., W.E. Hennink, and V. Brinks, *The Immunogenicity of Polyethylene Glycol: Facts and Fiction.* Pharmaceutical Research, 2013. **30**(7): p. 1729-1734.
128. Chang, C.-J., et al., *A genome-wide association study identifies a novel susceptibility locus for the immunogenicity of polyethylene glycol.* Nature Communications, 2017. **8**(1): p. 522.
129. Guiseppi-Elie, A., *Electroconductive hydrogels: Synthesis, characterization and biomedical applications.* Biomaterials, 2010. **31**(10): p. 2701-2716.
130. Pasqui, D., M. De Cagna, and R. Barbucci, *Polysaccharide-Based Hydrogels: The Key Role of Water in Affecting Mechanical Properties.* Polymers, 2012. **4**(3): p. 1517-1534.
131. van de Wetering, P., et al., *A mechanistic study of the hydrolytic stability of poly(2-(dimethylamino)ethyl methacrylate).* Macromolecules, 1998. **31**(23): p. 8063-8068.
132. Jhon, M.S. and J.D. Andrade, *Water and hydrogels.* Journal of Biomedical Materials Research, 1973. **7**(6): p. 509-522.
133. Lin, C.C. and A.T. Metters, *Hydrogels in controlled release formulations: network design and mathematical modeling.* Adv Drug Deliv Rev, 2006. **58**(12-13): p. 1379-408.
134. Guiseppi-Elie, A., C.B. Dong, and C.Z. Dinu, *Crosslink density of a biomimetic poly(HEMA)-based hydrogel influences growth and proliferation of attachment dependent RMS 13 cells.* Journal of Materials Chemistry, 2012. **22**(37): p. 19529-19539.
135. Pekař, M., *Hydrogels with Micellar Hydrophobic (Nano)Domains.* Frontiers in Materials, 2015. **1**(35).
136. Ishihara, K., M. Mu, and T. Konno, *Water-soluble and amphiphilic phospholipid copolymers having 2-methacryloyloxyethyl phosphorylcholine units for the solubilization of bioactive compounds.* J Biomater Sci Polym Ed, 2017: p. 1-39.
137. El-Sherbiny, I.M. and M.H. Yacoub, *Hydrogel scaffolds for tissue engineering: Progress and challenges.* Global Cardiology Science and Practice, 2013: p. 38.
138. Sharpe, L.A., et al., *Therapeutic applications of hydrogels in oral drug delivery.* Expert opinion on drug delivery, 2014. **11**(6): p. 901-915.
139. Heydari, A., A. Pardakhti, and H. Sheibani, *Preparation and Characterization of Zwitterionic Poly (β-cyclodextrin-co-guanidinocitrate) Hydrogels for Ciprofloxacin Controlled Release.* Macromolecular Materials and Engineering, 2017. **302**(6).
140. Sprouse, D. and T.M. Reineke, *Investigating the Effects of Block versus Statistical Glycopolycations Containing Primary and Tertiary Amines for Plasmid DNA Delivery.* Biomacromolecules, 2014. **15**(7): p. 2616-2628.
141. van de Wetering, P., et al., *A Mechanistic Study of the Hydrolytic Stability of Poly(2-(dimethylamino)ethyl methacrylate).* Macromolecules, 1998. **31**(23): p. 8063-8068.
142. Karunwi, O., et al., *Engineering the Abio-Bio Interface to Enable More than Moore in Functional Bioelectronics.* Journal of The Electrochemical Society, 2013. **160**(4): p. B60-B65.

143. Kotanen, C.N., et al., *Partitioning of coomassie brilliant blue into DMAEMA containing poly(HEMA)-based hydrogels.* European Polymer Journal, 2015. **72**: p. 438-450.
144. Shklyar, T.F., et al., *A correlation between mechanical and electrical properties of the synthetic hydrogel chosen as an experimental model of cytoskeleton.* Biophysics, 2008. **53**(6): p. 544-549.
145. Yeum, B., *Technical Note 24-Pseudocapacitance Associated with CPE.* Zsimpwin Programme, EChem Softwate, 2002.
146. Kotanen, C.N., O. Karunwi, and A. Guiseppi-Elie, *Biofabrication using pyrrole electropolymerization for the immobilization of glucose oxidase and lactate oxidase on implanted microfabricated biotransducers.* Bioengineering, 2014. **1**(1): p. 85-110.
147. Scarritt, M.E., R. Londono, and S.F. Badylak, *Host Response to Implanted Materials and Devices: An Overview*, in *The Immune Response to Implanted Materials and Devices*. 2017, Springer. p. 1-14.
148. Biran, R. and D. Pond, *Heparin coatings for improving blood compatibility of medical devices.* Advanced drug delivery reviews, 2017. **112**: p. 12-23.
149. Rabe, M., D. Verdes, and S. Seeger, *Understanding protein adsorption phenomena at solid surfaces.* Advances in Colloid and Interface Science, 2011. **162**(1-2): p. 87-106.
150. Clark, H.R., T.A. Barbari, and G. Rao, *Modeling the response time of an in vivo glucose affinity sensor.* Biotechnology Progress, 1999. **15**(2): p. 259-266.
151. Thevenot, P., W.J. Hu, and L.P. Tang, *Surface chemistry influences implant biocompatibility.* Current Topics in Medicinal Chemistry, 2008. **8**(4): p. 270-280.
152. Bajpai, A.K. and S. Kankane, *Preparation and characterization of macroporous poly(2-hydroxyethyl methacrylate)-based biomaterials: Water sorption property and in vitro blood compatibility.* Journal of Applied Polymer Science, 2007. **104**(3): p. 1559-1571.
153. Jenney, C.R. and J.M. Anderson, *Adsorbed serum proteins responsible for surface dependent human macrophage behavior.* Journal of Biomedical Materials Research, 2000. **49**(4): p. 435-447.
154. Bergström, K., et al., *Reduction of fibrinogen adsorption on PEG-coated polystyrene surfaces.* Journal of Biomedical Materials Research Part A, 1992. **26**(6): p. 779-790.
155. Liu, Y., *Some consideration on the Langmuir isotherm equation.* Colloids and Surfaces A: Physicochemical and Engineering Aspects, 2006. **274**(1): p. 34-36.
156. Rabe, M., D. Verdes, and S. Seeger, *Understanding protein adsorption phenomena at solid surfaces.* Advances in Colloid and Interface Science, 2011. **162**(1): p. 87-106.
157. Sangster, J., *Octanol-water partition coefficients of simple organic compounds.* Journal of Physical and Chemical Reference Data, 1989. **18**(3): p. 1111-1229.
158. Kyte, J. and R.F. Doolittle, *A simple method for displaying the hydropathic character of a protein.* Journal of molecular biology, 1982. **157**(1): p. 105-132.
159. Brahim, S., D. Narinesingh, and A. Guiseppi-Elie, *Synthesis and Hydration Properties of pH-Sensitive p(HEMA)-Based Hydrogels Containing 3-(Trimethoxysilyl)propyl Methacrylate.* Biomacromolecules, 2003. **4**(3): p. 497-503.
160. Seidel, J.M. and S.M. Malmonge, *Synthesis of polyHEMA hydrogels for using as biomaterials. Bulk and solution radical-initiated polymerization techniques.* Materials Research, 2000. **3**(3): p. 79-83.
161. Chinga, G., et al., *Quantification of the 3D microstructure of SC surfaces.* Journal of microscopy, 2007. **227**(3): p. 254-265.

162. Rafiee, M.A., et al., *Fracture and fatigue in graphene nanocomposites.* small, 2010. **6**(2): p. 179-183.
163. Arakawa, K. and K. Takahashi, *Relationships between fracture parameters and fracture surface roughness of brittle polymers.* International Journal of Fracture, 1991. **48**(2): p. 103-114.
164. Kyritsis, A., et al., *Water and polymer dynamics in poly(hydroxyl ethyl acrylate-co-ethyl acrylate) copolymer hydrogels.* European Polymer Journal, 2011. **47**(12): p. 2391-2402.
165. Zhang, R., et al., *Role of salt and water in the plasticization of PDAC/PSS polyelectrolyte assemblies.* The Journal of Physical Chemistry B, 2016. **121**(1): p. 322-333.
166. Pasqui, D., M. De Cagna, and R. Barbucci, *Polysaccharide-Based Hydrogels: The Key Role of Water in Affecting Mechanical Properties.* Polymers, 2012. **4**(3): p. 1517.
167. Miller, D.A., *The ionic conductivity of p (2-hydroxyethyl methacrylate) hydrogels*, in *Dept. of Physical and Inorganic Chemistry*. 1995, The University of Adelaide. p. 210.
168. Blythe, A.R. and D. Bloor, *Electrical properties of polymers*. 2005: Cambridge University Press.
169. Strathmann, H., *Electrochemical and thermodynamic fundamentals.* Ion-Exchange membrane separation processes, Elsevir, 2004: p. 23-88.
170. Wertz, C.F. and M.M. Santore, *Adsorption and Relaxation Kinetics of Albumin and Fibrinogen on Hydrophobic Surfaces: Single-Species and Competitive Behavior.* Langmuir, 1999. **15**(26): p. 8884-8894.
171. Ouberai, M.M., K. Xu, and M.E. Welland, *Effect of the interplay between protein and surface on the properties of adsorbed protein layers.* Biomaterials, 2014. **35**(24): p. 6157-6163.
172. Meyers, S.R. and M.W. Grinstaff, *Biocompatible and bioactive surface modifications for prolonged in vivo efficacy.* Chemical reviews, 2011. **112**(3): p. 1615-1632.
173. Zhang, X., et al., *The Pathway to Intelligence: Using Stimuli-Responsive Materials as Building Blocks for Constructing Smart and Functional Systems.* Advanced Materials, 2019. **31**(11): p. 1804540.
174. Bruggeman, K.F., R.J. Williams, and D.R. Nisbet, *Dynamic and Responsive Growth Factor Delivery from Electrospun and Hydrogel Tissue Engineering Materials.* Advanced Healthcare Materials, 2018. **7**(1): p. 1700836.
175. Zhang, X. and S. Soh, *Signal Amplification: A Sharp Impermeable-Permeable Transition for Highly Sensitive Low-Cost Detection.* Advanced Materials Technologies, 2018. **3**(6): p. 1800042.
176. Molinaro, G., et al., *Biocompatibility of thermosensitive chitosan-based hydrogels: an in vivo experimental approach to injectable biomaterials.* Biomaterials, 2002. **23**(13): p. 2717-2722.
177. Qiu, Y. and K. Park, *Environment-sensitive hydrogels for drug delivery.* Advanced drug delivery reviews, 2001. **53**(3): p. 321-339.
178. Pedrosa, V.A., et al., *Micropatterned nanocomposite hydrogels for biosensing applications.* Electroanalysis, 2011. **23**(5): p. 1142-1149.
179. Gulrez, S.K., S. Al-Assaf, and G.O. Phillips, *Hydrogels: methods of preparation, characterisation and applications*, in *Progress in molecular and environmental bioengineering-from analysis and modeling to technology applications*. 2011, InTech. p. 117.

180. Abasi, S., et al., *Biotechnical Properties of Poly(HEMA-co-HPMA) Hydrogels Are Governed by Distribution among Water States.* ACS Biomaterials Science & Engineering, 2019. **5**(10): p. 4994-5004.
181. Abasi, S., et al., *Distribution of water states within Poly(HEMA-co-HPMA)-based hydrogels.* Polymer, 2019: p. 121978.
182. Buenger, D., F. Topuz, and J. Groll, *Hydrogels in sensing applications.* Progress in Polymer Science, 2012. **37**(12): p. 1678-1719.
183. Wilson, A.N. and A. Guiseppi-Elie, *Bioresponsive Hydrogels.* Advanced Healthcare Materials, 2013. **2**(4): p. 520-532.
184. De, S.K., et al., *Equilibrium swelling and kinetics of pH-responsive hydrogels: Models, experiments, and simulations.* Journal of Microelectromechanical Systems, 2002. **11**(5): p. 544-555.
185. Siegel, R.A., *Stimuli sensitive polymers and self regulated drug delivery systems: A very partial review.* Journal of Controlled Release, 2014. **190**: p. 337-351.
186. Schmaljohann, D., *Thermo- and pH-responsive polymers in drug delivery.* Advanced Drug Delivery Reviews, 2006. **58**(15): p. 1655-1670.
187. Koetting, M.C., et al., *Stimulus-responsive hydrogels: Theory, modern advances, and applications.* Materials science & engineering. R, Reports : a review journal, 2015. **93**: p. 1-49.
188. Horava, S.D. and N.A. Peppas, *Design of pH-Responsive Biomaterials to Enable the Oral Route of Hematological Factor IX.* Annals of Biomedical Engineering, 2016. **44**(6): p. 1970-1982.
189. Nakamae, K., T. Miyata, and A.S. Hoffman, *Swelling behavior of hydrogels containing phosphate groups.* Die Makromolekulare Chemie, 1992. **193**(4): p. 983-990.
190. Rizwan, M., et al., *pH Sensitive Hydrogels in Drug Delivery: Brief History, Properties, Swelling, and Release Mechanism, Material Selection and Applications.* Polymers, 2017. **9**(4): p. 137.
191. Brannon-Peppas, L. and N.A. Peppas, *Dynamic and equilibrium swelling behaviour of pH-sensitive hydrogels containing 2-hydroxyethyl methacrylate.* Biomaterials, 1990. **11**(9): p. 635-644.
192. Sheppard Jr., N.F., et al., *Microfabricated conductimetric pH sensor.* Sensors and Actuators B: Chemical, 1995. **28**(2): p. 95-102.
193. Deirram, N., et al., *pH-Responsive Polymer Nanoparticles for Drug Delivery.* Macromolecular Rapid Communications, 2019. **40**(10): p. 1800917.
194. Rapado, M. and C. Peniche, *Synthesis and characterization of pH and temperature responsive poly(2-hydroxyethyl methacrylate-co-acrylamide) hydrogels.* Polímeros, 2015. **25**: p. 547-555.
195. Siegel, R.A., et al., *pH-Controlled release from hydrophobic/polyelectrolyte copolymer hydrogels.* Journal of Controlled Release, 1988. **8**(2): p. 179-182.
196. Chen, G. and A.S. Hoffman, *Graft copolymers that exhibit temperature-induced phase transitions over a wide range of pH.* Nature, 1995. **373**(6509): p. 49-52.
197. Brahim, S., D. Narinesingh, and A. Guiseppi-Elie, *Synthesis and hydration properties of pH-sensitive p (HEMA)-based hydrogels containing 3-(trimethoxysilyl) propyl methacrylate.* Biomacromolecules, 2003. **4**(3): p. 497-503.

198. Walker, A., et al., *Enhanced elasticity in poly(acrylic acid) gels via synthesis in the presence of high concentrations of select salts.* Soft Matter, 2019.
199. Shklyar, T., et al., *A correlation between mechanical and electrical properties of the synthetic hydrogel chosen as an experimental model of cytoskeleton.* Biophysics, 2008. **53**(6): p. 544-549.
200. Lvovich, V.F., *Fundamentals of Electrochemical Impedance Spectroscopy*, in *Impedance Spectroscopy*. 2012, John Wiley & Sons, Inc.: Hoboken, New Jersey p. 16.
201. Rana, S., R.H. Page, and C.J. McNeil, *Impedance spectra analysis to characterize interdigitated electrodes as electrochemical sensors.* Electrochimica Acta, 2011. **56**(24): p. 8559-8563.
202. Soller, B.R., et al., *Lightweight noninvasive trauma monitor for early indication of central hypovolemia and tissue acidosis: a review.* Journal of Trauma and Acute Care Surgery, 2012. **73**(2): p. S106-S111.
203. Bhat, A., J.M. Amanor-Boadu, and A. Guiseppi-Elie, *Toward Impedimetric Measurement of Acidosis with a pH-Responsive Hydrogel Sensor.* ACS Sensors, 2020. **5**(2): p. 500-509.
204. Abraham, S., et al., *Molecularly engineered p (HEMA)-based hydrogels for implant biochip biocompatibility.* Biomaterials, 2005. **26**(23): p. 4767-4778.
205. Yang, L., A. Guiseppi-Wilson, and A. Guiseppi-Elie, *Design considerations in the use of interdigitated microsensor electrode arrays (IMEs) for impedimetric characterization of biomimetic hydrogels.* Biomedical Microdevices, 2011. **13**(2): p. 279-289.
206. Van de Wetering, P., et al., *A mechanistic study of the hydrolytic stability of poly (2-(dimethylamino) ethyl methacrylate).* Macromolecules, 1998. **31**(23): p. 8063-8068.
207. Taguchi, G. and M.S. Phadke, *Quality engineering through design optimization*, in *Quality Control, Robust Design, and the Taguchi Method*. 1989, Springer. p. 77-96.
208. Dehnad, K., *Taguchi's Quality Philosophy: Analysis and Commentary*, in *Quality Control, Robust Design, and the Taguchi Method*. 2012, Springer Science & Business Media: Boston, MA. p. 16.
209. Anderson, M.J. and P.J. Whitcomb, *Introduction to the Beauty of Response Surface Methods*, in *RSM simplified: optimizing processes using response surface methods for design of experiments*. 2016, Productivity press: Boca Raton, FL. p. 22.
210. Tie, D., et al., *XPS Studies of Magnesium Surfaces after Exposure to Dulbecco's Modified Eagle Medium, Hank's Buffered Salt Solution, and Simulated Body Fluid.* Advanced Engineering Materials, 2010. **12**(12): p. B699-B704.
211. Kotanen, C.N., et al., *Partitioning of coomassie brilliant blue into DMAEMA containing poly (HEMA)-based hydrogels.* European Polymer Journal, 2015. **72**: p. 438-450.
212. Bhat, A., et al., *Dataset on hydrophobicity indices and differential scanning calorimetry thermograms for poly(HEMA)-based hydrogels.* Data in Brief, 2019. **24**: p. 103891.
213. Ping, Z., et al., *States of water in different hydrophilic polymers—DSC and FTIR studies.* Polymer, 2001. **42**(20): p. 8461-8467.
214. Amanor-Boadu, J., A. Guiseppi-Elie, and E. Sánchez-Sinencio, *The Impact of Pulse Charging Parameters on the Life Cycle of Lithium-Ion Polymer Batteries.* Energies, 2018. **11**(8): p. 2162.

215. Ginting, E. and M.M. Tambunan, *Selection of Optimal Factor Level From Process Parameters in Palm Oil Industry*. IOP Conference Series: Materials Science and Engineering, 2018. **288**: p. 012056.
216. Kotanen, C.N., et al., *The effect of the physicochemical properties of bioactive electroconductive hydrogels on the growth and proliferation of attachment dependent cells.* Biomaterials, 2013. **34**(27): p. 6318-6327.
217. Justin, G. and A. Guiseppi-Elie, *Characterization of electroconductive blends of poly (HEMA-co-PEGMA-co-HMMA-co-SPMA) and poly (Py-co-PyBA).* Biomacromolecules, 2009. **10**(9): p. 2539-2549.
218. Shipman Jr, C., *Evaluation of 4-(2-hydroxyethyl)-1-piperazineëthanesulfonic acid (HEPES) as a tissue culture buffer.* Proceedings of the Society for experimental biology and medicine, 1969. **130**(1): p. 305-310.
219. Strathmann, H., *Electrochemical and thermodynamic fundamentals*, in *Ion-Exchange membrane separation processes*. 2004, Elsevier. p. 23-88.
220. Rungsardthong, U., et al., *Effect of polymer ionization on the interaction with DNA in nonviral gene delivery systems.* Biomacromolecules, 2003. **4**(3): p. 683-690.
221. Thevenot, D.R., et al., *Electrochemical biosensors: recommended definitions and classification.* Pure and applied chemistry, 1999. **71**(12): p. 2333-2348.
222. Amanor-Boadu, J.M., A. Guiseppi-Elie, and E. Sánchez-Sinencio, *Search for Optimal Pulse Charging Parameters for Li-Ion Polymer Batteries Using Taguchi Orthogonal Arrays.* IEEE Transactions on Industrial Electronics, 2018. **65**(11): p. 8982-8992.
223. Stanley, H., C. Ogbonna, and G. Abu, *Exploration of One-Factor Rsm to Optimize the Concentration of Organic Fraction of Municipal Solid Waste (OFMSW) for Biogas Production.* Int J Waste Resour, 2017. **7**(293): p. 2.
224. Kumar, S. and P. Dinesha, *Optimization of engine parameters in a bio diesel engine run with honge methyl ester using response surface methodology.* Measurement, 2018. **125**: p. 224-231.
225. Zaretsky, M.C., L. Mouayad, and J.R. Melcher, *Continuum properties from interdigital electrode dielectrometry.* IEEE Transactions on Electrical Insulation, 1988. **23**(6): p. 897-917.
226. Carr, J.J., *Sensors and circuits: sensors, transducers, and supporting circuits for electronic instrumentation, measurement and control*. 1993: Prentice-Hall, Inc.
227. Halit Eren, W., John G, *Instrumentation and Measurement Concepts*, in *The measurement, instrumentation and sensors handbook: Electromagnetic, Optical, Radiation, Chemical, and Biomedical Measurement*. 2014, CRC press. p. 1-4.
228. Sheppard, N.F., R.C. Tucker, and C. Wu, *Electrical conductivity measurements using microfabricated interdigitated electrodes.* Analytical Chemistry, 1993. **65**(9): p. 1199-1202.
229. Sheppard, N.F., D.J. Mears, and A. Guiseppi-Elie, *Model of an immobilized enzyme conductimetric urea biosensor.* Biosensors and Bioelectronics, 1996. **11**(10): p. 967-979.
230. Abasi, S., et al., *Biotechnical Properties of Poly(HEMA-co-HPMA) Hydrogels are Governed by Distribution among Water States.* ACS Biomaterials Science & Engineering, 2019.
231. Hatton, K.W., et al., *Vagal nerve stimulation: overview and implications for anesthesiologists.* Anesthesia & Analgesia, 2006. **103**(5): p. 1241-1249.

232. Khodaparast, N., et al., *Vagus Nerve Stimulation During Rehabilitative Training Improves Forelimb Recovery After Chronic Ischemic Stroke in Rats.* Neurorehabilitation and Neural Repair, 2016. **30**(7): p. 676-684.
233. Meyers Eric, C., et al., *Vagus Nerve Stimulation Enhances Stable Plasticity and Generalization of Stroke Recovery.* Stroke, 2018. **49**(3): p. 710-717.
234. Sawan, M. and M. Elhilali, *Electronic stimulator implant for modulating and synchronizing bladder and sphincter function, United States Patent 6,393,323B1* McGill University; Gestion Univalor s.e.c., both of Montreal (CA)
235. Hou, S. and A.G. Rabchevsky, *Autonomic consequences of spinal cord injury.* Comprehensive Physiology, 2011. **4**(4): p. 1419-1453.
236. Douglas, W., G. Robert, and B. Timothy, *Monitoring and regulating physioloical states and functions via sensory neural inputs to the spinal cord, Patent No. US 9,622,671 B2* P. University of Pittsburgh of the commonwealth system of higher education, PA (US) Editor.
237. Moreno-Duarte, I., et al., *Targeted therapies using electrical and magnetic neural stimulation for the treatment of chronic pain in spinal cord injury.* Neuroimage, 2014. **85**: p. 1003-1013.
238. Meijs, S., et al., *Influence of fibrous encapsulation on electro-chemical properties of TiN electrodes.* Medical Engineering & Physics, 2016. **38**(5): p. 468-476.
239. Kastellorizios, M., N. Tipnis, and D.J. Burgess, *Foreign body reaction to subcutaneous implants*, in *Immune Responses to Biosurfaces*. 2015, Springer. p. 93-108.
240. Anderson, J.M., A. Rodriguez, and D.T. Chang, *Foreign body reaction to biomaterials.* Seminars in immunology, 2008. **20**(2): p. 86-100.
241. Green, R.A., et al., *Conducting polymers for neural interfaces: challenges in developing an effective long-term implant.* Biomaterials, 2008. **29**(24-25): p. 3393-3399.
242. McPherson, J.G., R.R. Miller, and S.I. Perlmutter, *Targeted, activity-dependent spinal stimulation produces long-lasting motor recovery in chronic cervical spinal cord injury.* Proceedings of the National Academy of Sciences, 2015. **112**(39): p. 12193-12198.
243. Onuki, Y., et al., *A review of the biocompatibility of implantable devices: current challenges to overcome foreign body response*. 2008, SAGE Publications.
244. Whitehurst, T.K., et al., *The Bion® Microstimulator and its Clinical Applications*, in *Implantable Neural Prostheses 1: Devices and Applications*, E. Greenbaum and D. Zhou, Editors. 2009, Springer US: New York, NY. p. 253-273.
245. Johnson, M.R., et al., *Minimally invasive implantation of epidural spinal cord neurostimulator electrodes by using a tubular retractor system.* Journal of neurosurgery, 2004. **100**(6): p. 1119-1121.
246. Moffitt, M. and D.K. Peterson, *System and method for maintaining a distribution of currents in an electrode array using independent voltage sources*.
247. Silva, L.V.D.C.d., et al., *TRANSCRANIAL DIRECT-CURRENT STIMULATION IN COMBINATION WITH EXERCISE: A SYSTEMATIC REVIEW.* Revista Brasileira de Medicina do Esporte, 2019. **25**: p. 520-526.
248. Fregni, F., et al., *A sham-controlled, phase II trial of transcranial direct current stimulation for the treatment of central pain in traumatic spinal cord injury.* PAIN, 2006. **122**(1): p. 197-209.

249. Dasilva, A.F., et al., *tDCS-induced analgesia and electrical fields in pain-related neural networks in chronic migraine.* Headache, 2012. **52**(8): p. 1283-1295.
250. Fregni, F., S. Freedman, and A. Pascual-Leone, *Recent advances in the treatment of chronic pain with non-invasive brain stimulation techniques.* The Lancet Neurology, 2007. **6**(2): p. 188-191.
251. Washburn, S., et al., *Patient-Perceived Differences Between Constant Current and Constant Voltage Spinal Cord Stimulation Systems.* Neuromodulation: Technology at the Neural Interface, 2014. **17**(1): p. 28-36.
252. Schade, C.M., et al., *Assessment of Patient Preference for Constant Voltage and Constant Current Spinal Cord Stimulation.* Neuromodulation: Technology at the Neural Interface, 2010. **13**(3): p. 210-217.
253. Geddes, L.A. and R. Roeder, *Criteria for the Selection of Materials for Implanted Electrodes.* Annals of Biomedical Engineering, 2003. **31**(7): p. 879-890.
254. Avery, R. and J. Wepsic, *Electrode implant for the neuro-stimulation of the spinal cord*, USPTO, Editor.
255. Edwards, C.A., et al., *Neurostimulation Devices for the Treatment of Neurologic Disorders.* Mayo Clinic Proceedings, 2017. **92**(9): p. 1427-1444.
256. Lu, Y., et al., *Flexible Neural Electrode Array Based-on Porous Graphene for Cortical Microstimulation and Sensing.* Scientific Reports, 2016. **6**(1): p. 33526.
257. Liu, T.-C., et al., *Implantable Graphene-based Neural Electrode Interfaces for Electrophysiology and Neurochemistry in In Vivo Hyperacute Stroke Model.* ACS Applied Materials & Interfaces, 2016. **8**(1): p. 187-196.
258. Myllymaa, S., K. Myllymaa, and R. Lappalainen, *Flexible implantable thin film neural electrodes*, in *Recent Advances in Biomedical Engineering*. 2009, IntechOpen. p. 165.
259. Rahim, S., X.-F. Huang, and J. Crook. *The Effects of Electrical Stimulation Mediated by Conductive Polymer on Hypothalamic Neurons as a Potential Model of Schizophrenia*. in *Proceedings of the International Conference of Theoretical and Applied Nanoscience and Nanotechnology (TANN'17)*. 2017. Toronto, Canada.
260. Stewart, E., et al., *Electrical stimulation using conductive polymer polypyrrole promotes differentiation of human neural stem cells: a biocompatible platform for translational neural tissue engineering.* Tissue Eng Part C Methods, 2015. **21**(4): p. 385-93.
261. Ludwig, K.A., et al., *Poly(3,4-ethylenedioxythiophene) (PEDOT) polymer coatings facilitate smaller neural recording electrodes.* Journal of Neural Engineering, 2011. **8**(1): p. 014001.
262. Abidian, M.R., et al., *Interfacing Conducting Polymer Nanotubes with the Central Nervous System: Chronic Neural Recording using Poly(3,4-ethylenedioxythiophene) Nanotubes.* Advanced Materials, 2009. **21**(37): p. 3764-3770.
263. Ludwig, K.A., et al., *Chronic neural recordings using silicon microelectrode arrays electrochemically deposited with a poly(3,4-ethylenedioxythiophene) (PEDOT) film.* Journal of Neural Engineering, 2006. **3**(1): p. 59-70.
264. Kolarcik, C.L., et al., *Evaluation of poly(3,4-ethylenedioxythiophene)/carbon nanotube neural electrode coatings for stimulation in the dorsal root ganglion.* Journal of Neural Engineering, 2014. **12**(1): p. 016008.
265. Green, R.A., et al., *Conducting polymers for neural interfaces: Challenges in developing an effective long-term implant.* Biomaterials, 2008. **29**(24): p. 3393-3399.

266. *Electrical Stimulation of Nerve Cells Using Conductive Nanofibrous Scaffolds for Nerve Tissue Engineering.* Tissue Engineering Part A, 2009. **15**(11): p. 3605-3619.
267. Ghasemi-Mobarakeh, L., et al., *Electrical stimulation of nerve cells using conductive nanofibrous scaffolds for nerve tissue engineering.* Tissue Eng Part A, 2009. **15**(11): p. 3605-19.
268. Balint, R., N.J. Cassidy, and S.H. Cartmell, *Conductive polymers: Towards a smart biomaterial for tissue engineering.* Acta Biomaterialia, 2014. **10**(6): p. 2341-2353.
269. Kaloni, T.P., et al., *Polythiophene: From Fundamental Perspectives to Applications.* Chemistry of Materials, 2017. **29**(24): p. 10248-10283.
270. Boeva, Z. and V. Sergeyev, *Polyaniline: Synthesis, Properties, and Application.* Polymer Science Series C, 2014. **56**.
271. Vernitskaya, T.y.V. and O.N. Efimov, *Polypyrrole: a conducting polymer; its synthesis, properties and applications.* Russian Chemical Reviews, 1997. **66**(5): p. 443-457.
272. Shrestha, S., et al., *Electrodeless coating polypyrrole on chitosan grafted polyurethane with functionalized multiwall carbon nanotubes electrospun scaffold for nerve tissue engineering.* Carbon, 2018. **136**: p. 430-443.
273. Yang, Q., et al., *Polypyrrole-coated phase-change liquid perfluorocarbon nanoparticles for the visualized photothermal-chemotherapy of breast cancer.* Acta biomaterialia, 2019. **90**: p. 337-349.
274. Rocchitta, G., et al., *Enzyme Biosensors for Biomedical Applications: Strategies for Safeguarding Analytical Performances in Biological Fluids.* Sensors, 2016. **16**(6): p. 780.
275. Kotanen, C., O. Karunwi, and A. Guiseppi-Elie, *Biofabrication using pyrrole electropolymerization for the immobilization of glucose oxidase and lactate oxidase on implanted microfabricated biotransducers.* Bioengineering, 2014. **1**(1): p. 85-110.
276. Ramanavičius, A., A. Ramanavičienė, and A. Malinauskas, *Electrochemical sensors based on conducting polymer—polypyrrole.* Electrochimica acta, 2006. **51**(27): p. 6025-6037.
277. Richardson, R.T., et al., *The effect of polypyrrole with incorporated neurotrophin-3 on the promotion of neurite outgrowth from auditory neurons.* Biomaterials, 2007. **28**(3): p. 513-523.
278. Bhat, A., Graham A. R., Trivedi H., Hogan M. K., Horner P. J., and Guiseppi-Elie A., *Engineering the ABIO-BIO Interface of Neurostimulation Electrodes Using Polypyrrole and Bioactive Hydrogels.* Submitted to Pure and Applied Chemistry, 2020.
279. Kotanen, C.N., C. Tlili, and A. Guiseppi-Elie, *Bioactive Electroconductive Hydrogels: The Effects of Electropolymerization Charge Density on the Storage Stability of an Enzyme-Based Biosensor.* Applied Biochemistry and Biotechnology, 2012. **166**(4): p. 878-888.
280. Pajkossy, T. and R. Jurczakowski, *Electrochemical impedance spectroscopy in interfacial studies.* Current Opinion in Electrochemistry, 2017. **1**(1): p. 53-58.
281. Karunwi, O. and A. Guiseppi-Elie, *Supramolecular glucose oxidase-SWNT conjugates formed by ultrasonication: effect of tube length, functionalization and processing time.* Journal of Nanobiotechnology, 2013. **11**(1): p. 6.
282. Ferreira, T. and W. Rasband, *The ImageJ User Guide-Version 1.44, Part V: 27.7*. 2011.
283. Elgrishi, N., et al., *A Practical Beginner's Guide to Cyclic Voltammetry.* Journal of Chemical Education, 2018. **95**(2): p. 197-206.

284. Bard, A.J. and L.R. Faulkner, *Electrochemical methods : fundamentals and applications*. 2001, New York: Wiley.
285. Stewart, E., et al., *Electrical stimulation using conductive polymer polypyrrole promotes differentiation of human neural stem cells: a biocompatible platform for translational neural tissue engineering.* Tissue Engineering Part C: Methods, 2014. **21**(4): p. 385-393.
286. Tan, Y. and K. Ghandi, *Kinetics and mechanism of pyrrole chemical polymerization.* Synthetic Metals, 2013. **175**: p. 183-191.
287. Bredas, J.L., et al., *Chain-length dependence of electronic and electrochemical properties of conjugated systems: polyacetylene, polyphenylene, polythiophene, and polypyrrole.* Journal of the American Chemical Society, 1983. **105**(22): p. 6555-6559.
288. Hauke, J. and T. Kossowski, *Comparison of values of Pearson's and Spearman's correlation coefficients on the same sets of data.* Quaestiones geographicae, 2011. **30**(2): p. 87-93.
289. Ferrara, N., H.-P. Gerber, and J. LeCouter, *The biology of VEGF and its receptors.* Nature Medicine, 2003. **9**(6): p. 669-676.
290. Dinarello, C.A., *Anti-inflammatory Agents: Present and Future.* Cell, 2010. **140**(6): p. 935-950.
291. Kohane, D.S. and R. Langer, *Polymeric Biomaterials in Tissue Engineering.* Pediatric Research, 2008. **63**: p. 487.
292. Okpala, C., A. Guiseppi-Elie, and D.M. Maharajh, *Several properties of 1,1,3,3-tetramethylurea-water systems.* Journal of Chemical & Engineering Data, 1980. **25**(4): p. 384-386.
293. Geeraedts, L.M., Jr., et al., *Exsanguination in trauma: A review of diagnostics and treatment options.* Injury, 2009. **40**(1): p. 11-20.
294. Tsuei, B.J. and P.A. Kearney, *Hypothermia in the trauma patient.* Injury, 2004. **35**(1): p. 7-15.
295. Wilcox, G., *Insulin and insulin resistance.* The Clinical biochemist. Reviews, 2005. **26**(2): p. 19-39.
296. Chima, R.S., et al., *Ciglitazone ameliorates lung inflammation by modulating the inhibitor kappaB protein kinase/nuclear factor-kappaB pathway after hemorrhagic shock.* Critical care medicine, 2008. **36**(10): p. 2849-2857.
297. Weil, M.H. and W. Tang, *Forty-Five-Year Evolution of Stat Blood and Plasma Lactate Measurement to Guide Critical Care.* Clinical Chemistry, 2009. **55**(11): p. 2053-2054.
298. Paladino, L., et al., *The utility of base deficit and arterial lactate in differentiating major from minor injury in trauma patients with normal vital signs.* Resuscitation, 2008. **77**(3): p. 363-8.
299. Luchette, F.A., et al., *Adrenergic antagonists reduce lactic acidosis in response to hemorrhagic shock.* Journal of Trauma and Acute Care Surgery, 1999. **46**(5): p. 873-880.
300. Aboudara, M.C., et al., *Hyperkalemia After Packed Red Blood Cell Transfusion in Trauma Patients.* Journal of Trauma and Acute Care Surgery, 2008. **64**(2): p. S86-S91.
301. Keel, M. and O. Trentz, *Pathophysiology of polytrauma.* Injury $V 36, 2005(6): p. 691-709.
302. Sasser, S.M., et al., *Guidelines for field triage of injured patients: recommendations of the National Expert Panel on Field Triage, 2011.* Morbidity and Mortality Weekly Report: Recommendations and Reports, 2012. **61**(1): p. 1-20.

303. Seamon, M.J., et al., *Just one drop: the significance of a single hypotensive blood pressure reading during trauma resuscitations.* J Trauma, 2010. **68**(6): p. 1289-94; discussion 1294-1295.
304. Cocchi, M.N., et al., *Identification and resuscitation of the trauma patient in shock.* Emerg Med Clin North Am, 2007. **25**(3): p. 623-42, vii.
305. Vandromme, M.J., et al., *Lactate is a better predictor than systolic blood pressure for determining blood requirement and mortality: could prehospital measures improve trauma triage?* J Am Coll Surg, 2010. **210**(5): p. 861-7, 867-9.
306. Lin, G., A. Becker, and M. Lynn, *Do pre-hospital trauma alert criteria predict the severity of injury and a need for an emergent surgical intervention?* Injury, 2012. **43**(9): p. 1381-1385.
307. Brasel, K.J., et al., *Heart Rate: Is It Truly a Vital Sign?* Journal of Trauma and Acute Care Surgery, 2007. **62**(4): p. 812-817.
308. Liu, N.T., et al., *Utility of vital signs, heart rate variability and complexity, and machine learning for identifying the need for lifesaving interventions in trauma patients.* Shock, 2014. **42**(2): p. 108-14.
309. Teasdale, G. and B. Jennett, *Assessment of coma and impaired consciousness: a practical scale.* The Lancet, 1974. **304**(7872): p. 81-84.
310. Teasdale, G. and B. Jennett, *Assessment and prognosis of coma after head injury.* Acta neurochirurgica, 1976. **34**(1-4): p. 45-55.
311. Benson, M., K.L. Koenig, and C.H. Schultz, *Disaster triage: START, then SAVE--a new method of dynamic triage for victims of a catastrophic earthquake.* Prehosp Disaster Med, 1996. **11**(2): p. 117-24.
312. Garner, A., et al., *Comparative analysis of multiple-casualty incident triage algorithms.* Ann Emerg Med, 2001. **38**(5): p. 541-8.
313. Jenkins, J.L., et al., *Mass-casualty triage: time for an evidence-based approach.* Prehosp Disaster Med, 2008. **23**(1): p. 3-8.
314. Sacco, W.J., et al., *Precise formulation and evidence-based application of resource-constrained triage.* Acad Emerg Med, 2005. **12**(8): p. 759-70.
315. Baker, S.P., et al., *The injury severity score: a method for describing patients with multiple injuries and evaluating emergency care.* J Trauma, 1974. **14**(3): p. 187-96.
316. Javali, R.H., et al., *Comparison of Injury Severity Score, New Injury Severity Score, Revised Trauma Score and Trauma and Injury Severity Score for Mortality Prediction in Elderly Trauma Patients.* Indian journal of critical care medicine : peer-reviewed, official publication of Indian Society of Critical Care Medicine, 2019. **23**(2): p. 73-77.
317. King, R.C., et al., *Application of data fusion techniques and technologies for wearable health monitoring.* Medical Engineering & Physics, 2017. **42**: p. 1-12.
318. Guiseppi-Elie, A., *Implantable biochip for managing trauma--induced hemorrhage, Patent No. US2012 0088997 A1, Apr. 12, 2012*
319. Bal, M., et al., *Performance Evaluation of the Machine Learning Algorithms Used in Inference Mechanism of a Medical Decision Support System.* The Scientific World Journal, 2014. **2014**: p. 15.
320. Paradiso, R., G. Loriga, and N. Taccini, *A wearable health care system based on knitted integrated sensors.* IEEE Transactions on Information Technology in Biomedicine, 2005. **9**(3): p. 337-344.

321. Lymberis, A., *Advanced Wearable Sensors and Systems Enabling Personal Applications*, in *Wearable and Autonomous Biomedical Devices and Systems for Smart Environment: Issues and Characterization*, A. Lay-Ekuakille and S.C. Mukhopadhyay, Editors. 2010, Springer Berlin Heidelberg: Berlin, Heidelberg. p. 237-257.
322. Majumder, S., T. Mondal, and M.J. Deen, *Wearable Sensors for Remote Health Monitoring.* Sensors, 2017. **17**(1): p. 130.
323. Salinas, J., et al., *Advanced monitoring and decision support for battlefield critical care environment.* US Army Medical Department journal, 2011.
324. Gerst, K.S., et al., *System and method for providing automatic setup of a remote patient care environment, Patent No. US 9773060 B2, Sep. 26, 2017*.
325. Chern, C.-C., Y.-J. Chen, and B. Hsiao, *Decision tree-based classifier in providing telehealth service.* BMC medical informatics and decision making, 2019. **19**(1): p. 104-104.
326. Sun, Y., et al., *Predicting prostate tumour location from multiparametric MRI using Gaussian kernel support vector machines: a preliminary study.* Australasian Physical & Engineering Sciences In Medicine, 2017. **40**(1): p. 39-49.
327. Topol, E.J., *High-performance medicine: the convergence of human and artificial intelligence.* Nature Medicine, 2019. **25**(1): p. 44-56.
328. Bond, R.R., et al., *Automation bias in medicine: The influence of automated diagnoses on interpreter accuracy and uncertainty when reading electrocardiograms.* Journal of Electrocardiology, 2018. **51**(6, Supplement): p. S6-S11.
329. Ramesh, A.N., et al., *Artificial intelligence in medicine.* Annals of the Royal College of Surgeons of England, 2004. **86**(5): p. 334-338.
330. Walker, P.B., et al., *A decision tree framework for understanding blast-induced mild Traumatic Brain Injury in a military medical database.* The Journal of Defense Modeling and Simulation, 2017. **14**(4): p. 389-398.
331. Safavian, S.R. and D. Landgrebe, *A survey of decision tree classifier methodology.* IEEE transactions on systems, man, and cybernetics, 1991. **21**(3): p. 660-674.
332. Zhu, D., *A hybrid approach for efficient ensembles.* Decision Support Systems, 2010. **48**(3): p. 480-487.
333. Krooshof, P.W., et al., *Visualization and recovery of the (bio) chemical interesting variables in data analysis with support vector machine classification.* Analytical chemistry, 2010. **82**(16): p. 7000-7007.
334. Moguerza, J.M. and A. Muñoz, *Support vector machines with applications.* Statistical Science, 2006. **21**(3): p. 322-336.
335. Steinwart, I. and A. Christmann, *Support vector machines*. 2008, Springer Science & Business Media. p. 287.
336. Trafalis, T.B. and R.C. Gilbert, *Robust support vector machines for classification and computational issues.* Optimization Methods and Software, 2007. **22**(1): p. 187-198.
337. Amato, F., et al., *Artificial neural networks in medical diagnosis.* Journal of Applied Biomedicine, 2013. **11**(2): p. 47-58.
338. Masumoto, H., et al., *Accuracy of a deep convolutional neural network in detection of retinitis pigmentosa on ultrawide-field images.* PeerJ, 2019. **7**: p. e6900-e6900.
339. Maulik, U. and S. Bandyopadhyay, *Genetic algorithm-based clustering technique.* Pattern Recognition, 2000. **33**(9): p. 1455-1465.

340. Kordmahalleh, M.M., et al., *Time-series forecasting with evolvable partially connected artificial neural network*, in *Proceedings of the Companion Publication of the 2014 Annual Conference on Genetic and Evolutionary Computation*. 2014, ACM: Vancouver, BC, Canada. p. 79-80.
341. Larvie, J.E., et al., *Stable Gene Regulatory Network Modeling From Steady-State Data.* Bioengineering, 2016. **3**(2): p. 12.
342. Davoudi, A., et al., *Intelligent ICU for Autonomous Patient Monitoring Using Pervasive Sensing and Deep Learning.* Scientific Reports, 2019. **9**(1): p. 8020.
343. Shickel, B., et al., *DeepSOFA: A Continuous Acuity Score for Critically Ill Patients using Clinically Interpretable Deep Learning.* Sci Rep, 2019. **9**(1): p. 1879.
344. Armen, S.B., et al., *Improving Outcomes in Patients With Sepsis.* American Journal of Medical Quality, 2016. **31**(1): p. 56-63.
345. Komorowski, M., et al., *The Artificial Intelligence Clinician learns optimal treatment strategies for sepsis in intensive care.* Nature Medicine, 2018. **24**(11): p. 1716-1720.
346. Zadeh, L.A., *Fuzzy sets as a basis for a theory of possibility.* Fuzzy sets and systems, 1978. **1**(1): p. 3-28.
347. Dubois, D. and H. Prade, *Possibility theory and its applications: Where do we stand?*, in *Springer Handbook of Computational Intelligence*. 2015, Springer. p. 31-60.
348. Nazmi, S., S. Ramyar, and A. Homaifar. *Determination of the Driver At-fault Using Possibility Theory-based Classification*. in *2019 Transportation Research Board Annual Meeting (TRB)*. 2019. TRB.
349. Denœux, T. and L.M. Zouhal, *Handling possibilistic labels in pattern classification using evidential reasoning.* Fuzzy sets and systems, 2001. **122**(3): p. 409-424.
350. Burnell, J.M., et al., *The effect in humans of extracellular pH change on the relationship between serum potassium concentration and intracellular potassium.* J Clin Invest, 1956. **35**(9): p. 935-9.
351. Valizadegan, H., Q. Nguyen, and M. Hauskrecht, *Learning classification models from multiple experts.* Journal of Biomedical Informatics, 2013. **46**(6): p. 1125-1135.
352. Castanedo, F., *A Review of Data Fusion Techniques.* The Scientific World Journal, 2013. **2013**: p. 19.
353. Newby, D., A.A. Freitas, and T. Ghafourian, *Comparing Multilabel Classification Methods for Provisional Biopharmaceutics Class Prediction.* Molecular Pharmaceutics, 2015. **12**(1): p. 87-102.
354. McLauchlan, L. and M. Mehrübeoğlu, *Neural network-based watermark embedding and identification*. Optical Engineering + Applications. Vol. 7075. 2008: SPIE.
355. Pomares, A., et al. *Ground Extraction from 3D Lidar Point Clouds with the Classification Learner App*. in *2018 26th Mediterranean Conference on Control and Automation (MED)*. 2018.
356. Rangelova, V., D. Tsankova, and N. Dimcheva, *Soft computing techniques in modelling the influence of ph and temperature on dopamine biosensor*, in *Intelligent and Biosensors*. 2010, InTech. p. 101.
357. Burden, F. and D. Winkler, *Bayesian Regularization of Neural Networks*, in *Artificial Neural Networks: Methods and Applications*, D.J. Livingstone, Editor. 2009, Humana Press: Totowa, NJ. p. 23-42.

358. Nazmi, S. and A. Homaifar, *Possibility Rule-based Classification using Function Approximation.* SMC, 2018.
359. Fawcett, T., *An introduction to ROC analysis.* Pattern Recognition Letters, 2006. **27**(8): p. 861-874.
360. Muh, H.C., J.C. Tong, and M.T. Tammi, *AllerHunter: A SVM-Pairwise System for Assessment of Allergenicity and Allergic Cross-Reactivity in Proteins.* PLOS ONE, 2009. **4**(6): p. e5861.
361. Nasrabadi, N.M., *Pattern recognition and machine learning.* Journal of electronic imaging, 2007. **16**(4): p. 049901.
362. Arlot, S. and A. Celisse, *A survey of cross-validation procedures for model selection.* Statistics surveys, 2010. **4**: p. 40-79.
363. Tibshirani, R. and G. Walther, *Cluster Validation by Prediction Strength.* Journal of Computational and Graphical Statistics, 2005. **14**(3): p. 511-528.
364. Pedregosa, F., et al., *Scikit-learn: Machine learning in Python.* Journal of machine learning research, 2011. **12**(Oct): p. 2825-2830.
365. Thornton, A.R. and M.J.M. Raffin, *Speech-Discrimination Scores Modeled as a Binomial Variable.* Journal of Speech and Hearing Research, 1978. **21**(3): p. 507-518.
366. Rehme, A.K., et al., *Identifying Neuroimaging Markers of Motor Disability in Acute Stroke by Machine Learning Techniques.* Cerebral Cortex, 2014. **25**(9): p. 3046-3056.
367. Bashir, S., U. Qamar, and F.H. Khan, *IntelliHealth: A medical decision support application using a novel weighted multi-layer classifier ensemble framework.* Journal of Biomedical Informatics, 2016. **59**: p. 185-200.
368. Forcellese, A., F. Gabrielli, and R. Ruffini, *Effect of the training set size on springback control by neural network in an air bending process.* Journal of Materials Processing Technology, 1998. **80-81**: p. 493-500.
369. Twomey, J.M. and A.E. Smith, *Bias and variance of validation methods for function approximation neural networks under conditions of sparse data.* IEEE Transactions on Systems, Man, and Cybernetics, Part C (Applications and Reviews), 1998. **28**(3): p. 417-430.
370. Asadi, H., et al., *Machine Learning for Outcome Prediction of Acute Ischemic Stroke Post Intra-Arterial Therapy.* PLOS ONE, 2014. **9**(2): p. e88225.
371. Shahid, N., T. Rappon, and W. Berta, *Applications of artificial neural networks in health care organizational decision-making: A scoping review.* PLOS ONE, 2019. **14**(2): p. e0212356.
372. Al-Absi, H.R.H., et al. *Hybrid Intelligent System for Disease Diagnosis Based on Artificial Neural Networks, Fuzzy Logic, and Genetic Algorithms*. in *Informatics Engineering and Information Science*. 2011. Berlin, Heidelberg: Springer Berlin Heidelberg.
373. Leibig, C., et al., *Leveraging uncertainty information from deep neural networks for disease detection.* Scientific Reports, 2017. **7**(1): p. 17816.
374. Moshtagh-Khorasani, M., et al., *An intelligent system based on fuzzy probabilities for medical diagnosis- a study in aphasia diagnosis.* Journal of research in medical sciences : the official journal of Isfahan University of Medical Sciences, 2009. **14**(2): p. 89-103.
375. R, N. and D.M.A. Kumar, *Enhanced Fuzzy K-NN Approach for Handling Missing Values in Medical Data Mining.* Indian Journal of Science and Technology, 2016. **9**: p. 1-7.

376. Cios, K.J. and G. William Moore, *Uniqueness of medical data mining.* Artificial Intelligence in Medicine, 2002. **26**(1): p. 1-24.
377. Eisele, S.C., P.Y. Wen, and E.Q. Lee, *Assessment of Brain Tumor Response: RANO and Its Offspring.* Curr Treat Options Oncol, 2016. **17**(7): p. 35.
378. Chan, V., et al., *A population based perspective on children and youth with brain tumours.* BMC cancer, 2015. **15**: p. 1007-1007.
379. Sexton, R.S. and J.N.D. Gupta, *Comparative evaluation of genetic algorithm and backpropagation for training neural networks.* Information Sciences, 2000. **129**(1): p. 45-59.
380. Iaccarino, G., et al. *Wind Turbine Optimization Under Uncertainty with High Performance Computing*. in *29th AIAA Applied Aerodynamics Conference. 2011*.
381. Petrone, G., et al., *A probabilistic non-dominated sorting GA for optimization under uncertainty.* ENGINEERING COMPUTATIONS, 2013. **30**: p. 1054-1085.
382. Justin, G., et al., *Biomimetic hydrogels for biosensor implant biocompatibility: electrochemical characterization using micro-disc electrode arrays (MDEAs).* Biomedical Microdevices, 2009. **11**(1): p. 103-115.
383. Kotanen, C.N. and A. Guiseppi-Elie, *Characterization of a Wireless Potentiostat for Integration With a Novel Implantable Biotransducer.* IEEE Sensors Journal, 2014. **14**(3): p. 768-776.